Antenna Development for MIMO and UHF RFID Applications

by

Chris D. Rouse

Bachelor of Science in Engineering, University of New Brunswick, 2009

A DISSERTATION SUBMITTED IN PARTIAL FULFILLMENT OF THE REQUIREMENTS FOR THE DEGREE OF

Doctor of Philosophy

In the Graduate Academic Unit of Electrical and Computer Engineering

Supervisors:	**Bruce G. Colpitts**, Ph.D., Electrical and Computer Engineering
	Brent R. Petersen, Ph.D., Electrical and Computer Engineering
Examining Board:	**Richard B. Langley**, Ph.D., Geodesy and Geomatics Engineering, Chair
	Eduardo Castillo Guerra, Ph.D., Electrical and Computer Engineering
	Kevin B. Englehart, Ph.D., Electrical and Computer Engineering
External Examiner:	**Zhizhang Chen**, Ph.D., Electrical and Computer Engineering, Dalhousie University

This dissertation is accepted

Dean of Graduate Studies

THE UNIVERSITY OF NEW BRUNSWICK

March, 2014

Abstract

Multiple-input multiple-output (MIMO) wireless communication systems are capable of achieving significantly higher channel capacities than single-antenna systems. Furthermore, there has been a trend toward installing a larger number of cellular base stations and wireless access points (APs) over the same physical coverage area in order to meet increasing capacity demands. An in-room MIMO system—in which an AP and a user with a portable device (PD) occupy the same room—is considered. The associated channel is dominated by line-of-sight (LOS) components, which tend to increase the received signal-to-noise ratio (SNR) but can degrade MIMO performance. Therefore, the application of elevation-directional (θ-directional) AP antennas which emphasize wall-reflected non-line-of-sight (NLOS) components is investigated to improve in-room MIMO capacity. Simulation results based on the experimental set-up suggest an improvement in mean MIMO capacity on the order of 13 % coupled with a 4 % increase in mean relative MIMO gain if the AP antenna radiation patterns strike a balance between improving MIMO channel conditions and maintaining an appropriate SNR. The associated measurements revealed only a 5 % improvement in mean MIMO capacity and a small reduction in mean relative MIMO gain due to the increased multipath richness associated with the real environment. However, the measured results validated the predicted relationship between the main lobe directions of the AP antenna radiation patterns and the resulting in-room MIMO performance, suggesting that more significant improvements could be achieved for in-room MIMO systems experiencing less multipath richness.

In the design of ultra-high frequency (UHF) radio-frequency identification (RFID) tags, the cost of the tag antenna is significant relative to that of the entire tag. As a result, cost-effective alternatives to copper as a UHF RFID tag antenna conductor have been explored in recent years. The feasibility of constructing such antennas using electrically conductive paper is investigated through simulations and experimental measurements. Results suggest that the conductivity of the paper is prohibitively low; however, reasonable performance would be achieved if the paper conductivity were increased by an order of magnitude.

Dedication

To my family.

Acknowledgements

I must first acknowledge and thank my supervisors, Dr. Bruce Colpitts and Dr. Brent Petersen, for their unwavering support and invaluable guidance throughout the pursuit of this degree. Dr. Colpitts particularly encouraged the development of my experimental and practical skills, while my theoretical and analytical skills benefited strongly from working with Dr. Petersen. I feel that I owe them both equally for my well-balanced academic growth.

I would also like to thank my fellow IsoTropic Thunder teammates, Brandon Brown and Fred Goora. Although our technical discussions were very helpful and enlightening, what I valued most was the friendship and general tomfoolery that we enjoyed. These tropics made pursuing the degree fun, even during the more difficult times, and always managed to keep me sane. Well, relatively sane anyway.

There are several other individuals who contributed to the completion of this degree. My fellow lab mates Mike Kurz, Satinder Gill and Mike Wylie helped in both an academic and technical capacity over the years. Bruce Miller, Ryan Jennings, Mike Morton, Claudio Riva and Greg Greer offered technical as well as practical help on several occasions. Without the administrative assistance of Shelley Cormier, Karen Annett and Denise Burke, I would have been lost.

Of course, none of this would have been possible without the love and support of my family and friends, whom I cannot even begin to thank. Actually, I guess I can *begin*, and here goes: "Thanks!"

Table of Contents

List of Tables

List of Figures

List of Abbreviations and Symbols

ADS	Advanced Design System
AOA	Angle-of-arrival
AP	Access Point
ASK	Amplitude Shift Keying
ATC	Anechoic Test Chamber
AWGN	Additive White Gaussian Noise
BER	Bit Error Rate
BLAST	Bell-labs Layered Space-Time
bps	Bits Per Second
cm	Centimetres
CW	Continuous Wave
CDF	Cumulative Distribution Function
CDMA	Code Division Multiple Access
CTM	Channel Transfer Matrix
CST	Computer Simulation Technology
dB	Decibels
dBi	Decibels Relative to an Isotropic Radiator
dBm	Decibels Relative to a Milliwatt
D-BLAST	Diagonal Bell-labs Layered Space-Time
DC	Direct Current

DFT	Discrete Fourier Transform
DOA	Direction-of-arrival
EIRP	Effective Isotropic Radiated Power
ESD	Electrostatic Discharge
FR-4	Flame Resistant-4
GHz	Gigahertz
HF	High Frequency
HPBW	Half-power Beamwidth
Hz	Hertz
IC	Integrated Circuit
IDFT	Inverse Discrete Fourier Transform
IFF	Identify Friend or Foe
ISM	Industrial, Scientific and Medical
kbps	Kilobits Per Second
kHz	Kilohertz
LF	Low Frequency
Low-e	Low-emissivity
LOS	Line-of-sight
LTE	Long Term Evolution
m	Metres
mm	Millimetres
mW	Milliwatts
MHz	Megahertz
MIMO	Multiple-input Multiple-output
MISO	Multiple-input Single-output
MSE	Mean Squared Error
μm	Micrometres

NLOS	Non-line-of-sight
ns	Nanoseconds
PCB	Printed Circuit Board
PD	Portable Device
PNA	Performance Network Analyzer
PSK	Phase Shift Keying
RCS	Radar Cross-section
RFID	Radio-frequency Identification
Rx	Receiver
SISO	Single-input Single-output
SIMO	Single-input Multiple-output
SBR	Shoot-and-bounce Ray Tracing
SMA	Subminiature Version A
SNR	Signal-to-noise Ratio
S	Siemens
TDMA	Time Domain Multiple Access
TEM	Transverse Electromagnetic
Tx	Transmitter
θ-directional	Elevation-directional
UCA	Uniform Circular Array
UHF	Ultra-high Frequency
UNB	University of New Brunswick
UWB	Ultra-wideband
V	Volts
V-BLAST	Vertical Bell-labs Layered Space-Time
VSWR	Voltage Standing Wave Ratio
W	Watts

Wi-Fi	Wireless Fidelity
WiMAX	Worldwide Interoperability for Microwave Access
WLAN	Wireless Local Area Network
a, b, i	General Purpose Variables
$a_{\mathrm{T}}, a_{\mathrm{T1}}, a_{\mathrm{T2}}$	Transmitted Symbols
$\mathbf{a}_{\mathrm{T}}$	Transmitted Symbol Vector
$\mathbf{a}'_{\mathrm{T}}$	Transformed Transmitted Symbol Vector
$a'_{\mathrm{T1}}, a'_{\mathrm{T2}}$	Transformed Transmitted Symbols
$\mathrm{A}, \mathrm{B}, \mathrm{C}, \mathrm{D}, \mathrm{P}, \mathrm{Q}, \mathrm{R}, \mathrm{S}$	van der Pauw Test Points
A	General Point in Space
A'	General Point Mirrored About a Boundary
A_1	Point Along the First Ray Segment
A_{AP}	Access Point Location in Space
A'_{AP}	Access Point Location Mirrored About a Boundary
A''_{AP}	Access Point Location Mirrored About Two Boundaries
$\hat{A}_{\mathrm{D}}, \hat{A}_{\mathrm{D1}}$	Unit Vectors Indicating Ray Directions
$\hat{A}_{\mathrm{inc}}$	Unit Vector Indicating the Direction of Wave Incidence
A_{PD}	Portable Device Location in Space
$A_{\mathrm{R}}, A_{\mathrm{R1}}, A_{\mathrm{R2}}$	Reflection Point Locations in Space
α	Value Indicating the Position of a Point Along a Ray
$\alpha_{\mathrm{R}}, \alpha_{\mathrm{R1}}$	Values Indicating the Positions of Reflection Points Along the Associated Rays
$b_{\mathrm{R}}, b_{\mathrm{R1}}, b_{\mathrm{R2}}$	Received Symbols
$\mathbf{b}_{\mathrm{R}}$	Received Symbol Vector
$\mathbf{b}'_{\mathrm{R}}$	Transformed Received Symbol Vector
$b'_{\mathrm{R1}}, b'_{\mathrm{R2}}$	Transformed Received Symbols

β	Progressive Phase Shift
c	Speed of Light
$\mathrm{c}_1, \mathrm{c}_2$	Constants
C	Capacity
C_{MIMO}	MIMO Capacity
$\overline{C_{\mathrm{MIMO}}}$	Room-averaged MIMO Capacity
C_{SISO}	SISO Capacity
$\chi, \chi_1, \chi_2, \psi$	Surface Definition Parameters
d_{AB}	Distance from a Point A to a Boundary
d_{AP}	Distance from the Access Point to the Floor
$d_{\mathrm{B}}, d_{\mathrm{B1}}$	Distances from Boundary Locations to the Origin
d_{d}	Dielectric Thickness
d_{e}	Distance Separating Non-adjacent Array Elements
$\vec{dl}$	Tangential Differential Length Vector
d_{PD}	Distance from the Portable Device to the Floor
$\vec{dS}$	Differential Surface Normal Vector
d_{t}	Conductor Thickness
d_{w}	Conductor Width
d_x	Room x-dimension
d_y	Room y-dimension
d_z	Room z-dimension
D_0	Maximum Antenna Directivity
$\delta(\cdot)$	Dirac Delta Function
$^\circ$	Degrees
δ_{s}	Skin Depth
Δ_{SE}	Improvement Over the Single-element Case
e_{rad}	Antenna Radiation Efficiency

$\vec{E}$	Electric Field Vector
$\vec{E}_{\text{inc}}$	Incident Electric Field Vector
$\vec{E}_{\text{rectangular}}$	Electric Field Vector in Rectangular Coordinates
$\vec{E}_{\text{ref}}$	Reflected Electric Field Vector
$\vec{E}_{\text{spherical}}$	Electric Field Vector in Spherical Coordinates
E_x, E_y, E_z	Electric Field Vector Components in Rectangular Coordinates
$\vec{E}_{\parallel}$	Electric Field Vector Component Parallel to the Plane of Incidence
$\vec{E}_{\perp}$	Electric Field Vector Component Perpendicular to the Plane of Incidence
ϵ_{e}	Effective Relative Permittivity / Effective Dielectric Constant
ϵ_{r}	Relative Permittivity / Dielectric Constant
ϵ_0	Permittivity of Free Space
η	Wave Impedance
f	Frequency
f_0	A Particular Frequency
f_{c}	Centre Frequency
f_{step}	Frequency Step
F_{A}	Array Factor
$g_{ba}(i)$	Complex Gain Associated with the i-th Multipath Component Linking the b-th Receive and a-th Transmit Antennas
g_C	Relative MIMO Gain
$\overline{g_C}$	Room-averaged Relative MIMO Gain
G_0, G_{01}, G_{02}	Maximum Antenna Gains

$G_{0,\text{reader}}$	Maximum Gain of an RFID Reader Antenna
$G_{0,\text{tag}}$	Maximum Gain of an RFID Tag Antenna
Γ_{normal}	Boundary Reflection Coefficient at Normal Incidence
$\lvert\Gamma_{\text{RL}}\rvert$	Magnitude of the Boundary Reflection Coefficient at Normal Incidence Based on a Measured Reflection Loss
Γ_{tag}	RFID Tag IC Input Reflection Coefficient
$\Gamma_{\parallel}$	Boundary Reflection Coefficient for Electric Field Vector Components Parallel to the Plane of Incidence
$\Gamma_{\perp}$	Boundary Reflection Coefficient for Electric Field Vector Components Perpendicular to the Plane of Incidence
h, h_1, h_2	SISO, MISO and SIMO Narrowband Discrete Complex Baseband Channel Impulse Responses
$h_{11}, h_{21}, h_{12}, h_{22}$	MIMO Narrowband Discrete Complex Baseband Channel Impulse Responses
$h_{ba}[n]$	Discrete Complex Baseband Channel Impulse Response Linking the b-th Receive and a-th Transmit Antennas
$h_{ba}(t)$	Complex Baseband Channel Impulse Response Linking the b-th Receive and a-th Transmit Antennas
$h_{ba,\text{sampled}}(t)$	Sampled Complex Baseband Channel Impulse Response Linking the b-th Receive and a-th Transmit Antennas
$H(f)$	Channel Transfer Function
$H(f_0)$	Channel Transfer Function Value at f_0
$H_{ba}[k]$	Discrete Channel Transfer Function Linking the b-th Receive and a-th Transmit Antennas
$\mathbf{H}$	Channel Transfer Matrix
$\mathbf{H}_k$	Channel Transfer Matrix at Frequency Index k
$i(z,t)$	Antenna Current

$I(z)$	Normalized Current Distribution Along z
$\mathbf{I}$	Identity Matrix
I_0	Peak Current
I_{AB}	Current Through the van der Pauw Test Points A and B
I_{in}	Antenna Input Current
I_{PQ}	Current Through the van der Pauw Test Points P and Q
I_S	Net Current Through the Surface S
j	Imaginary Number
J_a	a-th Order Bessel Function of the First Kind
$\vec{J}_{\mathrm{P}}$	Current Density Vector Due to a Source at the van der Pauw Test Point P
k	Frequency Sample Index
K	Number of Frequency Samples
κ	RFID Tag Power Transfer Coefficient
l	Antenna length
l_β	Transmission Line Length Incurring a Phase Shift of β
$\vec{l}_{\mathrm{e}}, \vec{l}_{\mathrm{e1}}, \vec{l}_{\mathrm{e2}}$	Antenna Vector Effective Lengths
l_ϕ	Azimuth-component of the Vector Effective Length
l_θ	Elevation-component of the Vector Effective Length
L	Number of Multipath Components
λ	Free Space Wavelength
λ_{m}	Wavelength on a Microstrip Line
$m_{ba}(t)$	Multipath Impulse Response Linking the b-th Receive and a-th Transmit Antennas
$m_{ba,\mathrm{baseband}}(t)$	Baseband Multipath Impulse Response Linking the b-th Receive and a-th Transmit Antennas
M	Number of Antennas at the Transmitter and Receiver

M_{R}	Number of Antennas at the Receiver
M_{T}	Number of Antennas at the Transmitter
μ	Permeability
n	Time Sample Index
$n_{\mathrm{W}}, n_{\mathrm{W1}}, n_{\mathrm{W2}}$	Received AWGN Signals
$\mathbf{n}_{\mathrm{W}}$	Received AWGN Vector
$\mathbf{n}'_{\mathrm{W}}$	Transformed Received AWGN Vector
$n'_{\mathrm{W1}}, n'_{\mathrm{W2}}$	Transformed Received AWGN Signals
$\hat{n}_{\mathrm{B}}, \hat{n}_{\mathrm{B1}}$	Boundary Unit Normal Vectors
$\hat{n}_{\mathrm{inc}}$	Unit Normal Vector of the Plane of Incidence
$\vec{n}_S$	Normal Vector of the Surface S
N	Number of Phased-array Elements
$\hat{o}_x, \hat{o}_y, \hat{o}_z$	Boundary Coordinate System Unit Vectors
Ω	Ohms
p	Parameter Satisfying the van der Pauw Formula
P_{EIRP}	Effective Isotropic Radiated Power
$P_{\mathrm{in}}, P_{\mathrm{in1}}, P_{\mathrm{in2}}$	Antenna Input Powers
P_{min}	Minimum Power for RFID Tag Activation
P_{N}	Noise Power
$P_{\mathrm{out}}, P_{\mathrm{out1}}, P_{\mathrm{out2}}$	Antenna Output Powers
P_{R}	Received Power
$P_{\mathrm{R}b}$	Received Power at the b-th Receive Antenna
P_{rad}	Antenna Radiated Power
P_{T}	Transmit Power
%	Percent
$\phi_{\mathrm{E}}, \theta_{\mathrm{E}}, \psi_{\mathrm{E}}$	Euler Angles
r, θ, ϕ	Spherical Coordinates

$\hat{r}, \hat{\theta}, \hat{\phi}$	Spherical Coordinate System Unit Vectors
r_{12}	Range Separating Two Antennas
r_{AP}	Radius of the Access Point Array
$r_{\max}$	Maximum RFID Read Range
$r_{\max,\mathrm{isotropic}}$	Maximum RFID Read Range When Using Isotropic Sources
r_{rel}	Relative RFID Read Range
r_{unamb}	Unambiguous Range
q	Two-dimensional Field Representation of the xy-plane
q'	Two-dimensional Field Representation of the $x'y'$-plane
$R_{\mathrm{AB,CD}}$	Ratio of the Voltage Across the van der Pauw Test Points D and C and the Current Through the van der Pauw Test Points A and B
R_{ba}	Mutual Resistances Between the b-th and a-th Array Elements
$R_{ba,\mathrm{isotropic}}$	Mutual Resistances Between the b-th and a-th Isotropic Elements
$R_{ba,\mathrm{dipole}}$	Mutual Resistances Between the b-th and a-th Dipole Elements
$R_{ba,\mathrm{loop}}$	Mutual Resistances Between the b-th and a-th Loop Elements
$R_{\mathrm{BC,DA}}$	Ratio of the Voltage Across the van der Pauw Test Points A and D and the Current Through the van der Pauw Test Points B and C
$\mathbf{R}_{\mathrm{E}}$	Euler Rotation Matrix
$\mathbf{R}_{\mathrm{E},\phi}, \mathbf{R}_{\mathrm{E},\theta}, \mathbf{R}_{\mathrm{E},\psi}$	Individual Euler Angle Rotation Matrices
R_{IC}	RFID Tag IC Input Resistance

R_{in}	Antenna Input Resistance
R_{lo}	Ohmic Resistance Per Unit Length
R_{loss}	Antenna Loss Resistance
R_{MA}	RFID Tag Matching Network and Antenna Input Resistance
$R_{\text{PQ,RS}}$	Ratio of the Voltage Across the van der Pauw Test Points S and R and the Current Through the van der Pauw Test Points P and Q
$R_{\text{QR,SP}}$	Ratio of the Voltage Across the van der Pauw Test Points P and S and the Current Through the van der Pauw Test Points Q and R
$R_{\text{rad}}, R_{\text{rad1}}, R_{\text{rad2}}$	Antenna Radiation Resistances
$R_{\text{rad},a}$	Radiation Resistance of the a-th Transmit Antenna
$R_{\text{rad},b}$	Radiation Resistance of the b-th Receive Antenna
ρ	SNR
ρ_{dB}	SNR in dB
$\overline{\rho_{\text{dB}}}$	Room-averaged SNR in dB
s_{AP}	Access Point Antenna Separation
s_{e}	Phased-array Element Separation
s_{PD}	Portable Device Antenna Separation
s_{PQ}	Separation Between the van der Pauw Test Points P and Q
s_{QR}	Separation Between the van der Pauw Test Points Q and R
s_{RS}	Separation Between the van der Pauw Test Points R and S
S	Surface

$S_{11}, S_{13}, S_{23}, S_{14}, S_{24}$	S-Parameters
$S_{13k}, S_{23k}, S_{14k}, S_{24k}$	S-Parameters at Frequency Index k
σ	Conductivity
t	Time
T_1, T_2	Arbitrary Points Defining a Surface
$\vec{T}_\chi, \vec{T}_\psi$	Surface Tangent Vectors
T_s	Sampling Period
$\tau_{ba}(i)$	Propagation Delay Associated with the i-th Multipath Component Linking the b-th Receive and a-th Transmit Antennas
θ_{inc}	Angle of Incidence Upon a Boundary
θ_{tra}	Angle of Transmission Into a Boundary
θ_0	Elevation-direction of the Radiation Pattern Maximum
$u(x, y)$	Potential Associated with $w(q)$
$u'(x', y')$	Potential Associated with $w'(q')$
$\mathbf{U}, \mathbf{V}$	Singular Vector Matrices
$v(x, y)$	Lines of Force Associated with $w(q)$
$v'(x', y')$	Lines of Force Associated with $w'(q')$
v_1, v_2	Values of $v(x, y)$
v'_1, v'_2	Values of $v'(x', y')$
$\hat{v}_n$	Unit Vector Indicating the Direction of the Line of Nodes
V_{DC}	Voltage Across the van der Pauw Test Points D and C
V_{in}, V_{in1}, V_{in2}	Antenna Input Voltages
$V_{in,a}(i)$	Input Voltage to the a-th Transmit Antenna Associated with the i-th Multipath Component
V_{oc}	Antenna Open-circuit Output Voltage
$V_{out}, V_{out1}, V_{out2}$	Antenna Output Voltages

$V_{\text{out},b}(i)$	Output Voltage from the b-th Receive Antenna Due to the i-th Multipath Component
$V_{\text{SR}}, V'_{\text{SR}}, V''_{\text{SR}}$	Voltages Across the van der Pauw Test Points S and R
$w_{\text{f}}(t)$	Filter Impulse Response
$w(q)$	Two-dimensional Field Defined in the q-plane
$w'(q')$	Two-dimensional Field Defined in the q'-plane
W	Single-sided Baseband Channel Bandwidth
x, y, z	Rectangular Coordinates
$\hat{x}, \hat{y}, \hat{z}$	Rectangular Coordinate System Unit Vectors
x', y'	Rectangular Coordinates of Transformed xy-plane Via Conformal Mapping
X_{IC}	RFID Tag IC Input Reactance
X_{in}	Antenna Input Reactance
X_{MA}	RFID Tag Matching Network and Antenna Input Reactance
ξ_1, ξ_2	Singular Values
ξ_{max}	Maximum Singular Value of $\mathbf{H}$
ξ_{min}	Minimum Singular Value of $\mathbf{H}$
$\boldsymbol{\Xi}$	Singular Value Matrix
Z_0	Characteristic Impedance
Z_1, Z_2	RFID Tag Antenna Load Impedances
Z_{IC}	RFID Tag IC Input Impedance
Z_{in}	Antenna Input Impedance
Z_{MA}	RFID Tag Matching Network and Antenna Input Impedance

Chapter 1

Introduction

This dissertation presents contributions to two distinct areas of wireless communications: multiple-input multiple-output (MIMO) systems and radio-frequency identification (RFID) systems operating in the ultra-high frequency (UHF) band. MIMO systems—in which multiple antennas are used at both the transmitter and receiver—can achieve significantly higher information capacities than single-input single-output (SISO) systems by exploiting differences among the channels linking each pair of transmit and receive antennas. As a result, MIMO finds application in many wireless communication standards such as Long Term Evolution (LTE), Worldwide Interoperability for Microwave Access (WiMAX) and Wireless Fidelity (Wi-Fi). In addition, cellular base stations and wireless local area network (WLAN) access points (APs) are being installed closer together in order to meet increasing capacity demands [1]. It is therefore conceivable that MIMO-equipped WLAN APs may only be responsible for providing service to individual rooms in the near future.

An in-room MIMO system consists of a room in which a MIMO-equipped WLAN AP and a user with a portable device (PD) are confined. The associated multipath interference is typically dominated by line-of-sight (LOS) components and, to a lesser extent, wall-reflected non-line-of-sight (NLOS) components [2–4]. Although the

existence of strong LOS components typically increases the received signal-to-noise ratio (SNR), it also reduces the achievable MIMO capacity improvements relative to the SISO case [5,6]. Conversely, NLOS channel conditions yield a lower received SNR while presenting a greater opportunity for capacity improvements with MIMO. The purpose of the MIMO-related research presented in this dissertation is to investigate the effect of exchanging the typically non-directional AP antennas with elevation-directional (θ-directional) AP antennas which emphasize wall-reflected NLOS components on in-room MIMO capacity. If the gains exhibited by the θ-directional AP antennas are sufficient to compensate for the relatively low power levels associated with these NLOS components, the system would benefit from NLOS channel conditions without incurring a reduction in the received SNR. This concept is explored through simulations based on an idealized in-room MIMO system model and experimentally via MIMO channel measurements conducted in an unoccupied classroom.

UHF RFID provides a means of automatic identification and finds application in a variety of industries such as retail, automotive, shipping and storage. A typical UHF RFID system includes a reader—which is usually equipped with a radio transceiver—and a tag consisting of an antenna and a simple integrated circuit (IC). In the interest of reducing both cost and complexity, UHF RFID tags are often passive, meaning that they do not feature an independent power supply such as a battery [7]. They are instead powered from radio-frequency (RF) energy incident from the reader. Communication from the tag to the reader is achieved via modulated backscatter.

As UHF RFID tag IC costs are reduced, the costs associated with the tag antennas become increasingly significant. Consequently, low-cost alternatives to copper as an antenna conductor have been investigated in recent years, such as silver ink [8] and advanced carbon-fibre composites [9]. The RFID-related research presented in this dissertation investigates the feasibility of replacing copper as an antenna conduc-

tor with electrically conductive paper, which has recently been developed as a low-cost and eco-friendly material for applications such as electrostatic discharge (ESD) packaging [10, 11]. A UHF RFID tag based on conductive paper could therefore be built into the packaging of a product and recycled along with it, increasing eco-friendliness in addition to reducing costs. A simulation model is developed in order to evaluate the performance of a conductive-paper dipole antenna and to characterize the relationship between the performance of the antenna and the conductivity of the paper. Measurements are performed using constructed copper and conductive-paper dipoles in order to validate the simulation results.

1.1 Contributions

Directional antennas, adaptive beamforming and a variety of antenna configurations have been applied to outdoor, outdoor-indoor, indoor and in-room environments in an effort to improve MIMO performance [12–17]. The primary contribution associated with the MIMO-related research presented here stems from the recognition that the directions-of-arrival (DOAs) associated with some of the dominant in-room multipath components—such as the aforementioned wall-reflected NLOS components—are quasi-predictable, regardless of the location of the PD within the room. As a result, exchanging the non-directional AP antennas for θ-directional antennas with radiation patterns which favour these general directions is a potentially simple way to improve MIMO capacity throughout the room. This concept has not been previously explored in the literature. Consequently, the results associated with its investigation through simulations and experimental measurements form a contribution to the field.

Although a variety of materials have been investigated as potential antenna conductors, conductive paper is relatively new and has never been applied in this

context. Consequently, the design, construction, simulation and measurement of conductive-paper antennas contribute new knowledge to the field. At this point, it is appropriate to acknowledge the work performed by Mr. Michael R. Kurz at the University of New Brunswick (UNB), who constructed one of the conductive-paper antennas, both of the copper antennas and provided valuable assistance during the experimental measurements. By characterizing the relationship between the conductivity of the paper and the performance of the associated antenna, a target conductivity is identified which directs further research efforts and forms an additional contribution. The research associated with the performance evaluation of conductive-paper dipole antennas has been published [18].

1.2 Organization of the Dissertation

This dissertation is organized into six chapters and two appendices. Chapter 1 introduces the subject areas under consideration: MIMO communications systems and UHF RFID systems. For each subject area, the motivations driving the corresponding research efforts are outlined. A discussion of the relevant contributions resulting from these efforts is presented.

Chapter 2 provides relevant background information for both MIMO and UHF RFID systems. In the subsequent chapters, it is often assumed that the reader is familiar with this background material in addition to the fundamentals of signal processing, microwave engineering and antenna theory. Due to the breadth of research which has been conducted in the area of MIMO communication systems, a review of the most significant and relevant literature is also provided.

Simulation details associated with improving in-room MIMO capacity using θ-directional AP antennas are presented in Chapter 3. The in-room MIMO system model is completely described; a code listing of the software written to implement the

model can be found in Appendix A. Simulation results corresponding to the use of non-directional AP antennas and a variety of θ-directional AP antenna configurations are presented for a particular room geometry. The influence of room geometry on performance is explored for a particular θ-directional AP antenna configuration.

Chapter 4 describes an experimental investigation of the results obtained in Chapter 3. Design, simulation, fabrication and measurement details associated with the antennas used during the measurements are presented. The selection and characterization of the room in which the measurements are taken is discussed. The experimental set-up is described and the measured results are presented.

The performance exhibited by dipole antennas constructed using conductive paper is presented in Chapter 5. The van der Pauw method is used to measure the paper conductivity; Appendix B offers a theoretical treatment of this method. Details associated with the construction of the conductive-paper antennas are also provided. The antennas are characterized over a range of conductivities through simulation in order to assess the performance associated with the current paper technology and identify a conductivity target to direct further development. The validity of the simulation model is tested via measurement of the gains exhibited by the constructed antennas. It should be noted that the contributions associated with Chapter 5 are largely unrelated to those associated with Chapters 3 and 4.

Chapter 6 concludes the dissertation. The key results associated with the research efforts presented in Chapters 3, 4 and 5 are summarized. Opportunities for future work in each research area are discussed.

Chapter 2

Background

The following sections will present background material relating to MIMO and UHF RFID systems. Where possible, the material will be introduced chronologically in an effort to add historical context to the discussion. Since the research conducted in the field of MIMO communication is quite extensive, Section 2.1.5 offers a review of some of the most significant and relevant literature.

2.1 MIMO Communication Systems

In order to meet the increasing demand for higher data rates, research in the area of wireless communication focuses primarily on discovering new ways to exploit the available frequency spectrum more efficiently. One method which has been gaining popularity over the past few decades is the use of multiple antennas at one or both ends of the communication link. Wireless systems which employ more than one antenna at both the transmitter and receiver are often referred to as MIMO systems. This is somewhat unfortunate since the term MIMO is relatively vague; it could be used to describe any system with multiple inputs and outputs. However, the name has most commonly been associated with wireless communication systems employing spatial multiplexing, which are discussed in Section 2.1.4. In any case, a

MIMO system relies on differences among the channels linking each pair of transmit and receive antennas in order to achieve better performance than the equivalent SISO system. While MIMO can be used to achieve multi-user communication, only single-user MIMO—in which there are only two radios communicating with each other—will be considered.

2.1.1 Single-antenna Systems

The majority of wireless communication systems employ a single antenna at both the transmitter and receiver. Assuming the transmit power to be limited, the performance of the resulting SISO system is typically governed by additive white Gaussian noise (AWGN) and the effects of multipath interference. Co-channel and adjacent channel interference, which are often significant in multiple access systems, will not be considered here. A typical wireless channel exhibits mobility, causing the associated multipath to be time-varying. As a result, the envelope of the signal appearing at the receiver fluctuates with time in accordance with periods of constructive and destructive interference. This phenomenon is known as fading. The effects of fading can significantly impact the reliability of a wireless link; for example, a particularly deep fade may result in a dropped call or a lost internet connection.

A SISO system is illustrated in Figure 2.1; note that Tx and Rx serve as shorthand for transmitter and receiver, respectively. The impact of fading on the received signal depends on the signal bandwidth and the degree of mobility associated with the channel. For now, it will be assumed that the signal bandwidth is narrow enough that the transfer function associated with the channel is approximately constant over the band. A wireless channel which exhibits this behaviour is commonly referred to as a flat fading channel. Employing a complex baseband signal notation, the received symbol b_{R} can be expressed in terms of the transmitted symbol a_{T} as

$$b_{\mathrm{R}} = h\, a_{\mathrm{T}} + n_{\mathrm{W}}, \tag{2.1}$$

where h is the narrowband discrete complex baseband channel impulse response and n_{W} is an AWGN signal. As indicated in Figure 2.1, fading in the channel causes $|b_{\mathrm{R}}|$ to fluctuate over time, where $|\cdot|$ denotes the magnitude operation.

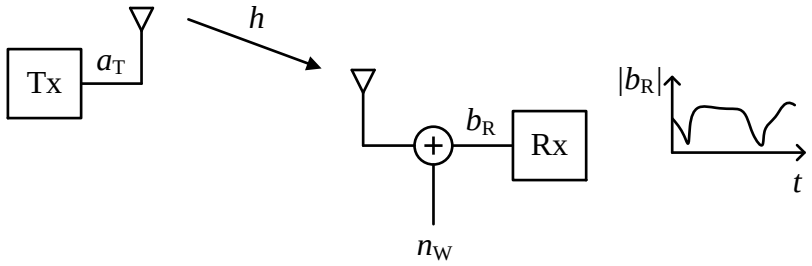

Figure 2.1: A SISO wireless communication system with AWGN and flat fading.

In many wireless communication systems, the transmitter has no knowledge of the channel and the receiver learns the channel via training symbols embedded within each block of data; such systems are commonly referred to as open-loop. A closed-loop wireless link can be achieved via some form of feedback from the receiver to the transmitter, but the added complexity associated with such a system is beyond the scope of the contributions presented in the following chapters. As a result, open-loop wireless links will be considered.

2.1.1.1 SISO Capacity

The Shannon capacity defines the maximum rate at which information can be communicated over a given channel with an arbitrarily low probability of error [19]. Although this limit cannot be achieved in practice, it can be closely approached under certain circumstances. For example, the application of turbo codes to an AWGN channel has been shown to yield information rates within 1 dB of the associated Shannon capacity [20].

For a time-invariant channel the associated capacity, denoted by C, can be expressed in bps/Hz as [19, 21]

$$C = \log_2 \left(1 + \frac{P_{\mathrm{T}}}{P_{\mathrm{N}}} |h|^2 \right), \tag{2.2}$$

where P_{T} is the transmit power and P_{N} is the noise power at the receiver. If the SNR at the receiver is much larger than unity, Equation 2.2 suggests that a change in SNR of 3 dB results in a corresponding change in capacity of approximately 1 bps/Hz.

The capacity of a fading channel is more difficult to quantify because h is a sample of a stochastic process. In this case the capacity can be defined in terms of the ergodic capacity, obtained by taking the mathematical expectation of the right-hand side of Equation 2.2, or in terms of the capacity with outage, which is the maximum data rate that can be achieved based on a certain probability that the receiver will be unable to decode the data without error [20]. Since the capacity evaluations carried out in the subsequent chapters assume static channel conditions, no further treatment of channel capacity in the presence of fading is given.

The capacity of a frequency-selective time-invariant channel can be evaluated with relative ease by observing that the complex baseband form of a frequency-flat channel impulse response is equivalent to its Fourier transform. Let $H(f)$ denote the transfer function of a frequency-selective channel, where f is frequency. The value $H(f_0)$ can be interpreted as the complex baseband form of a frequency-flat channel impulse response for an infinitesimally narrowband system operating at a particular frequency, f_0. Therefore, the capacity of a frequency-selective SISO channel is obtained by replacing h in Equation 2.2 with $H(f)$ and integrating over f [22, 23]:

$$C = \frac{1}{2W} \int_{-W}^{+W} \log_2 \left(1 + \frac{P_{\mathrm{T}}}{P_{\mathrm{N}}} |H(f)|^2 \right) df, \tag{2.3}$$

where W is the single-sided baseband channel bandwidth.

2.1.2 Spatial Diversity

There are two distinct ways in which multiple antennas can be employed to improve wireless radio performance. The first technique to be developed, spatial diversity, involves using multiple antennas at the receiver, transmitter or both in order to suppress the effects of fading, thereby improving the reliability of a wireless link. Spatial multiplexing, presented in Section 2.1.4, was developed more recently and requires multiple antennas at both the transmitter and receiver in order to take advantage of the effects of fading, thereby achieving higher channel capacities.

2.1.2.1 Receive Diversity

The concept of employing multiple receive antennas in order to improve the reliability of a wireless link has existed since the 1920s [24]. However, it did not truly come to fruition until the theory of spatial correlation—discussed in Section 2.1.3—was developed in the late 1960s [25, 26]. Consider a wireless communication system consisting of a single transmitter and two receivers at different physical locations, as illustrated in Figure 2.2(a). The values of h_1 and h_2 will be distinct because the paths linking the transmitter to each receiver are different. As a result, the fading exhibited by the received signals b_{R1} and b_{R2} will also be different. If the processes associated with h_1 and h_2 can be assumed to be independent, it is unlikely that both received signals will experience a deep fade simultaneously.

Now, suppose that the two receivers are replaced by a single receiver with two antennas which are separated by the same distance as before. This situation is depicted in Figure 2.2(b). If the received signals were combined in some clever way, the degree of fading experienced by the resulting signal (b_{R}) would be much less severe. This is the underlying concept of receive diversity. Systems incorporating receive diversity can also be referred to as single-input multiple-output (SIMO) systems.

Some of the most well-known combination techniques employed by receive

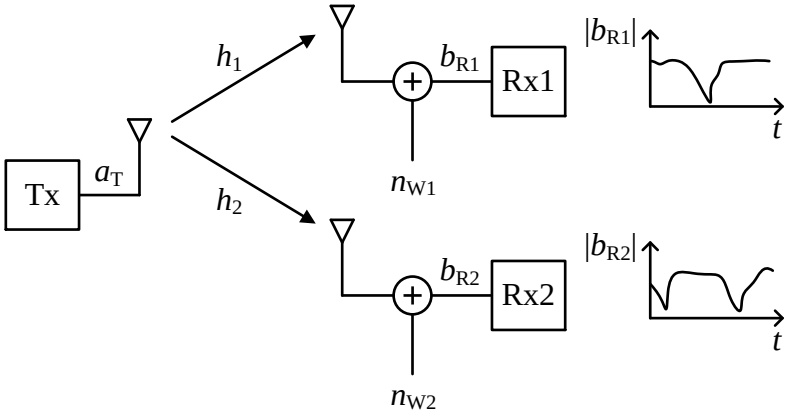

(a) A wireless communication system with a single transmitter and two separate receivers.

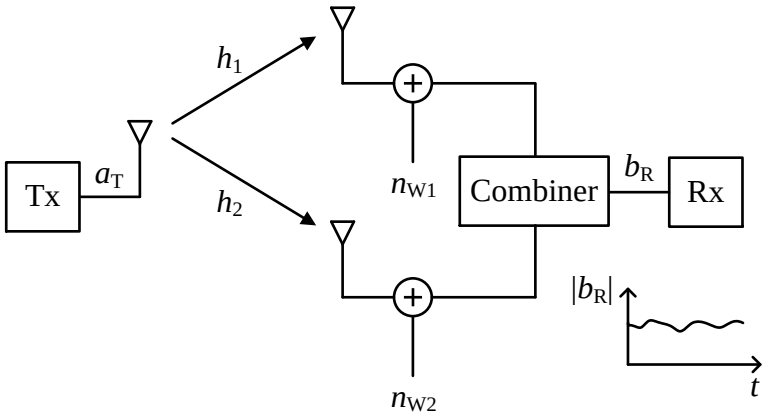

(b) A wireless communication system with receive diversity.

Figure 2.2: Diagrams illustrating the concept of receive diversity as a technique to mitigate the effects of fading.

diversity systems are: [24, 27]

- selection combining, where the receiver simply chooses the received signal with the highest instantaneous SNR;
- maximal ratio combining, which is optimal in the presence of fading and AWGN;
- equal gain combining, a mildly sub-optimal technique which is easier to implement than maximal ratio combining;

- optimum combining, which out-performs maximal ratio combining in the presence of co-channel and adjacent channel interference.

Of course, the effectiveness of each of these methods depends strongly on the degree of correlation associated with the fading; the best performance is achieved when h_1 and h_2 are statistically independent [25].

2.1.2.2 Transmit Diversity

Most wireless communication links are bi-directional, meaning that both of the communicating devices are transceivers. For example, consider the cellular telephone system in which a single base station provides service to each mobile within the corresponding cell. Communication from the base station to the mobile occurs on what is known as the forward link, while communication from the mobile to the base station occurs on the reverse link. It is assumed for the purpose of this discussion that the forward and reverse links occupy different frequency bands. Implementing receive diversity at the base station is feasible because there is ample physical space and the additional cost and complexity is effectively divided among all of the mobiles within the cell. However, it is not always practical to implement receive diversity at the mobile terminal as space tends to be limited, the additional cost can be prohibitive and any additional complexity tends to reduce the battery life of the unit. This was certainly the case in the mid-1990s [28]. Consequently, only the base station would be equipped for diversity.

This does not pose a problem for the reverse link; reliability is improved via receive diversity at the base station. Figure 2.3(a) depicts this situation for the case of two base station antennas. However, the forward link does not benefit from diversity in an open loop system because the transmitter has no knowledge of the channel. Even if the base station employs both of its antennas when transmitting and the associated signals fade independently, the mobile has no way of distinguishing between them

once they have superimposed at its antenna. This issue motivated research devoted to achieving transmit diversity in the absence of *a priori* channel knowledge [28].

Figure 2.3(b) illustrates a cellular link employing two-antenna transmit diversity on the forward link. Transmit diversity systems can also be referred to as multiple-input single-output (MISO) systems. In essence, multiple copies of the input symbols a_{T} are independently pre-coded and radiated from different antennas such that they can be separated after superposition at the receiving antenna. This allows the receiver to learn the associated channels and thus the reliability of the forward link can be improved in the same way as the reverse link without employing diversity at the mobile.

While a number of precoding methods have been developed to achieve transmit diversity, the Alamouti code is perhaps the most well-known. This code, which was published in 1998, achieves transmit diversity in a very elegant way; refer to the original paper by Alamouti for details [28]. Thus, transmit diversity came to fruition near the turn of the century.

2.1.2.3 Transmit/Receive Diversity

In wireless systems for which the added complexity associated with diversity is acceptable at both ends, transmit diversity can be implemented in conjunction with receive diversity [29]. Figure 2.4 illustrates a transmit/receive diversity system with two antennas at each end. Such a system can also be referred to as a MIMO system; however, as previously mentioned, this name is often attached to systems implementing spatial multiplexing. Conveniently, the benefits associated with the independent use of transmit and receive diversity stack with their combined use; the maximum diversity gain is given by the multiplication of the corresponding transmit and receive diversity gains [30]. The result is a wireless link which is very resilient to fading.

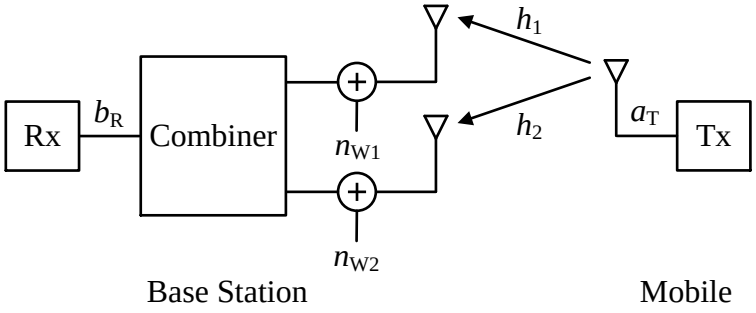

(a) A cellular system with receive diversity on the reverse link.

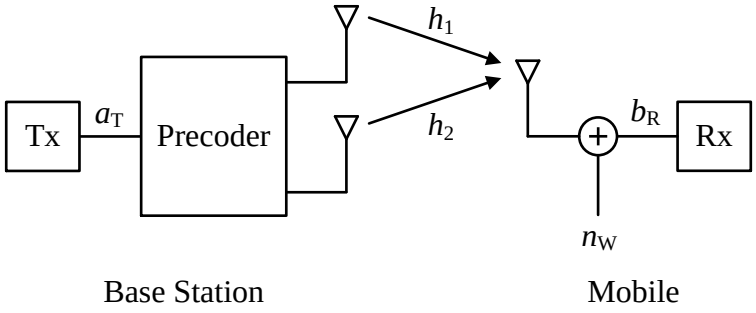

(b) A cellular system with transmit diversity on the forward link.

Figure 2.3: Employing transmit and receive diversity at the base station in a cellular system to improve reliability without significantly increasing the size, cost or complexity of the mobile.

2.1.3 Spatial Correlation

As previously mentioned, the signals present at each antenna in a diversity system would ideally be statistically independent, allowing the system to achieve the maximum possible diversity gain. Unfortunately, this is not the case in practice, as the associated antennas are often tightly spaced. The performance of both transmit and receive diversity is therefore limited by the degree of correlation between the antenna signals. Since the antennas are located at different points in space, this

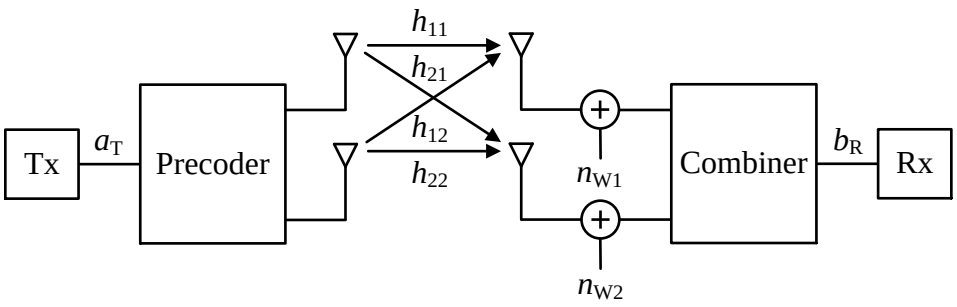

Figure 2.4: A wireless communication system with transmit/receive diversity.

correlation is commonly referred to as spatial correlation.

If the antennas are assumed to be isotropic point sources and the effects of mutual coupling are ignored, the degree of spatial correlation associated with a given antenna array is completely defined by the angular distribution of the incident multipath [25]. Spatial correlation is minimized when the received signal envelope is constant with respect to the angle of incidence and the phase is completely random. This is most often the case in environments exhibiting very dense multipath. Conversely, the degree of spatial correlation tends to be much higher in environments exhibiting sparse multipath since the associated angular distribution would strongly favour only a few directions-of-arrival (DOAs).

It has been demonstrated experimentally that as long as the spatial correlation coefficient is less than or equal to 0.7, spatial diversity continues to be effective [26]. Consider once again the example of a cellular system. For a mobile in an urban environment—which typically exhibits very dense multipath—an antenna spacing of one half-wavelength is usually sufficient. On the other hand, cellular base station antennas are typically mounted high above most scatterers and the associated angular distribution strongly favours the general direction of the mobile. As a result, antenna spacings on the order of 25 wavelengths might be required for good diversity performance [26].

The presence of an LOS component can have a significant impact on spatial correlation. LOS components tend to be much stronger than NLOS components since they do not incur reflection, diffraction or penetration losses and, by definition, they incur the lowest possible free space path loss. If an LOS path exists between the transmitter and the receiver, the associated angular distributions will be shaped such that they focus on the LOS directions. As a result, it is often found that NLOS environments characterized by Rayleigh fading experience lower spatial correlations than LOS environments, which are often characterized by Ricean fading [5].

2.1.4 Spatial Multiplexing

The fundamental principle of spatial diversity, whether it be at the receiver, transmitter or both, is to improve the reliability of a wireless link by averaging over a number of channel realizations. In a transmit/receive diversity system, this involves generating multiple copies of the original data stream, encoding the copies separately, transmitting them over the fading channel and combining the received signals back into a single data stream at the receiver. Suppose that instead of transmitting separately encoded copies of the same data stream, a completely independent data stream is transmitted from each antenna. Upon propagation through the channel, the data streams would become mixed and it would be the responsibility of the receiver to separate them in an effective manner. This is the basic premise of spatial multiplexing, developed in the mid-to-late 1990s [21, 31].

Consider the MIMO system depicted in Figure 2.5. It will again be assumed that all of the individual channels are frequency-flat. Expressing such a situation mathematically lends itself well to matrix notation. Let $\mathbf{a}_{\mathrm{T}} = [a_{\mathrm{T1}}, a_{\mathrm{T2}}]^T$, $\mathbf{n}_{\mathrm{W}} = [n_{\mathrm{W1}}, n_{\mathrm{W2}}]^T$ and $\mathbf{b}_{\mathrm{R}} = [b_{\mathrm{R1}}, b_{\mathrm{R2}}]^T$, where $(\cdot)^T$ denotes the transpose operation. The channel transfer matrix (CTM) can be expressed as

$$\mathbf{H} = \begin{bmatrix} h_{11} & h_{12} \\ h_{21} & h_{22} \end{bmatrix}, \tag{2.4}$$

in which case the communication scenario is described by

$$\mathbf{b}_{\mathrm{R}} = \mathbf{H}\mathbf{a}_{\mathrm{T}} + \mathbf{n}_{\mathrm{W}}. \tag{2.5}$$

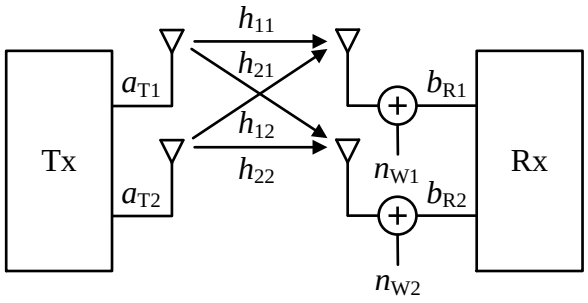

Figure 2.5: A MIMO spatial multiplexing system.

The difficulty with spatial multiplexing arises due to coupling between the independent data streams which inevitably occurs during propagation through the channel. Mathematically, this is attributed to the off-diagonal terms in the CTM: h_{21} and h_{12} in this case. If these terms were forced to zero, the CTM would be diagonal and the system could be expressed in terms of uncoupled SISO channels. In general, this issue can be approached through singular value decomposition [31]:

$$\mathbf{H} = \mathbf{U}\boldsymbol{\Xi}\mathbf{V}^{H}, \tag{2.6}$$

where $\boldsymbol{\Xi}$ is a diagonal matrix consisting of the singular values of the CTM, $\mathbf{U}$ and $\mathbf{V}$ are unitary matrices consisting of the singular vectors of the CTM and $(\cdot)^{H}$ denotes the conjugate transpose operation [32]. Substituting Equation 2.6 into Equation 2.5 yields

$$\mathbf{b}_{\mathrm{R}} = \mathbf{U}\boldsymbol{\Xi}\mathbf{V}^{H}\mathbf{a}_{\mathrm{T}} + \mathbf{n}_{\mathrm{W}}. \tag{2.7}$$

Multiplying both sides of this expression by $\mathbf{U}^{H}$ gives

$$\mathbf{U}^{H}\mathbf{b}_{\mathrm{R}} = \boldsymbol{\Xi}\mathbf{V}^{H}\mathbf{a}_{\mathrm{T}} + \mathbf{U}^{H}\mathbf{n}_{\mathrm{W}} \tag{2.8}$$

since $\mathbf{U}^{H}\mathbf{U} = \mathbf{U}\mathbf{U}^{H} = \mathbf{I}$, where $\mathbf{I}$ is the identity matrix. The system can then be written in diagonal form as [29]

$$\mathbf{b}'_{\mathrm{R}} = \boldsymbol{\Xi}\mathbf{a}'_{\mathrm{T}} + \mathbf{n}'_{\mathrm{W}}, \tag{2.9}$$

where the following transformations have been applied:

$$\mathbf{a}'_{\mathrm{T}} = \mathbf{V}^{H}\mathbf{a}_{\mathrm{T}}; \tag{2.10}$$

$$\mathbf{n}'_{\mathrm{W}} = \mathbf{U}^{H}\mathbf{n}_{\mathrm{W}}; \tag{2.11}$$

$$\mathbf{b}'_{\mathrm{R}} = \mathbf{U}^{H}\mathbf{b}_{\mathrm{R}}. \tag{2.12}$$

The MIMO channel can thus be expressed in terms of two uncoupled spatial sub-channels [31]. Mathematically, these are written as

$$b'_{\mathrm{R}1} = \xi_1\, a'_{\mathrm{T}1} + n'_{\mathrm{W}1} \tag{2.13}$$

and

$$b'_{\mathrm{R}2} = \xi_2\, a'_{\mathrm{T}2} + n'_{\mathrm{W}2}, \tag{2.14}$$

where ξ_1 and ξ_2 are the singular values of $\mathbf{H}$.

The columns of $\mathbf{U}$ and $\mathbf{V}$ are composed of the singular vectors of $\mathbf{H}$. The transformations expressed by Equations 2.10–2.12 therefore involve scaling the origi-

nal transmitted, received and noise signals by the complex conjugates of the singular vectors of $\mathbf{H}$. Due to the unitary nature of both $\mathbf{U}$ and $\mathbf{V}$, the power levels associated the signals are unchanged. Applying such a transformation to AWGN is immaterial; the statistics of $\mathbf{n}'_{\mathrm{W}}$ are identical to those of $\mathbf{n}_{\mathrm{W}}$ [29]. Using the singular vectors to transform the transmitted and received signals can be interpreted in the context of beamforming [33]. The radiation patterns of the transmit and receive antenna arrays are steered and phased for each data stream such that the off-diagonal terms in $\mathbf{H}$ are forced to zero. Figure 2.6 illustrates the resulting communication system.

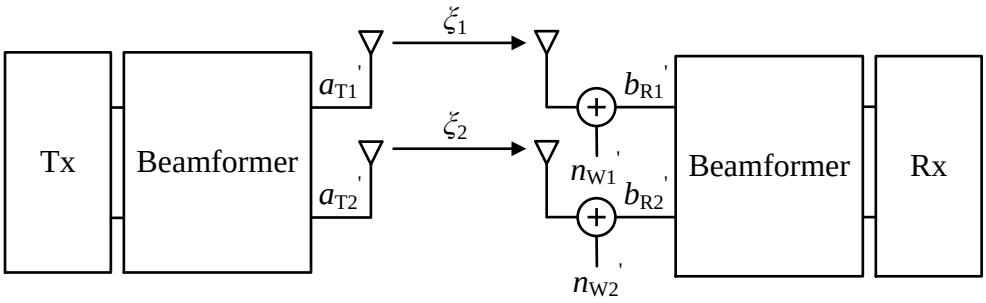

Figure 2.6: A MIMO spatial multiplexing system with beamforming which reduces the channel to a pair of spatial subchannels.

The performance improvements that can be achieved through spatial multiplexing are largely governed by the singular values of the CTM. Ideally, all of the singular values would be equal, implying that the maximum number of spatial subchannels are available and can be exploited with equal effectiveness. The singular value spread is often quantified by the condition number, expressed as [32]

$$\mathrm{cond}(\mathbf{H}) = \frac{\xi_{\max}}{\xi_{\min}} \tag{2.15}$$

where $\xi_{\max}$ and $\xi_{\min}$ are the maximum and minimum singular values of $\mathbf{H}$, respectively. A condition number of unity implies that all of the singular values are equal and the CTM is perfectly invertible, whereas a condition number which approaches infinity

suggests that the CTM is rank-deficient. Using the condition number as a metric for the performance of spatial multiplexing is most effective for systems employing two antennas at both the transmitter and receiver, in which case only two singular values exist. Otherwise, care must be taken as the additional singular values are unaccounted for.

2.1.4.1 MIMO Capacity

The capacity of the MIMO channel depicted in Figures 2.5 and 2.6 can be expressed as the sum of the capacities associated with the spatial subchannels expressed in Equations 2.13 and 2.14: [29]

$$C = \log_2\left(1 + \frac{P_\mathrm{T}}{2\,P_\mathrm{N}}\,\xi_1^2\right) + \log_2\left(1 + \frac{P_\mathrm{T}}{2\,P_\mathrm{N}}\,\xi_2^2\right). \tag{2.16}$$

Since the system is assumed to be open loop, the transmit power is divided equally between the two antennas. If the condition number of the CTM is unity, $\xi_1 = \xi_2$ and the received SNR can be expressed as

$$\rho = \frac{P_\mathrm{T}}{P_\mathrm{N}}\,\xi_1^2. \tag{2.17}$$

The channel capacity associated with this ideal case is

$$C = 2\log_2\left(1 + \frac{\rho}{2}\right). \tag{2.18}$$

Extending to the case of M antennas at the transmitter and receiver gives

$$C = M\log_2\left(1 + \frac{\rho}{M}\right). \tag{2.19}$$

This expression is of enormous significance; in the ideal case of a perfectly invertible CTM, the achievable spectral efficiency of a MIMO system increases almost linearly

with the number of antennas. If $\rho/M \gg 1$, Equation 2.19 suggests that a 3 dB change in SNR results in a corresponding change in capacity of approximately M bps/Hz.

The ability of a spatial multiplexing system to approach the ideal capacity expressed in Equation 2.19 is dictated by many of the same factors which affect the performance of spatial diversity systems. A high degree of spatial correlation will degrade the achievable MIMO capacity, which implies that MIMO is most effectively used in NLOS environments exhibiting rich scattering. Sparse multipath or the presence of a strong LOS component can result in a rank-deficient CTM, which significantly reduces the achievable MIMO capacity. However, unlike for spatial diversity, low spatial correlation does not guarantee good spatial multiplexing performance [34]. Even if the antenna signals are completely uncorrelated, the presence of what are known as pinholes or keyholes—addressed in Section 2.1.5—can drastically reduce the achievable MIMO capacity. In the absence of these impairments, lowering the degree of spatial correlation associated with the channel improves MIMO capacity.

The capacity of a MIMO channel can also be expressed in matrix form as [21, 35]

$$C = \log_2 \det \left[\mathbf{I} + \frac{P_{\mathrm{T}}}{M_{\mathrm{T}}\, P_{\mathrm{N}}} \mathbf{H}\mathbf{H}^H \right], \tag{2.20}$$

where M_{T} is the number of transmitting antennas. This expression is obtained based on the eigenvalue equation for $\mathbf{H}\mathbf{H}^H$, since the associated eigenvalues are simply the squared singular values of $\mathbf{H}$ [29]. If the entries of the CTM are frequency-selective, the associated MIMO capacity can be expressed as [22, 23]

$$C = \frac{1}{2W} \int_{-W}^{+W} \log_2 \det \left[\mathbf{I} + \frac{P_{\mathrm{T}}}{M_{\mathrm{T}}\, P_{\mathrm{N}}} \mathbf{H}(f)\mathbf{H}(f)^H \right] df, \tag{2.21}$$

for the same reasons as those given for Equation 2.3.

2.1.5 MIMO Literature Review

Some of the earliest research relating to the capacity of MIMO systems was conducted by Winters in the late 1980s [36]. However, it was the seminal paper by Foschini and Gans [21] along with the mathematical developments of Telatar [31, 37] which truly sparked interest in the area in the mid-to-late 1990s. These contributions focused on the achievable capacity gains associated with the use of multiple transmit and receive antennas in deterministic or uncorrelated Rayleigh fading channels which were assumed to be frequency-flat and known only at the receiver.

In cases where the transmitter does have access to *a priori* channel knowledge, higher capacities can be achieved. This is accomplished through adaptive power allocation among the transmit antennas. The allocation is based on an elegant water-filling solution [31, 38, 39] which can be readily implemented in practice. However, in cases where the received SNR is high and the CTM is well-conditioned, the benefits of channel knowledge at the transmitter are negligible.

The influence of spatial correlation on MIMO capacity has been previously investigated [40, 41]. As might be expected, these contributions revealed that correlation among the antenna signals reduces the achievable MIMO capacity, particularly if the associated correlation coefficient exceeds 0.5. Mutual coupling among the antennas at the transmitter and receiver would be expected to add to the degree of spatial correlation and degrade performance. However, it has been shown that mutual coupling can actually increase MIMO capacity in certain circumstances [42, 43]. This can be explained as follows: the radiation pattern of a given antenna is distorted due the presence of other antennas within its near-field region. Depending on the geometries associated with the receive and transmit antenna arrays, the distortion will be different for each antenna. This is known as pattern diversity and serves to reduce the correlation associated with the antenna signals, thereby increasing the achievable MIMO capacity.

As previously mentioned, the presence of pinholes or keyholes can drastically reduce the capacity of a MIMO system, regardless of the degree of spatial correlation exhibited by the channel [34, 44–46]. This is commonly referred to as the keyhole effect. Consider a transmitter and receiver located in separate regions, each exhibiting dense multipath such that the associated angle spreads are roughly uniform and spatial correlation is low. If the regions are linked by a single or strongly dominant path, the resulting CTM will be inherently rank-deficient, greatly limiting the effectiveness of spatial multiplexing. Fortunately, the keyhole effect rarely occurs in practice [35].

One drawback to the implementation of MIMO systems is that each antenna must be connected to a complete RF chain, which increases the cost and complexity of the associated devices. Based on channel conditions, some of the antennas may not be necessary to achieve the corresponding MIMO capacity. For example, under circumstances where the CTM is rank-deficient, at least one of the antennas will be useless in the context of spatial multiplexing. This issue can be addressed through the implementation of antenna selection [47, 48], which involves constructing devices with more antennas than RF chains. By switching the available RF chains to those antennas which result in the highest capacity improvements at a given time, RF resources are used more efficiently.

The capacity of frequency-selective MIMO channels is considerably more complex to analyse; the channel can either be modelled as a Toeplitz matrix based on the number of resolvable multipath components [38], or as a set of frequency-flat channel matrices corresponding to a sufficient number of discrete narrowband frequency intervals [49]. As with SISO systems, MIMO systems in which the bandwidth is wide enough that the associated channel is frequency-selective exhibit increased resilience to fading relative to narrowband systems; this is usually measured as an increase in outage capacity. However, the ergodic capacity of a frequency-selective MIMO channel has been shown to be theoretically higher than for flat fading [38, 49]. This

is because the ability to resolve multipath components provides an opportunity for additional diversity between the individual channels. A significant increase in outage capacity and a small increase in ergodic capacity for frequency-selective channels have been observed during MIMO channel measurements [22].

Of course, the capacities reported in MIMO research can only be achieved if there exists a receiver structure capable of decoding MIMO signals. The Bell-labs Layered Space-Time (BLAST) architecture proposed by Foschini [50] defines just such a receiver. This design, commonly referred to as diagonal BLAST (D-BLAST) was intended for open loop MIMO systems operating in frequency-flat Rayleigh fading environments and achieved signal recovery through successive interference cancellation. A simplification to D-BLAST was later published in the form of vertical BLAST (V-BLAST) [51], which has become a standard receiver structure in MIMO research and implementation. It has also been shown that V-BLAST can be modified for operation under frequency-selective fading conditions [52]. The effectiveness of BLAST was investigated in a measurement campaign, the results of which clearly demonstrated that significant improvements in spectral efficiency can be achieved through the application of MIMO with a BLAST receiver [53].

In addition to BLAST, a variety of space-time coding techniques exist which are applicable to both spatial diversity and spatial multiplexing systems. For example, the Alamouti code is a space-time block code applicable to spatial diversity systems. Relatively little attention will be given to these techniques here; the interested reader is referred to a text on the subject [29] and a tutorial paper which offers of brief summary of some of the techniques along with a literature survey [39]. For space-time coding to be effective, the codes must span across the individual branches of the multi-antenna system. In the case of spatial multiplexing, this tends to reduce the independence associated with the data streams, thereby limiting capacity. Initially, this would seem disadvantageous; however, the resulting similarities between

the data streams can be used to achieve spatial diversity gains [39]. As a result, the bit error rate (BER) of the system can be reduced for a given signalling scheme and SNR, increasing the reliability of the link. Alternatively, the improved BER performance can be leveraged to implement higher-level modulation schemes, indirectly increasing the bit rate of the system [39]. Thus, a combination of spatial diversity and spatial multiplexing is often applied in practice; the associated tradeoffs have been investigated [30, 54].

The performance of a MIMO system is strongly influenced by the environment in which it is operated. As such, a wide variety of spatial channel models have been developed in the literature; an overview of these models is presented in [55]. Although the work presented in the subsequent chapters deals exclusively with ray tracing, most communication environments are stochastic in nature. Consequently, an understanding of the associated channel models is critical when simulating MIMO channels.

The effects of antenna array geometry on MIMO capacity in a purely LOS environment have been thoroughly investigated [56–60]. This work has primarily been devoted to characterizing optimal antenna spacings or developing antenna array geometries which improve the achievable MIMO capacity despite the highly correlated nature of the environment. The associated contributions are largely applicable to tower-to-tower communication links in which channel conditions are static and strongly LOS dominated. Considerable attention has also been given to the design of antenna arrays for operation in environments exhibiting both a strong LOS component and fading [61–64]. In this case, the channel is either characterized by a Ricean distribution, a Rayleigh distribution coupled with geometrically obtained LOS components or geometrically through the use of ray tracing. Antenna array design in NLOS (Rayleigh fading) environments has been investigated as well [12, 13, 15, 65–67]. These contributions were largely concerned with the effects of the antenna array topology

and element polarization on performance.

More generally, the performance of MIMO systems in outdoor environments has been investigated both theoretically [68] and experimentally [22]. These studies identified some of the key issues associated with a variety of outdoor MIMO channels and offered either performance predictions or measured results for each. Similar studies have been conducted for indoor environments [5,6,69], where measured results are more readily obtained and used to assess the accuracy of indoor channel models.

In addition to single user systems, MIMO is also applicable to multiple access systems. For instance, mobile communication standards such as WiMAX and LTE employ MIMO technology to provide service to multiple users [70]. The capacity formulations for multiuser MIMO are considerably more complex than for the single user case; Goldsmith et al. present an excellent overview of some the research conducted in this area [35]. Relatively little attention will be given to these systems here; however, it is interesting to note that the interference which the users present to one another can be mitigated by employing antenna spacings on the order of a symbol wavelength—defined as the physical length of a single symbol propagating through space—instead of a carrier wavelength. This is based on a similar result obtained for code division multiple access (CDMA) systems and has been proven both theoretically [71] and experimentally [72]. This is primarily applicable to systems where the symbol wavelength is relatively short, such as ultra-wideband (UWB) MIMO systems which have been gaining popularity in recent years [73].

2.2 UHF RFID Systems

Automatic identification is essential in a variety of industries such as retail, automotive, shipping and storage. In addition to optical character recognition (barcodes), biometric procedures (voice recognition, fingerprinting, etc.) and smart cards,

RFID technology has found widespread application in these and other industries over the past several decades [74].

An RFID system consists of a tag—also known as a transponder—which is typically affixed to an object, animal or person of interest, along with a reader—also known as an interrogator—which identifies and communicates with the tag via wireless link. Most industrial RFID systems operate in either the low frequency (LF) band from 125–134 kHz or the high frequency (HF) band at a centre frequency of 13.56 MHz [75]. The primary disadvantage of operation in these bands is that the associated wavelengths are relatively large, prohibiting the design of resonant tag antennas. As a result, near-field communication between electrically small antennas is employed. More specifically, information transfer is often achieved via inductive coupling between coils at the reader and tag. The relative strengths of the near-field components fall off with r^{-3}, where r is the radial distance from the reader to the tag, thereby limiting the range of the system from a few centimetres to, at most, 1 m [7,76]. Conversely, far-field components fall off with r^{-1}, suggesting that operation in a higher frequency band would significantly increase the achievable range. Extensive research has therefore been conducted in order to develop and improve RFID systems operating in the UHF band [77]. Since the antenna development presented in Chapter 5 is intended for UHF RFID applications, LF and HF RFID systems are not considered further.

UHF RFID systems are interesting in that the tags often do not feature a transmitter. Communication from the tag to the reader is instead achieved via modulation of the radar cross-section (RCS) presented by the tag to the reader. This is usually accomplished by adjusting the load impedance connected to the tag antenna in accordance with a message signal [78]. In the interest of reducing costs and maintenance considerations, UHF RFID tags are typically passive, meaning that they do not feature an independent power source [7]. A portion of the RF power

incident from the reader is instead converted to a direct current (DC) voltage within the tag IC, which, when sufficiently large, activates the remaining circuitry. The use of active—or battery-assisted—UHF RFID tags results in longer read ranges due either to the presence of a transmitter or the fact that they are capable of using all of the incident RF power from the reader for communication. It is also much easier to incorporate sensors into active tags, permitting the development of RFID-based sensor networks [79]. Regardless, active tags are far less applicable than their passive counterparts [7] and will not be considered further. Details regarding the operation of passive UHF RFID tags is presented in Section 2.2.1.

The concept of scattered modulation dates back to World War II when radar systems were first developed. Friendly aircraft were outfitted with backscatter modulation technology so that they could be distinguished from enemy aircraft on radar; this was known as the "identify friend or foe" (IFF) system [76, 80]. Covert listening devices based on backscatter modulation were developed for the purposes of espionage in the mid-1940s [80]. The first academic research devoted to communication via modulated backscatter was published by Stockman in 1948 [81] and proposed the mechanical adjustment of elaborate radar targets to achieve the modulation. A series of patents and related theoretical contributions throughout the 1950s and 1960s—for example, the development of the theory of loaded scatterers in 1964 [82]—culminated in the development of the first passive UHF RFID system for monitoring livestock in 1975 [83, 84]. Since then, UHF RFID has been continually improved and developed for various industrial and academic applications. Further details regarding the history of RFID technology can be found in a number of overview papers [7, 80, 84], while the handbook by Finkenzeller offers a comprehensive introduction to RFID systems [74].

2.2.1 Passive UHF RFID

A simplified block diagram depicting the RF details associated with a passive UHF RFID system is presented in Figure 2.7. The RFID reader includes a baseband processor which drives an internal transmitter and interprets data from an internal receiver. A circulator ensures that the transmission signal is delivered exclusively to the reader antenna. This signal includes periods of continuous wave (CW) behaviour to power nearby tags and modulation based on querying data intended for the tags once they have been activated [77, 78]. In North America, the centre frequency of the transmission signal must fall within either the 915 MHz, 2.4 GHz or 5.8 GHz industrial, scientific and medical (ISM) bands [74]. Data rates on the order of hundreds of kbps are typical of passive UHF RFID systems and the effective isotropic radiated power (EIRP), denoted by P_{EIRP}, is limited to 4 W in North America [80]. The EIRP can be expressed as

$$P_{\text{EIRP}} = P_{\text{T}}\, G_{0,\text{reader}}, \tag{2.22}$$

where $G_{0,\text{reader}}$ is the maximum gain exhibited by the reader antenna. For example, if the reader antenna is a half-wavelength dipole with a maximum gain of approximately 2.15 dBi, the transmit power must not exceed approximately 2.44 W.

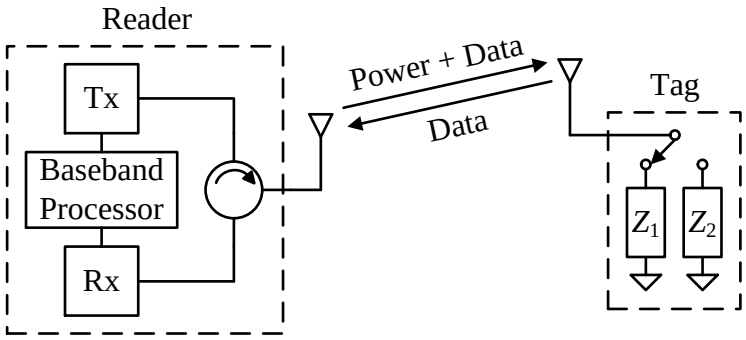

Figure 2.7: A block diagram representing the RF details associated with a passive UHF RFID system based on load modulation.

Once a tag is close enough to the reader that there is sufficient RF energy to activate the associated IC, communication between the tag and reader is possible. Upon activation and reception of the reader query, the tag responds by switching between distinct antenna load impedances, denoted by Z_1 and Z_2, in accordance with the associated response data. The resulting variation in the load reflection coefficient experienced by the tag, denoted by Γ_{tag}, modulates the backscatter from the tag. At the reader, the backscattered signal passes through the circulator to the receiver for detection. In situations where numerous tags may be present, an anticollision scheme such as time division multiple access (TDMA) can be employed to avoid interference [74].

Two distinct forms of backscatter modulation are typically employed by passive UHF RFID tags. Amplitude shift keying (ASK) involves selecting Z_1 and Z_2 such that the magnitude of Γ_{tag} is varied, while phase shift keying (PSK) is obtained when Z_1 and Z_2 are such that only the phase of Γ_{tag} is varied. The use of ASK will be considered as it is simpler and tends to offer superior range performance than PSK; the interested reader is referred to the text by Curty et al. [7] for further details regarding backscatter modulation techniques.

Figure 2.8 presents a more detailed block diagram of a passive UHF RFID tag employing ASK for backscatter modulation. As the tag approaches a reader, the incident RF energy is collected by an antenna and matching network external to the tag IC. A voltage multiplier consisting of cascaded clamping and rectification circuits [7] converts the RF voltage at its input to a DC voltage of greater magnitude at its output [85]. Provided that there is enough available RF power, the demodulator, control logic and memory circuits become active. For example, 1.2 V at the output of the voltage multiplier is typically sufficient to activate the remaining tag circuitry [7]. The demodulator is then capable of relaying the query signal from the reader to the control logic circuitry. In this example, the response from the tag is achieved

via toggling a switch which shorts the input terminals of the IC in accordance with binary data read from memory. Relating this situation to that depicted in Figure 2.7, Z_1 is the input impedance of the tag IC, denoted by $Z_{\mathrm{IC}} = R_{\mathrm{IC}} + jX_{\mathrm{IC}}$, and Z_2 is 0 Ω.

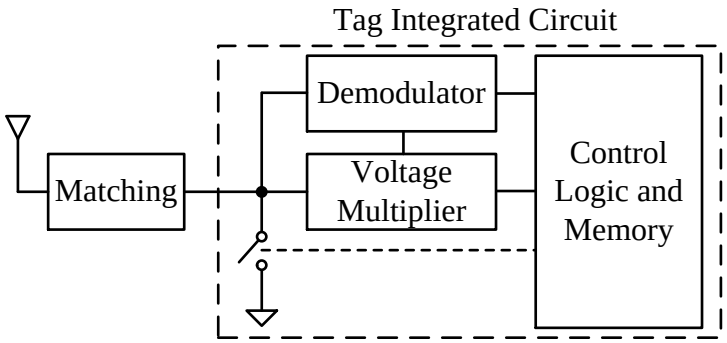

Figure 2.8: A more detailed block diagram for a passive UHF RFID tag employing ASK for backscatter modulation.

The operating range of a passive UHF RFID tag is ultimately dictated by the amount of incident RF power necessary to fully activate the tag IC. Numerous research efforts have been devoted to improving the efficiency with which the circuitry internal to the tag IC makes use of the available RF power [85–87]. Such circuit-level details are beyond the scope of this discussion. The RF details which determine the range performance of the tag are instead emphasized.

Let P_{min} denote the minimum incident RF power required to activate the tag IC. Furthermore, define the RFID read range as the maximum range from the reader at which the tag is fully active. This range, denoted by r_{max}, is obtained via reformulation of Friis' transmission equation [77]:

$$r_{\mathrm{max}} = \frac{\lambda}{4\pi}\sqrt{\frac{P_{\mathrm{EIRP}}\, G_{0,\mathrm{tag}}}{P_{\mathrm{min}}}}\kappa, \tag{2.23}$$

where λ is the free space wavelength, $G_{0,\mathrm{tag}}$ is the maximum gain exhibited by the tag antenna and κ is the power transmission coefficient from the tag antenna and matching network to the tag IC. If $Z_{\mathrm{MA}} = R_{\mathrm{MA}} + jX_{\mathrm{MA}}$ denotes the input impedance

of the matching network and antenna taken from the terminals of the tag IC, κ is given by [75, 77]

$$\kappa = \frac{4\, R_{\mathrm{MA}}\, R_{\mathrm{IC}}}{\left|Z_{\mathrm{MA}} + Z_{\mathrm{IC}}\right|^2}. \tag{2.24}$$

The power transmission coefficient achieves its maximum value of unity when $Z_{\mathrm{MA}} = Z_{\mathrm{IC}}^{\dagger}$, where $(\cdot)^{\dagger}$ denotes the complex conjugate operation. However, it is difficult to achieve both a conjugate impedance match at the input terminals of the tag IC and a high value of $G_{0,\mathrm{tag}}$. The RFID tag antenna designer must strike a balance between these and other competing factors in order to achieve the best RFID read range performance [77].

Although a suitable impedance match can be achieved using lumped components, transmission line techniques and specialized antenna designs are more common in practice as they reduce the cost and fabrication complexity associated with the tags. For example, matching can be achieved by driving a dipole by an appropriately designed T-match or inductively coupled loop [75]. Miniaturization of the tag antenna is also desirable and is popularly achieved via meandering. Meander-line dipole antennas with various feed and matching arrangements are popular passive UHF RFID tag design solutions [75, 77].

Chapter 3

Improving In-room MIMO Capacity Using Elevation-directional Access Point Antennas: Simulations

MIMO technology has been employed in a number of wireless communication applications in order to meet the ever-increasing demand for mobile data. There has recently been a trend toward installing a larger number of cellular base stations [1] and WLAN APs over the same physical coverage area in order to meet increasing capacity demands. It is therefore possible that in the near future a MIMO-equipped WLAN AP may be primarily responsible for providing service to a single room.

The in-room MIMO channel—where a WLAN AP and a user with a PD occupy the same room—presents an interesting communication environment in that there are often strong LOS components linking the AP and PD antennas and many of the dominant NLOS components arise due to wall reflections [2–4]. The impact of LOS components in MIMO systems is two-fold: an LOS situation typically means

a higher SNR at the receiver [88], while measurements have shown that it also leads to a higher degree of spatial correlation in both frequency-flat [5] and frequency-selective [6] fading channels, which limits the achievable spatial multiplexing gain. Often, the SNR increase associated with the presence of a strong LOS component outweighs the higher degree of spatial correlation, resulting in a net increase in channel capacity [88]. On the other hand, the relative multipath richness exhibited by an NLOS situation results in less spatial correlation and measurements have demonstrated that for the same level of SNR the capacity of a MIMO channel may be improved by artificially obstructing the LOS components [22, 69].

The goal of this research is to determine whether or not replacing the typically non-directional WLAN AP antennas with θ-directional antennas which emphasize wall-reflected NLOS components is viable as a simple way to improve in-room MIMO capacity. APs with non-directional antennas benefit from receiving multipath components equally from all (or most) directions, while APs using θ-directional antennas enjoy conditions which approximate an NLOS situation, where the high antenna gains compensate for the relatively low power levels associated with the wall-reflected multipath components. Each situation is illustrated in Figure 3.1; the non-directional AP antennas are depicted as isotropic and the weights of the LOS and NLOS rays express the associated power levels. Note that the θ-directional AP antennas are omnidirectional in azimuth (ϕ) in order to avoid sectoring which can degrade MIMO communication performance [89]. In order to realize such a radiation pattern and allow different main lobe θ-directions to be explored, vertically oriented linear-phased-array AP antennas will be considered and the associated results will be compared with those obtained for single-element AP antennas.

The impact of different antenna configurations on MIMO performance has been investigated in both indoor and outdoor environments [12, 13, 15]. The application of directional antennas to indoor and outdoor-indoor communication systems

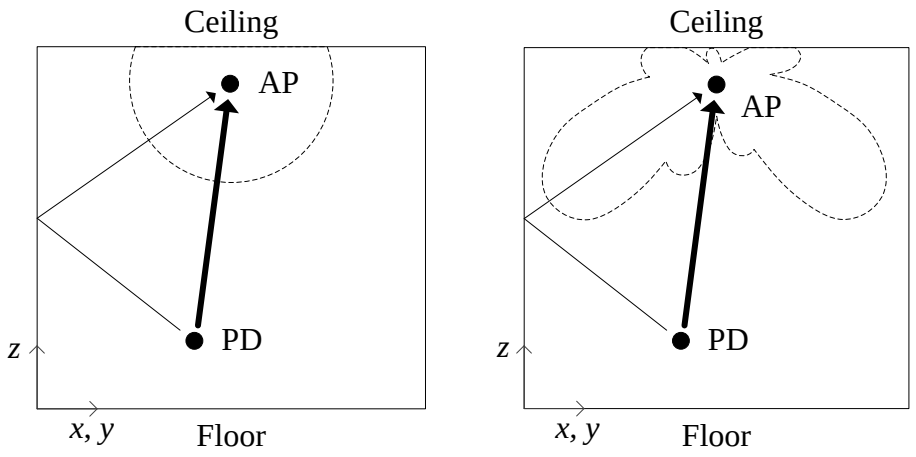

(a) Non-directional AP antennas. (b) Elevation-directional AP antennas.

Figure 3.1: An illustration of the AP configurations under consideration, where z is the vertical direction within the room.

was explored in cases where the location of the receiver was known or could be estimated by the transmitter [16,17]. The quasi-predictable directions-of-arrival (DOAs) associated with some of the dominant in-room multipath components—such as the aforementioned wall-reflected NLOS components—suggest that performance can be improved through the use of AP antennas with static θ-directional radiation patterns; adaptation of the AP antenna radiation patterns based on channel conditions will not be considered. The use of phased arrays has been investigated in an isolated corridor in the context of applying adaptive beamforming for each independent data stream to increase MIMO capacity [14]. In contrast, phased arrays will be used here to realize AP antennas with directional radiation patterns which take advantage of the nature of the in-room MIMO channel in order to improve communication performance throughout the room.

3.1 In-room MIMO System Model

This section outlines details associated with the in-room MIMO system model. Software was developed in MATLAB® in order to implement this model. Refer to

Appendix A for a complete code listing.

3.1.1 In-room Environment

Figure 3.2 depicts the communication environment consisting of a room which contains the AP and a PD. The dimensions of the room in the x, y and z directions are given by d_x, d_y and d_z, respectively. The AP is mounted at a distance of $d_z - d_{\mathrm{AP}}$ below the centre of the ceiling, where d_{AP} is the distance from the AP to the floor, and a PD is located somewhere in the room at a height of d_{PD} above the floor. The effects of mobility on communication performance are not considered as the channel is assumed to be quasi-static. The room is completely isolated, meaning that everything other than a surface reflection is ignored. This assumption is reasonable given the relative proximity of the AP and PD. With the exception of the communicating devices, the room is also assumed to be empty. The goal here is not to accurately model a particular room and develop an optimal AP design, but to demonstrate that performance may be improved for a large subset of practical rooms. Furthermore, the dominant shape of a room is most often a rectangular parallelepiped (a box), suggesting that the geometry of Figure 3.2 is representative of the majority of practical rooms.

The PD and the AP both feature M antennas. Since omnidirectional coverage throughout the room is desired, the shape of the AP antenna array should be symmetric in x and y [40]. As a result, the AP antennas are assumed to be arranged in a uniform circular array (UCA) oriented within the xy-plane, with adjacent antennas separated by s_{AP}. The radius of the AP, r_{AP}, is therefore given by

$$r_{\mathrm{AP}} = \frac{s_{\mathrm{AP}}}{\sqrt{2\left(1-\cos\left(\frac{2\pi}{M}\right)\right)}}. \tag{3.1}$$

The associated antennas are evenly spaced in azimuth, with the first antenna being

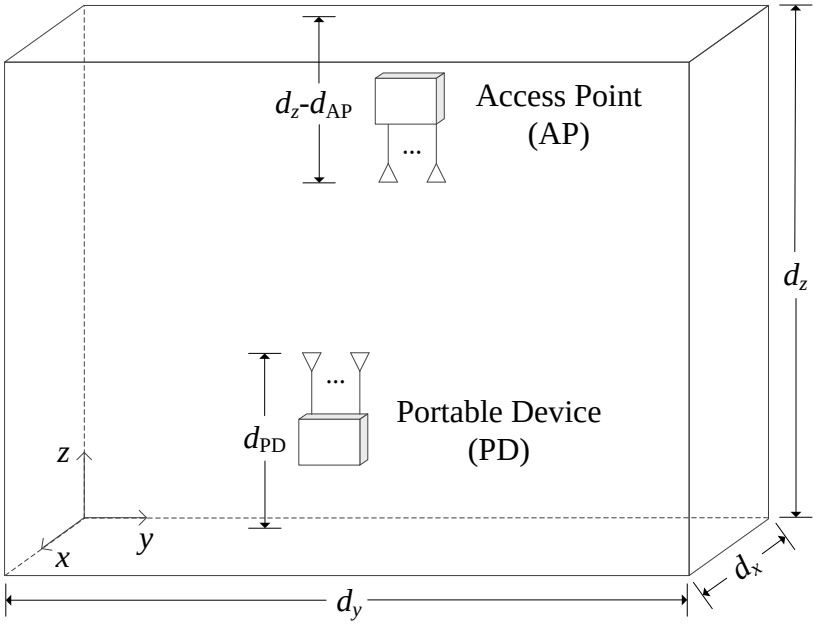

Figure 3.2: An illustration of the in-room MIMO communication system environment which depicts the locations and orientations of the AP and a PD.

placed at $\phi = 0°$. For the sake of simplicity, the PD antennas are similarly arranged, with adjacent antennas separated by s_{PD}. In the case of the AP, each antenna may consist of a single radiating element, such as a half-wavelength dipole, or a vertically oriented linear-phased-array of N radiating elements with a progressive phase shift of β; each of these situations is depicted in Figure 3.3 for $M = 3$. The PD array is always comprised of single-element antennas and the associated geometry resembles Figure 3.3(a) but with s_{PD} and r_{PD} in place of s_{AP} and r_{AP}, respectively.

3.1.2 Antennas

Since the MIMO performance results are to be directly compared for different AP antenna types, the antennas themselves must be accurately modelled in an electromagnetic sense. In order to properly account for the reflections associated with the NLOS paths linking the PD to the AP, the antennas are characterized in terms

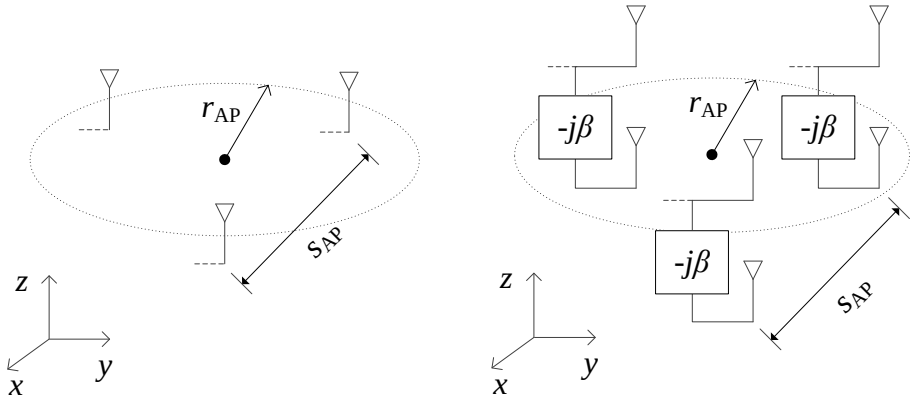

(a) Single elements. (b) Linear phased arrays ($N = 2$).

Figure 3.3: AP geometries for an $M = 3$ MIMO example.

of field parameters as opposed to power-based parameters such as gain and radiation pattern. More specifically, a given antenna will be primarily modelled by its vector effective length, which serves to uniquely define it in terms of directivity, radiation pattern and polarization [90]. This approach has been used in previous work to model radiators in a similar environment [91].

It is assumed that the wireless link is sufficiently narrowband that the fields can be approximated as sinusoidal. Thus, phasor notation can be used to represent the field components and the associated propagation parameters can be modelled as frequency-independent. As such, the electric field vector in the far-field of an antenna, denoted by $\vec{E}$, can be expressed as [90]

$$\vec{E} = -j\frac{\eta I_{\text{in}}\vec{l}_{\text{e}}}{2\lambda r}\exp\left(-j\frac{2\pi r}{\lambda}\right), \tag{3.2}$$

where η in the wave impedance, I_{in} is the current through the input terminals of the antenna, $\vec{l}_{\text{e}}$ is the vector effective length, λ is the wavelength and r is the radial component of the point at which the field is being evaluated in spherical coordinates. It is convenient to note that I_{in} can be written as

$$I_{\text{in}} = \frac{V_{\text{in}}}{Z_{\text{in}}}, \tag{3.3}$$

where V_{in} is the voltage across input terminals of the antenna and Z_{in} is the antenna input impedance. It is assumed throughout the simulations that the antennas are lossless and resonant, making

$$Z_{\text{in}} = R_{\text{rad}}, \tag{3.4}$$

where R_{rad} is the radiation resistance [90]. Antenna vector effective length can be further expressed as

$$\vec{l}_{\text{e}} = 0\,\hat{r} + l_\theta\,\hat{\theta} + l_\phi\,\hat{\phi}, \tag{3.5}$$

where l_θ and l_ϕ are elevation and azimuth components of $\vec{l}_{\text{e}}$, respectively. The unit vectors in the r, θ and ϕ directions are denoted by $\hat{r}$, $\hat{\theta}$ and $\hat{\phi}$, respectively. Of course, the radial component of $\vec{l}_{\text{e}}$ is always zero for propagation in the transverse electromagnetic (TEM) mode. Thus, the far-field behaviour of the antenna is completely described by $\vec{l}_{\text{e}}$ and R_{rad}.

Vector effective length is also applicable upon signal reception. Consider an electric field incident upon an antenna from the far-field. The voltage across the open-circuited antenna terminals, V_{oc}, is given by [90]

$$V_{\text{oc}} = \vec{E} \bullet \vec{l}_{\text{e}}, \tag{3.6}$$

where $\bullet$ denotes the vector inner product operation. Assuming the output of the antenna is conjugate matched, the corresponding output voltage, V_{out}, is simply

$$V_{\text{out}} = \frac{V_{\text{oc}}}{2}. \tag{3.7}$$

3.1.2.1 Radiating Elements

The isotropic source, though purely theoretical, is a fundamental radiating element which is often used as a reference for quantifying the behaviour of practical antennas. For example, the gain of an antenna is typically expressed relative to that of an isotropic source. Due its impractical nature, it does not have readily applicable values for R_{rad} and $\vec{l}_{\text{e}}$; however, they can be derived theoretically. Consider two antennas in free space, separated by a distance of r_{12} which is much larger than the associated far-field distances. Assuming the antennas are lossless, conjugate matched and polarization-aligned, the power delivered to the load at the output of antenna 2, P_{out2}, due to radiated power from antenna 1, P_{in1}, can be expressed based on Friis' transmission equation as [90]

$$P_{\text{out2}} = P_{\text{in1}} \left(\frac{\lambda}{4\pi r_{12}} \right)^2 G_{01}\, G_{02}, \tag{3.8}$$

where G_{01} and G_{02} are the maximum gains associated with antennas 1 and 2, respectively. Based on the current assumptions, this can be re-written as

$$\frac{|V_{\text{out2}}|^2}{2R_{\text{rad2}}} = \frac{|V_{\text{in1}}|^2}{2R_{\text{rad1}}} \left(\frac{\lambda}{4\pi r_{12}} \right)^2 G_{01}\, G_{02}, \tag{3.9}$$

where V_{out2} is the voltage across the output terminals of antenna 2, R_{rad2} is the radiation resistance associated with antenna 2, V_{in1} is the voltage across the input terminals of antenna 1 and R_{rad1} is the radiation resistance associated with antenna 1. Using Equations 3.2–3.7:

$$|V_{\text{out2}}| = \frac{\eta\, |V_{\text{in1}}| \left| \vec{l}_{\text{e1}} \bullet \vec{l}_{\text{e2}} \right|}{4\, \lambda\, r_{12}\, R_{\text{rad1}}}, \tag{3.10}$$

where $\vec{l}_{\text{e1}}$ and $\vec{l}_{\text{e2}}$ are the vector effective lengths associated with antennas 1 and 2, respectively. Note that the propagation medium is also assumed to be lossless

throughout the simulations. Substituting this into Equation 3.9 and rearranging gives

$$\frac{\left|\vec{l}_{\mathrm{e}1} \bullet \vec{l}_{\mathrm{e}2}\right|}{R_{\mathrm{rad}2}} = \frac{\lambda^2}{\eta\,\pi}\sqrt{G_{01}\,G_{02}}. \tag{3.11}$$

If both antennas are isotropic sources, this reduces to

$$\frac{\left|\vec{l}_{\mathrm{e}}\right|^2}{R_{\mathrm{rad}}} = \frac{\lambda^2}{\eta\,\pi}, \tag{3.12}$$

since the gains are unity, regardless of the values of θ and ϕ. Finally, the radiation resistance and vector effective length of an isotropic source can be expressed as

$$R_{\mathrm{rad}} = \eta \tag{3.13}$$

and

$$\left|\vec{l}_{\mathrm{e}}\right| = \frac{\lambda}{\sqrt{\pi}}, \tag{3.14}$$

respectively. Since only the magnitude of the vector effective length has been obtained, the polarization behaviour of the antenna remains unspecified. For ease of comparison with half-wavelength dipoles, the isotropic sources are assumed to be θ-polarized, meaning $l_\theta = \left|\vec{l}_{\mathrm{e}}\right|$ and $l_\phi = 0$.

Of course, the application of more practical radiators must also be investigated. Half-wavelength dipoles are the most fundamental and well-understood radiating elements. The associated vector effective length can be derived based on readily available field results using Equation 3.2, while the radiation resistance is known to be approximately 73 Ω [90]. In addition, resonant loops are considered despite the fact that they do not exhibit omnidirectional radiation patterns because their properties provide an interesting contrast with those of the other elements. A resonant loop has a

circumference of approximately one wavelength, at which the radiation resistance is known to be approximately 135 Ω [90]. The complete field description has been published [92], from which the far-field results are used in conjunction with Equation 3.2 to derive the associated vector effective length. Table 3.1 summarizes the values of R_{rad}, l_θ and l_ϕ associated with each of the radiating elements under consideration. The zeroth-, first- and second-order Bessel functions of the first kind are denoted by J_0, J_1 and J_2, respectively.

Table 3.1: Radiating parameters of an isotropic source, a half-wavelength dipole and a resonant loop.

Parameter	Isotropic Source	Half-wavelength Dipole	Resonant Loop
R_{rad} (Ω)	377	73	135
l_θ (m)	$\frac{\lambda}{\sqrt{\pi}}$	$-\frac{\lambda \cos\left(\frac{\pi}{2}\cos(\theta)\right)}{\pi \sin(\theta)}$	$\frac{\lambda \cos(\theta)\sin(\phi)\, J_1(\sin(\theta))}{\sin(\theta)}$
l_ϕ (m)	0	0	$\frac{\lambda \cos(\phi)\left[J_0(\sin(\theta)) - J_2(\sin(\theta))\right]}{2}$

3.1.2.2 Phased Arrays

Table 3.1 provides sufficient information to accurately model the electromagnetic behaviour of the PD and single-element AP antennas. However, additional steps must be taken to effectively model the phased-array AP antennas. In general, the behaviour of an array consisting of identical elements can be described in terms of two quantities: the element factor and the array factor [90]. Table 3.1 can be used to evaluate the element factor, as it simply expresses the electromagnetic behaviour of a single array element positioned at the geometric centre of the array. Conversely, the array factor only accounts for the electromagnetic behaviour resulting from the geometry of the array and the excitation phase associated with each element.

For an N-element uniform linear array with an inter-element spacing of s_{e} and a progressive phase shift between elements of β, the array factor, denoted by F_{A}, is given by [93]

$$F_{\mathrm{A}} = \sum_{a=1}^{N} \sqrt{\frac{R_{\mathrm{rad}}}{N\left(R_{\mathrm{rad}} + \sum\limits_{\substack{b=1 \\ b\neq a}}^{N} R_{ba}\right)}} \exp\left(j(a-1)\left(\frac{2\pi}{\lambda} s_{\mathrm{e}} \cos(\theta) + \beta\right)\right), \tag{3.15}$$

where R_{ba} is the mutual resistance between the b-th and the a-th array element. The exponential term accounts for the fact that the elements have been independently phased and are radiating from different physical locations, while the terms under the square root ensure that the radiated power is constant regardless of the values of N, s_{e} and β. This allows for a fair comparison between results associated with the use of phased-array and single-element AP antennas. The transmit power is divided equally among the elements in the array, which explains the presence of N in the denominator. The summation over R_{ba} in the denominator accounts for mutual coupling between the array elements. In order to make use of Equation 3.2, $\vec{l}_{\mathrm{e}}$ must be replaced by the vector effective length of the array, denoted by $\vec{l}_{\mathrm{e,array}}$, which can be expressed as

$$\vec{l}_{\mathrm{e,array}} = F_{\mathrm{A}}\, \vec{l}_{\mathrm{e,element}}, \tag{3.16}$$

where $\vec{l}_{\mathrm{e,element}}$ is the elemental vector effective length.

For the case of isotropic elements, the mutual resistance, $R_{ba,\mathrm{isotropic}}$, is given by [93, 94]

$$R_{ba,\mathrm{isotropic}} = R_{\mathrm{rad}}\, \mathrm{sinc}\left(\frac{2d_{\mathrm{e}}}{\lambda}\right) \cos\left((b-a)\beta\right). \tag{3.17}$$

where $d_{\mathrm{e}} = (b-a)s_{\mathrm{e}}$. Mutual resistance is solely considered as it is assumed that each

element is conjugate matched.

While Equation 3.17 is relatively easy to obtain, the formulations are considerably more difficult for practical antennas. For example, consider the use of dipoles as array elements. Since the radiation pattern of the array should be omnidirectional in the azimuth plane, the case of parallel collinear dipoles is assumed. The resulting mutual resistance, $R_{ba,\text{dipole}}$, is given by [93]

$$\begin{aligned} R_{ba,\text{dipole}} = \Bigg(-15\cos\left(\frac{2\pi d_\text{e}}{\lambda}\right)\Bigg[-2\text{Ci}\left(\frac{4\pi d_\text{e}}{\lambda}\right) + \text{Ci}\left(\frac{4\pi(d_\text{e}-l)}{\lambda}\right) + \text{Ci}\left(\frac{4\pi(d_\text{e}+l)}{\lambda}\right) \\ - \ln\left(\frac{d_\text{e}^2 - l^2}{d_\text{e}^2}\right)\Bigg] + 15\sin\left(\frac{2\pi d_\text{e}}{\lambda}\right)\Bigg[2\text{Si}\left(\frac{4\pi d_\text{e}}{\lambda}\right) - \text{Si}\left(\frac{4\pi(d_\text{e}-l)}{\lambda}\right) \\ -\text{Si}\left(\frac{4\pi(d_\text{e}+l)}{\lambda}\right)\Bigg]\Bigg)\cos\left((b-a)\beta\right), \end{aligned} \tag{3.18}$$

where $\text{Ci}\left(\cdot\right)$ denotes the cosine integral, $\text{Si}\left(\cdot\right)$ denotes the sine integral and l is the length of the dipole. Despite the fundamental nature of this radiator, the analytic expression for $R_{ba,\text{dipole}}$ is elaborate.

For the case of resonant loop elements, a closed form expression for mutual resistance is not available. Instead, values for $R_{ba,\text{loop}}$ were computed manually under the following circumstances:

- the loops were vertically oriented;
- the loops were driven from the positive x-direction; and
- the inter-element spacing (s_e) was one half-wavelength.

Figure 3.4 illustrates such an array for the case of $N = 4$. The MATLAB® code found in Appendix A can only be used to accurately model phased-array AP antennas with resonant loop elements under the above conditions. The values of $R_{ba,\text{loop}}$ were obtained by first computing the radiated power, denoted by P_rad, from a single loop excited by $V_\text{in} = 1$ V. In general, this can be accomplished using the expression [90]

$$P_{\text{rad}} = \frac{1}{2\eta} \int_0^{2\pi} \int_0^{\pi} |\vec{E}|^2 \sin(\theta)\, d\theta\, d\phi. \tag{3.19}$$

The radiated power resulting from each pair of loops in the array was then computed for the case of $\beta = 0°$ and $R_{ba} = 0\ \Omega$. The difference between these powers and that obtained for a single loop can be attributed to changes in antenna input resistance. Subtracting the radiation resistance from the corresponding input resistances yields the values of $R_{ba,\text{loop}}$ for $\beta = 0°$. The dependence on β is restored by multiplying each result by $\cos\left((b-a)\beta\right)$ [93].

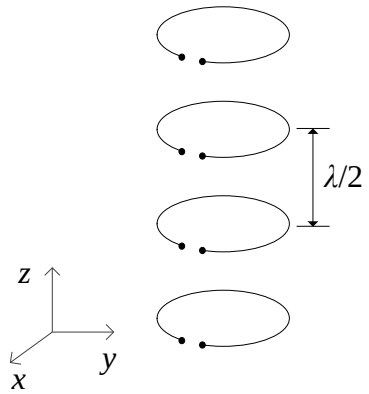

Figure 3.4: An illustration of a 4-element phased-array AP antenna comprised of resonant loop elements for simulation purposes.

3.1.3 Channel Model

The complex and time-varying nature of most wireless propagation environments suggests the application of stochastic channel models [55]. However, the static and relatively simplistic nature of the in-room environment presented in Section 3.1.1 lends itself to a deterministic channel model. The dimensions of the room are assumed to be very large relative to the wavelength of the radio signals under consideration. As a result, ray tracing is used in order to identify the propagation paths linking each pair of antennas [95, 96]. Ray tracing finds application in the development of com-

puter graphics and is based on the concepts of geometrical optics such as reflection and diffraction [97]. In the context of channel modelling, there are two distinct approaches: shoot-and-bounce ray tracing (SBR) and electromagnetic image theory [98]. SBR is very flexible to changes in the scattering environment, but is more complex and computationally intensive. Electromagnetic image theory is fast and intuitive, but is only practical for very simplistic environments [98]. Under the circumstances, ray tracing with electromagnetic image theory is the appropriate choice.

The walls, floor and ceiling are assumed to be smooth, linear, isotropic, homogeneous and non-magnetic electromagnetic boundaries. Each boundary is therefore characterized by a relative permittivity, ϵ_{r}. As a result, NLOS paths arise solely from specular reflections. Diffuse scattering is not considered as the resulting multipath components tend to be much weaker than those associated with specular reflections [98]. The spherical wave model is applied due to the relative proximity of the PD and the AP [99]. This is in contrast to the plane wave model, in which the average length associated with all of the rays linking a given PD antenna to each of the AP antennas would be used for free space path loss calculations. The plane wave model finds application in purely LOS MIMO channels where the transmitter and receiver are often separated by a very large distances. Conversely, the spherical wave model treats path loss and phase shift calculations equivalently: each ray is attributed its own length subject to the distance separating the corresponding PD and AP antennas.

3.1.3.1 Ray Tracing

The ray tracing algorithm will be described for a SISO system, as it is simply repeated a number of times for a MIMO system. Stepping back from electromagnetic details for the moment, a ray can be completely described by a series of points in space: a start point, a number of reflection points, if any, and an end point. Throughout

the simulations, it is assumed that the PD is transmitting and the AP is receiving. The start and end points of a given ray are therefore denoted by A_{PD} and A_{AP}, respectively.

The LOS ray is the simplest to model as it is completely described by A_{PD} and A_{AP}, which are already known. Modelling the NLOS rays is more computationally intensive as the coordinates of the boundary reflection points must be determined. All of the possible combinations of boundaries upon which the ray may reflect based on the total number of boundaries and the number of reflections under consideration must be identified; this is readily accomplished using the appropriate MATLAB® commands. The number of NLOS rays which must be evaluated increases rapidly with the maximum number of reflections which are to be evaluated. Table 3.2 presents the total number of NLOS rays when one to four reflections are considered. Since the execution of the ray tracing algorithm requires a significant portion of the total simulation time, selecting the lowest possible number of reflections without degrading the accuracy of the results is desirable. Depending on the relative locations of the PD and AP, some of the NLOS rays may not be valid. This can only be ascertained upon evaluation of the associated ray reflection points.

Table 3.2: The number of NLOS rays which must be evaluated by a ray tracing algorithm employing electromagnetic image theory based on the maximum number of reflections under consideration.

Max. Reflections	NLOS Rays
1	6
2	36
3	396
4	3636

The ray tracing algorithm is best described with an example. Consider the case depicted by Figure 3.5 in which the ray starts at A_{PD}, reflects off of Boundary 1, then Boundary 2 and ends at A_{AP}. Although Figure 3.5 illustrates a two-dimensional

situation for clarity, all of the quantities and calculations are three-dimensional. The geometry of the situation can be evaluated using image theory [100]. The final destination of the ray, A_{AP}, must be mirrored about each of the reflection boundaries in reverse order to give the first ray destination, which is denoted by A''_{AP} in this case. In general, a point A which has been mirrored about a boundary, denoted by A', can be expressed as

$$A' = A - 2\, d_{AB}\, \hat{n}_{\mathrm{B}}, \tag{3.20}$$

where $\hat{n}_{\mathrm{B}}$ is the unit normal vector associated with the boundary and d_{AB} is the distance from A to the boundary. This distance is given by

$$d_{AB} = A \bullet \hat{n}_{\mathrm{B}} + d_{\mathrm{B}}, \tag{3.21}$$

where d_{B} is the distance from the boundary to the origin.

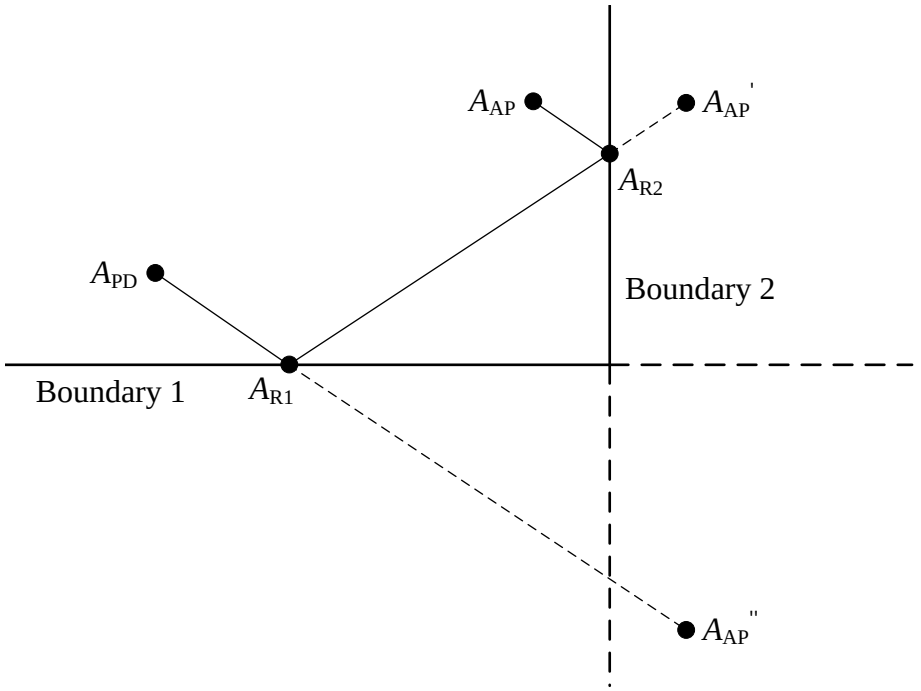

Figure 3.5: A two-reflection ray tracing example.

Once the coordinates of A''_{AP} are known, the first reflection point, A_{R1}, must be computed. This is accomplished by determining the directional unit vector associated with the first segment of the ray, denoted by $\hat{A}_{\mathrm{D1}}$, which can be expressed as [97]

$$\hat{A}_{\mathrm{D1}} = \frac{A''_{\mathrm{AP}} - A_{\mathrm{PD}}}{|A''_{\mathrm{AP}} - A_{\mathrm{PD}}|}. \tag{3.22}$$

Thus, an arbitrary point along the line associated with the first ray segment, A_1, is given by [97]

$$A_1 = A_{\mathrm{PD}} + \alpha\, \hat{A}_{\mathrm{D1}}, \tag{3.23}$$

where α is a number which indicates the position along the line relative to A_{PD}. The value of α associated with the point of reflection upon Boundary 1, denoted by α_{R1}, can be written as [97]

$$\alpha_{\mathrm{R1}} = -\frac{\hat{n}_{\mathrm{B1}} \bullet A_{\mathrm{PD}} + d_{\mathrm{B1}}}{\hat{n}_{\mathrm{B1}} \bullet \hat{A}_{\mathrm{D1}}}, \tag{3.24}$$

where $\hat{n}_{\mathrm{B1}}$ is the unit normal vector associated with Boundary 1 and d_{B1} is the distance from Boundary 1 to the origin. Equation 3.24 assumes that $\hat{n}_{\mathrm{B1}} \bullet \hat{A}_{\mathrm{D1}} \neq 0$; otherwise the ray segment is parallel to the boundary and the reflection will not occur. In this case, the ray is deemed invalid and the algorithm is terminated. If the ray is still valid, determining A_{R1} is simply a matter of evaluating Equation 3.23 using the value of α_{R1}. As long as A_{R1} is within the confines of the room, the complete ray segment remains valid.

The above procedure is repeated in order to evaluate A_{R2} by using A_{R1} and A'_{AP} as the start and end points of the second ray segment, respectively. In fact, it can be repeated an arbitrary number of times based on the number of reflections under consideration. Once all of the reflection points have been computed and the full ray is deemed valid, the complex channel gain and propagation delay can be computed

via electromagnetic calculations.

3.1.3.2 Electromagnetics

Based on A_{PD} and the first ray destination, the transmitted electric field can be computed using Equation 3.2. For the purposes of evaluating wave reflections or the incident field upon an AP antenna, it is convenient to first express the electric field in rectangular coordinates. This can readily be accomplished using a conversion matrix [90]:

$$\vec{E}_{\mathrm{rectangular}} = \begin{bmatrix} \sin(\theta)\cos(\phi) & \cos(\theta)\cos(\phi) & -\sin(\phi) \\ \sin(\theta)\sin(\phi) & \cos(\theta)\sin(\phi) & \cos(\phi) \\ \cos(\theta) & -\sin(\theta) & 0 \end{bmatrix} \vec{E}_{\mathrm{spherical}}. \tag{3.25}$$

In the case of a NLOS path, the electric field is subject to one or more reflections off of the floor, the ceiling or one of the walls. If the electromagnetic wave is normally incident upon the boundary, the reflection is relatively simple to evaluate. The wave reflection coefficient for this case, Γ_{normal}, is given by [100]

$$\Gamma_{\mathrm{normal}} = \frac{1-\sqrt{\epsilon_{\mathrm{r}}}}{1+\sqrt{\epsilon_{\mathrm{r}}}}. \tag{3.26}$$

The reflected electric field, $\vec{E}_{\mathrm{ref}}$, can be expressed in terms of the incident electric field, $\vec{E}_{\mathrm{inc}}$, as

$$\vec{E}_{\mathrm{ref}} = \Gamma_{\mathrm{normal}}\,\vec{E}_{\mathrm{inc}}. \tag{3.27}$$

Typically, the wave is obliquely incident upon the boundary. In this case, the first step is to identify the plane of incidence, which contains both the unit normal vector associated with the boundary and the unit vector associated with the direction

of wave incidence. The latter, denoted by $\hat{A}_{\text{inc}}$, is obtained similarly to $\hat{A}_{\text{D1}}$ based on the wave origin point and the point of reflection upon the boundary. The unit normal vector associated with the plane of the incidence, $\hat{n}_{\text{inc}}$, is therefore given by

$$\hat{n}_{\text{inc}} = \hat{A}_{\text{inc}} \times \hat{n}_{\text{B}}. \tag{3.28}$$

where $\times$ denotes the vector cross product operation. Figure 3.6 illustrates the plane of incidence for the wave reflection under consideration. The associated reflection coefficient depends on whether or not the incident electric field is parallel or perpendicular to the plane of incidence [100]. Consequently, oblique reflection also affects the polarization of the wave. The perpendicular electric field component, denoted by $\vec{E}_{\perp}$, can be expressed as

$$\vec{E}_{\perp} = (\hat{n}_{\text{inc}} \bullet \vec{E}_{\text{inc}})\, \hat{n}_{\text{inc}}. \tag{3.29}$$

The parallel field component, $\vec{E}_{\parallel}$, can then be determined:

$$\vec{E}_{\parallel} = \vec{E}_{\text{inc}} - \vec{E}_{\perp}. \tag{3.30}$$

The corresponding reflection coefficients are given by

$$\Gamma_{\perp} = \frac{\cos(\theta_{\text{inc}}) - \sqrt{\epsilon_r}\cos(\theta_{\text{tra}})}{\cos(\theta_{\text{inc}}) + \sqrt{\epsilon_r}\cos(\theta_{\text{tra}})} \tag{3.31}$$

and

$$\Gamma_{\parallel} = \frac{\cos(\theta_{\text{tra}}) - \sqrt{\epsilon_r}\cos(\theta_{\text{inc}})}{\cos(\theta_{\text{tra}}) + \sqrt{\epsilon_r}\cos(\theta_{\text{inc}})}, \tag{3.32}$$

where θ_{inc} is the angle of incidence upon the boundary and θ_{tra} is the angle of transmission into the boundary medium [100]. The value of θ_{tra} can be determined from θ_{inc} using Snell's law [100]:

$$\theta_{\text{tra}} = \arcsin\left(\frac{\sin(\theta_{\text{inc}})}{\sqrt{\epsilon_{\text{r}}}}\right). \tag{3.33}$$

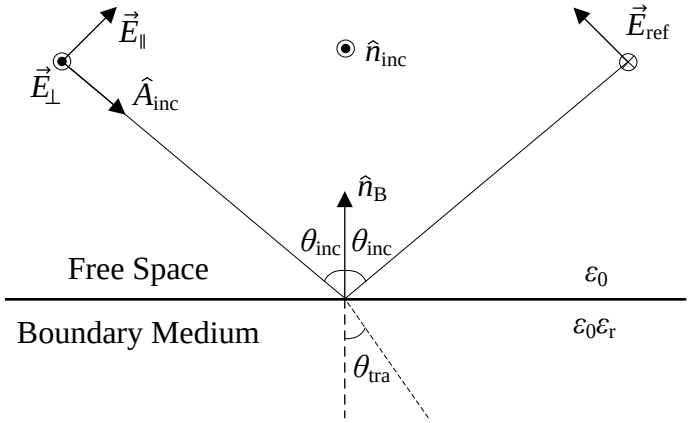

Figure 3.6: An illustration of the plane of incidence for an oblique reflection.

Upon reflection, the component of the electric field which is normal to the boundary is inverted. This is addressed by first expressing the field relative to the local coordinate system of the boundary. The wave reflection point acts as the origin of the boundary coordinate system, while the boundary itself occupies the associated xy-plane. This conversion is achieved using an Euler rotation matrix, for which the Euler angles ϕ_{E}, θ_{E} and ψ_{E} must be evaluated [101]. Let $\hat{o}_x$, $\hat{o}_y$ and $\hat{o}_z$ denote the unit vectors associated with the x-, y- and z-axes of the boundary coordinate system. Since θ_{E} is the angle between the z-axes of the global and boundary coordinate systems, it can be expressed as

$$\theta_{\text{E}} = \arccos(\hat{z} \bullet \hat{o}_z). \tag{3.34}$$

The corresponding rotation matrix, $\mathbf{R}_{\text{E},\theta}$, is given by [101]

$$\mathbf{R}_{\mathrm{E},\theta} = \begin{bmatrix} 1 & 0 & 0 \\ 0 & \cos(\theta_{\mathrm{E}}) & \sin(\theta_{\mathrm{E}}) \\ 0 & -\sin(\theta_{\mathrm{E}}) & \cos(\theta_{\mathrm{E}}) \end{bmatrix}, \tag{3.35}$$

In order to evaluate the remaining Euler angles, the unit vector associated with the line of intersection between the xy-planes of the two coordinate systems must be evaluated. This is known as the line of nodes and its unit vector, $\hat{v}_{\mathrm{n}}$, can be written as [101]

$$\hat{v}_{\mathrm{n}} = \frac{\hat{z} \times \hat{o}_z}{|\hat{z} \times \hat{o}_z|}. \tag{3.36}$$

The angle between the x-axis of the global coordinate system and the line of nodes is ϕ_{E} and is given by

$$\phi_{\mathrm{E}} = \arccos(\hat{x} \bullet \hat{v}_{\mathrm{n}}). \tag{3.37}$$

The corresponding rotation matrix, $\mathbf{R}_{\mathrm{E},\phi}$, is expressed as [101]

$$\mathbf{R}_{\mathrm{E},\phi} = \begin{bmatrix} \cos(\phi_{\mathrm{E}}) & \sin(\phi_{\mathrm{E}}) & 0 \\ -\sin(\phi_{\mathrm{E}}) & \cos(\phi_{\mathrm{E}}) & 0 \\ 0 & 0 & 1 \end{bmatrix}. \tag{3.38}$$

Finally, ψ_{E} is the angle between the line of nodes and the x-axis of the boundary coordinate system, given by

$$\psi_{\mathrm{E}} = \arccos(\hat{v}_{\mathrm{n}} \bullet \hat{o}_x) \tag{3.39}$$

and the corresponding rotation matrix, $\mathbf{R}_{\mathrm{E},\psi}$, can be written as [101]

$$\mathbf{R}_{\mathrm{E},\psi} = \begin{bmatrix} \cos(\psi_{\mathrm{E}}) & \sin(\psi_{\mathrm{E}}) & 0 \\ -\sin(\psi_{\mathrm{E}}) & \cos(\psi_{\mathrm{E}}) & 0 \\ 0 & 0 & 1 \end{bmatrix}. \tag{3.40}$$

The complete Euler rotation matrix, $\mathbf{R}_{\mathrm{E}}$, is therefore given by [101]

$$\mathbf{R}_{\mathrm{E}} = \mathbf{R}_{\mathrm{E},\psi}\, \mathbf{R}_{\mathrm{E},\theta}\, \mathbf{R}_{\mathrm{E},\phi}. \tag{3.41}$$

Expressing the electric field in terms of the boundary coordinate system is accomplished via multiplication with $\mathbf{R}_{\mathrm{E}}$. Conversely, multiplication by $\mathbf{R}_{\mathrm{E}}^{T}$ converts the field from the boundary coordinate system back to the global coordinate system.

Based on the above considerations, the reflected electric field, denoted by $\vec{E}_{\mathrm{ref}}$ can finally be expressed as

$$\vec{E}_{\mathrm{ref}} = \mathbf{R}_{\mathrm{E}}^{T} \left(\left(\mathbf{R}_{\mathrm{E}} \left(\Gamma_{\parallel}\, \vec{E}_{\parallel} + \Gamma_{\perp}\, \vec{E}_{\perp} \right) \right) \circ (\hat{o}_x + \hat{o}_y - \hat{o}_z) \right), \tag{3.42}$$

where $\circ$ denotes the Hadamard product.

Once all of the required reflections have been evaluated, the output voltage resulting from the electric field incident upon the appropriate AP antenna can be computed using Equations 3.6 and 3.7. This requires converting the electric field back into spherical coordinates, which is accomplished via multiplication with the transpose of the matrix in Equation 3.25 [90].

3.1.3.3 Communications

The remainder of the model is governed by communication theory. The impulse response due to multipath between the a-th PD antenna and the b-th AP antenna, denoted by $m_{ba}(t)$, can be expressed as

$$m_{ba}(t) = \sum_{i=0}^{L-1} g_{ba}(i)\,\delta(t - \tau_{ba}(i)), \tag{3.43}$$

where L is the number of multipath components, $\delta(\cdot)$ denotes the Dirac delta function and t is time. The gain associated with the the i-th multipath component linking the a-th PD antenna and the b-th AP antenna is denoted by $g_{ba}(i)$, while the corresponding propagation delay, $\tau_{ba}(i)$, is obtained by dividing the total length of the associated ray by the speed of light.

The use of $m_{ba}(t)$ as the channel impulse response implies operation in the passband, an infinite channel bandwidth and analog communication. The steps required in order to arrive at the bandlimited and discrete complex baseband channel impulse response are illustrated in Figure 3.7 via block diagram. After down-conversion, the baseband multipath impulse response, $m_{ba,\text{baseband}}(t)$, is given by

$$m_{ba,\text{baseband}}(t) = \sum_{i=0}^{L-1} g_{ba}(i)\,\exp(-j2\pi f_{\text{c}}\tau_{ba}(i))\,\delta(t - \tau_{ba}(i)). \tag{3.44}$$

where f_{c} is the passband centre frequency. This expression can be related to the results of the electromagnetic calculations by observing that

$$g_{ba}(i)\,\exp(-j2\pi f_{\text{c}}\tau_{ba}(i)) = \frac{V_{\text{out},b}(i)}{V_{\text{in},a}(i)}\sqrt{\frac{R_{\text{rad},a}}{R_{\text{rad},b}}}. \tag{3.45}$$

where $V_{\text{out},b}(i)$ is the output voltage from the b-th receive antenna due to the i-th multipath component, $V_{\text{in},a}(i)$ is the input voltage to the a-th transmit antenna associated with the i-th multipath component, $R_{\text{rad},a}$ is the radiation resistance of the a-th transmit antenna and $R_{\text{rad},b}$ is the radiation resistance of the b-th receive antenna. The continuous-time complex baseband channel impulse response, $h_{ba}(t)$, results from the convolution of $m_{ba,\text{baseband}}(t)$ with the impulse response of the baseband filter, $w_{\text{f}}(t)$. An ideal low-pass filter with a cut-off frequency of W is assumed. As a result,

$$w_{\mathrm{f}}(t) = 2W\mathrm{sinc}\,(2Wt) \tag{3.46}$$

and $h_{ba}(t)$ is given by

$$h_{ba}(t) = 2W \sum_{i=0}^{L-1} g_{ba}(i)\, \exp(-j2\pi f_{\mathrm{c}} \tau_{ba}(i))\, \mathrm{sinc}\,(2W(t - \tau_{ba}(i)))\,. \tag{3.47}$$

All that remains is to apply the sampling operation to $h_{ba}(t)$, giving $h_{ba,\mathrm{sampled}}(t)$:

$$\begin{aligned} h_{ba,\mathrm{sampled}}(t) = 2WT_{\mathrm{s}} \sum_{n=-\infty}^{n=+\infty} \sum_{i=0}^{L-1} & g_{ba}(i)\, \exp(-j2\pi f_{\mathrm{c}} \tau_{ba}(i)) \\ & \mathrm{sinc}\,(2W(nT_{\mathrm{s}} - \tau_{ba}(i)))\, \delta(t - nT_{\mathrm{s}}), \end{aligned} \tag{3.48}$$

where n is the time sample index and T_{s} is the sampling period. As a result of the ideal low-pass filter assumption, sampling can be performed at the Nyquist rate without incurring aliasing. Consequently,

$$T_{\mathrm{s}} = \frac{1}{2W}. \tag{3.49}$$

Furthermore, the complex baseband channel impulse response can be represented more compactly using discrete signal notation:

$$h_{ba}[n] = \sum_{i=0}^{L-1} g_{ba}(i)\, \exp(-j2\pi f_{\mathrm{c}} \tau_{ba}(i))\, \mathrm{sinc}\,(n - 2W\tau_{ba}(i)))\,. \tag{3.50}$$

Thus, each of the impulse responses—which include the effects of the antennas—associated with the MIMO channel were computed.

Applying a K-point discrete Fourier transform (DFT) to $h_{ba}[n]$ results in a transfer function given by $H_{ba}[k]$, where k is the frequency sample index. For a

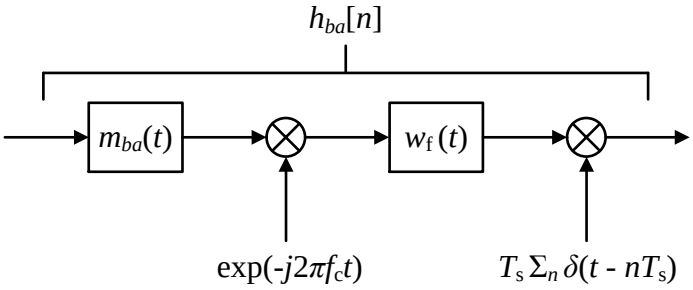

Figure 3.7: A block diagram of the complex baseband channel model.

MIMO system in which both the transmitter and receiver have M antennas, a total of M^2 transfer functions exist. At a particular value of k, the corresponding set of transfer function values can be organized into a CTM with M rows and M columns, given by $\mathbf{H}_k$. Once the CTMs have been obtained, channel modelling is complete and the appropriate performance metrics can be computed.

3.1.4 Performance Metrics

It is assumed that the transmitter has no knowledge of the channel, the transmit power is limited to P_{T}, the receiver has perfect knowledge of the channel and the received signal is corrupted by AWGN. Based on Equation 2.21 and the discrete signal notation introduced in Section 3.1.3.3, the MIMO capacity, C_{MIMO}, in bps/Hz can be expressed as [22]

$$C_{\mathrm{MIMO}} = \frac{1}{K} \sum_{k=0}^{K-1} \log_2 \det \left[\mathbf{I} + \frac{P_{\mathrm{T}}}{M P_{\mathrm{N}}} \mathbf{H}_k \mathbf{H}_k^H \right]. \tag{3.51}$$

The use of MIMO capacity as the sole performance metric can be problematic as it is difficult to distinguish between the effects of the received SNR and spatial multiplexing gains on C_{MIMO}. This issue is typically resolved through normalization of the CTMs and the selection of a fixed SISO-equivalent SNR such that only spatial multiplexing gains affect capacity [33]. However, the application of directional anten-

nas to the in-room scenario will most likely result in significant changes to both of these factors. Consequently, received SNR and relative MIMO gain [102] are used as additional performance metrics, allowing for the effects of each on the MIMO capacity to be observed.

In order to calculate the SNR associated with the MIMO system, the received power at each AP antenna must be determined. This is accomplished by addition of the contributions from each of the M PD antennas and averaging over k since a frequency-selective channel has been assumed. Therefore, the total received power at the b-th AP antenna, $P_{\mathrm{R}b}$, is given by

$$P_{\mathrm{R}b} = \frac{1}{K} \sum_{k=0}^{K-1} \sum_{a=1}^{M} |H_{ba}[k]|^2 \, \frac{P_{\mathrm{T}}}{M}. \tag{3.52}$$

The total received power, P_{R}, is readily obtained by averaging $P_{\mathrm{R}b}$ over b:

$$P_{\mathrm{R}} = \frac{1}{KM} \sum_{k=0}^{K-1} \sum_{b=1}^{M} \sum_{a=1}^{M} |H_{ba}[k]|^2 \, \frac{P_{\mathrm{T}}}{M}. \tag{3.53}$$

Note that the summation of $|H_{ba}[k]|^2$ over both b and a is the squared Frobenius norm of $\mathbf{H}_k$, written as $\|\mathbf{H}_k\|_{\mathrm{F}}^2$. The received SNR, ρ, is therefore given by [103]

$$\rho = \frac{P_{\mathrm{T}}}{KM^2 P_{\mathrm{N}}} \sum_{k=0}^{K-1} \|\mathbf{H}_k\|_{\mathrm{F}}^2. \tag{3.54}$$

Since SNR is conveniently expressed in dB, let ρ_{dB} denote $10 \log_{10} \rho$.

Relative MIMO gain is defined as the ratio of the MIMO capacity to that of the equivalent SISO system in which the PD and AP antennas are of the same type as those in the MIMO system and are each located at the centre of the respective MIMO UCAs. Denoted by g_C, the relative MIMO gain is simply given by [102]

$$g_C = \frac{C_{\mathrm{MIMO}}}{C_{\mathrm{SISO}}}, \tag{3.55}$$

where C_{SISO} is the SISO capacity, which can be calculated using Equation 3.51 for $M = 1$. It should be noted that g_C is not completely insensitive to variations in SNR; the SNRs associated with the MIMO and SISO systems may not be equal due to the different antenna placements.

3.2 Results

Most of the simulation results presented in the following subsections were generated for the case of $d_x = d_y = 8$ m and $d_z = 3$ m, as these represent room dimensions which would be typical for an office or academic environment. Results for other room geometries can be found in Section 3.2.2.1. The value of d_{PD} is assumed to be 1 m, as it roughly corresponds to the height of a PD being operated while the user is seated. In order to ensure that nothing occupies the near-field region of the AP antennas, d_{AP} and s_{AP} are given by $d_z - 2\lambda$ and 2λ, respectively [104]. In the interest of simplicity, the physical dimensions of the antennas are ignored; even if the phased-array AP antennas become quite large, d_{AP} and s_{AP} remain unchanged. The value of s_{e} affects the directivity and sidelobe level of the associated phased array. A value of $\lambda/2$ is used as it maximizes antenna directivity while maintaining the sidelobe level at approximately 10 dB below that of the main lobe. Since it is likely that a PD would be relatively compact, s_{PD} is $\lambda/2$. Furthermore, a distance of over 2λ is always maintained between the location of the PD and the walls.

The choice of M has a significant impact on simulation time as the number of individual channels which must be modelled is equal to M^2. As a result, a lower value of M is desirable; however, $M > 2$ is required for the AP and PD arrays to be UCAs. Therefore, the case of $M = 3$ is considered. While mutual coupling between phased-array elements is accounted for as detailed in Section 3.1.2.2, coupling between the PD and AP antennas is ignored. To avoid making assumptions about the radiation

patterns of the PD antennas, they are assumed to be isotropic sources.

As previously mentioned, the maximum number of reflections considered by the ray tracing algorithm also has a strong effect on simulation time. It has been shown that the contributions of paths with three or more reflections to the overall channel impulse response tend to be negligible due to additional propagation and reflection losses [2, 95]. As a result, only paths with up to two reflections are evaluated. For the walls, floor and ceiling, an ϵ_{r} of 4 is used as this is a typical dielectric constant for building materials at microwave frequencies [105–107]. At normal incidence, this gives a reflection loss of approximately 9.5 dB; therefore, the LOS components are on the order of 10 dB more powerful than the single-bounce NLOS components.

In accordance with the North American 2.4 GHz ISM band, the values of f_c and W are 2441.75 MHz and 41.75 MHz, respectively. For the DFTs, $K = 32$ is sufficient to properly model the frequency-selective behaviour of the channel. The ratio $P_{\mathrm{T}}/P_{\mathrm{N}}$ was chosen to be 80 dB, which ensures that the received SNR is high enough to avoid noise-limiting the achievable MIMO capacity. Based on W and an antenna temperature of approximately 300 K, the expected antenna noise would be approximately -98 dBm [104]. Transmit powers of over 0 dBm are typical for indoor wireless systems. Therefore, the choice of $P_{\mathrm{T}}/P_{\mathrm{N}} = 80$ dB is conservative, even if the losses and noise figure associated with the receiver are taken into consideration [108].

3.2.1 Single-element AP Antennas

The performance results obtained when single-element AP antennas are considered first as they serve as benchmarks for the phased-array cases. Figure 3.8 shows a surface plot of the MIMO capacity for $M = 3$, isotropic source AP antennas, $d_x = d_y = 8$ m and $d_z = 3$ m. The PD locations form a uniform grid within the available space and the communication performance is evaluated at each point. A 30 by 30 point grid was found to be sufficient in terms of generating reliable results

while maintaining reasonable computation times. Similar plots of ρ_{dB} and g_C are not included as they convey little additional information. From Figure 3.8 it is clear that C_{MIMO} generally increases as the location of the PD approaches the centre of the room, which is to be expected as the received SNR is also increasing. Exceptions to this trend occur in certain areas of the room largely due to reduced relative MIMO gain performance.

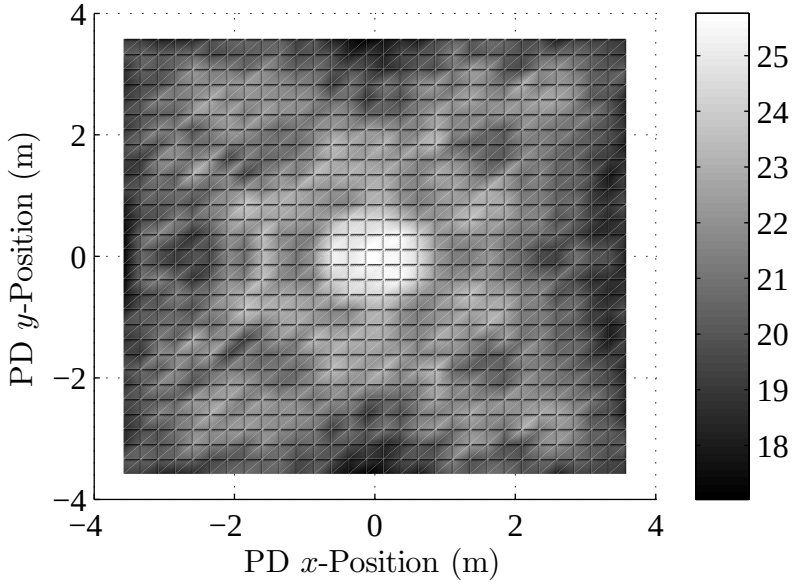

Figure 3.8: A surface plot of C_{MIMO} in bps/Hz for $M = 3$ isotropic source AP antennas in a room with $d_x = d_y = 8$ m and $d_z = 3$ m.

The MIMO capacity results associated with the use of half-wavelength dipoles and resonant loops as AP antennas are shown in Figures 3.9 and 3.10, respectively. Comparing these plots to Figure 3.8 highlights the influence of vector effective length on capacity. Figure 3.9 shows a generally higher degree of coverage near the walls and a capacity minimum directly below the AP, which is expected given the radiation pattern exhibited by a vertically oriented half-wavelength dipole. Conversely, Figure 3.10 shows that the centre of the room is favoured when resonant loop AP antennas are used, as is the y-axis relative to the x-axis in general. This is expected

given the associated radiation pattern and the fact that the loops are oriented such that they are fed from the x-direction. The use of loops also yields the largest range of channel capacities observed throughout the room. This is a result of the higher gain exhibited by resonant loops relative to the other elements coupled with the fact that loops favour the ϕ-polarization as opposed to the θ-polarization exhibited by the isotropic PD antennas, resulting in significant polarization losses in some areas of the room.

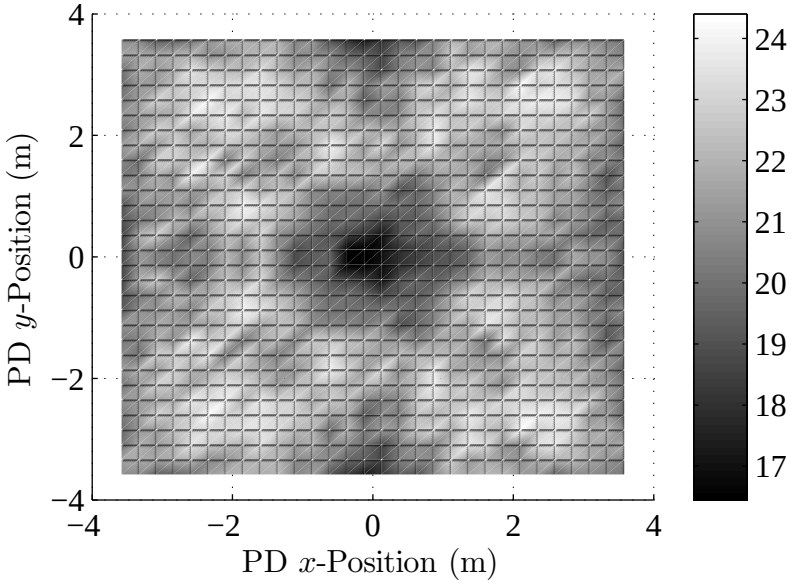

Figure 3.9: A surface plot of C_{MIMO} in bps/Hz for $M = 3$ half-wavelength dipole AP antennas in a room with $d_x = d_y = 8$ m and $d_z = 3$ m.

While surface plots fully present the in-room MIMO performance results, they do not easily allow for sets of results to be compared directly. For this reason, results are compared based on $\overline{C_{\text{MIMO}}}$, $\overline{\rho_{\text{dB}}}$ and $\overline{g_C}$, which represent the averages of C_{MIMO}, ρ_{dB} and g_C taken throughout the room, respectively. For the case of $M = 3$ single-element AP antennas and a room with $d_x = d_y = 8$ m and $d_z = 3$ m, these values are summarized in Table 3.3. Of particular interest is the fact that $\overline{C_{\text{MIMO}}}$ increases slightly with the use of half-wavelength dipoles in place of isotropic sources, which

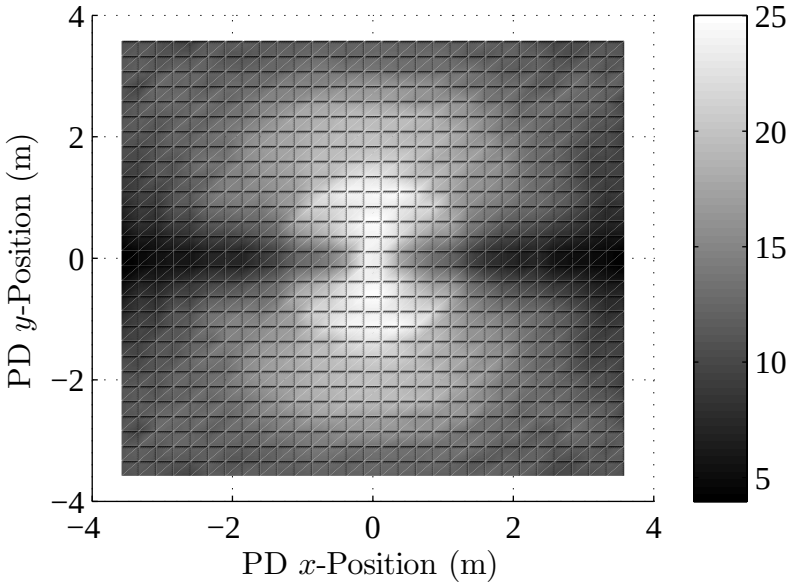

Figure 3.10: A surface plot of C_{MIMO} in bps/Hz for $M = 3$ resonant loop AP antennas in a room with $d_x = d_y = 8$ m and $d_z = 3$ m.

occurs in spite of a reduced $\overline{\rho_{\mathrm{dB}}}$ due to a corresponding increase in $\overline{g_C}$. The fact that the relative MIMO gain is highest on average for this case should not be surprising as vertical dipoles naturally favour NLOS over LOS components in this configuration. Conversely, it is lowest on average when loops are used as they favour LOS components in this configuration. The corresponding value of $\overline{\rho_{\mathrm{dB}}}$ is also lower due to the aforementioned losses arising due to polarization mismatches; as a result, $\overline{C_{\mathrm{MIMO}}}$ is lowest when loops are used.

Table 3.3: Room-averaged MIMO capacity, SNR and relative MIMO gain results for single-element AP antennas.

Element Type	$\overline{C_{\mathrm{MIMO}}}$ (bps/Hz)	$\overline{\rho_{\mathrm{dB}}}$ (dB)	$\overline{g_C}$ (-)
Isotropic Source	21.2	30.0	2.18
Half-wavelength Dipole	21.6	29.5	2.27
Resonant Loop	13.9	22.2	1.96

3.2.2 Phased-array AP Antennas

Consider the case of N-element phased-array AP antennas. Figure 3.11 shows plots of $\overline{C_{\mathrm{MIMO}}}$, $\overline{\rho_{\mathrm{dB}}}$ and $\overline{g_C}$ for a variety of N values with isotropic source elements as a function of the elevation angle associated with of the main lobes of the AP antenna radiation patterns, denoted by θ_0. Note that the single-element results have also been included for convenience. Only the range of $90^\circ \leq \theta_0 \leq 180^\circ$ has been considered, which corresponds to directing the main lobes from straight out toward the walls to straight down toward the floor; steering the main lobes upward results in significant reductions in received SNR values and, consequently, lower capacities.

Figure 3.11(a) shows that the maximum achievable value of $\overline{C_{\mathrm{MIMO}}}$ increases with N, suggesting an opportunity for MIMO capacity improvement through the application of θ-directional AP antennas to the in-room scenario. Since the relative improvements over the single-element case diminish with increasing N, results were not generated for $N > 8$. Based on Figure 3.11(b), improvements in $\overline{\rho_{\mathrm{dB}}}$ relative to the single-element case can also be achieved; however, it is interesting to note that the maximum result is actually associated with $N = 4$, suggesting that the SNR coverage might degrade if the AP antennas become overly directional. Finally, Figure 3.11(c) shows improvements in the maximum achievable $\overline{g_C}$ over the range of $90^\circ \leq \theta_0 \leq 180^\circ$, which increases along with N in a similar manner as $\overline{C_{\mathrm{MIMO}}}$.

Unfortunately, these benefits do not all occur for the same main lobe directions. Based on the geometry of the situation, the value of θ_0 should fall between approximately 90° and 114° to emphasize single-bounce wall-reflected NLOS components. In the case of isotropic elements, β is related to θ_0 by [90]

$$\beta = -\frac{2\pi s_{\mathrm{e}}}{\lambda}\cos(\theta_0). \tag{3.56}$$

As a result, the corresponding phasing angle range is $0^\circ \leq \beta \leq 72^\circ$. The $\overline{\rho_{\mathrm{dB}}}$ results

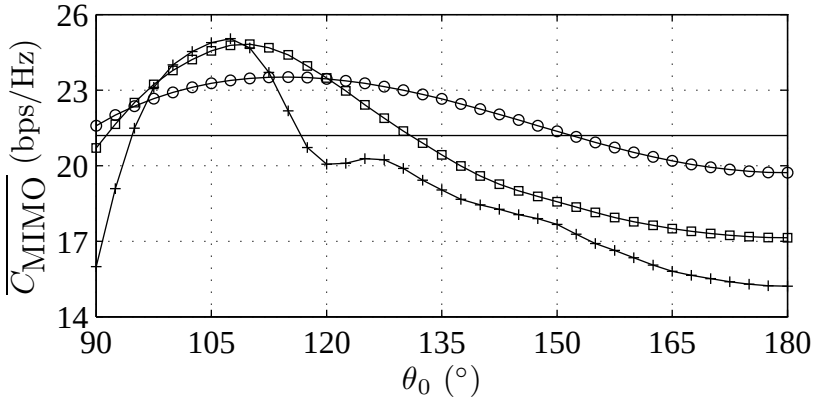

(a) $\overline{C_{\mathrm{MIMO}}}$.

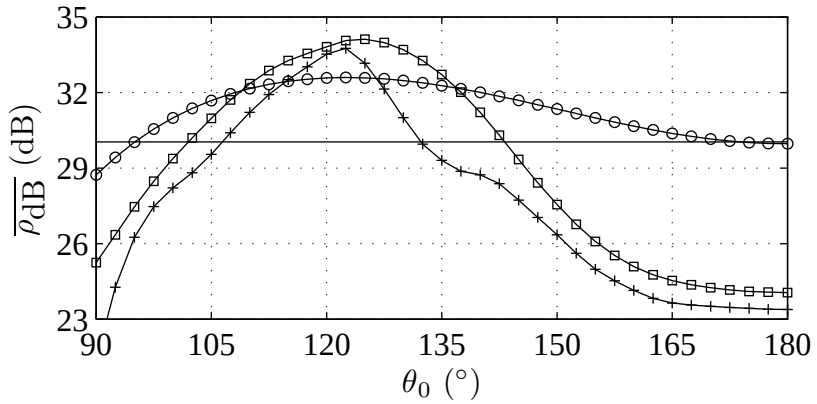

(b) $\overline{\rho_{\mathrm{dB}}}$.

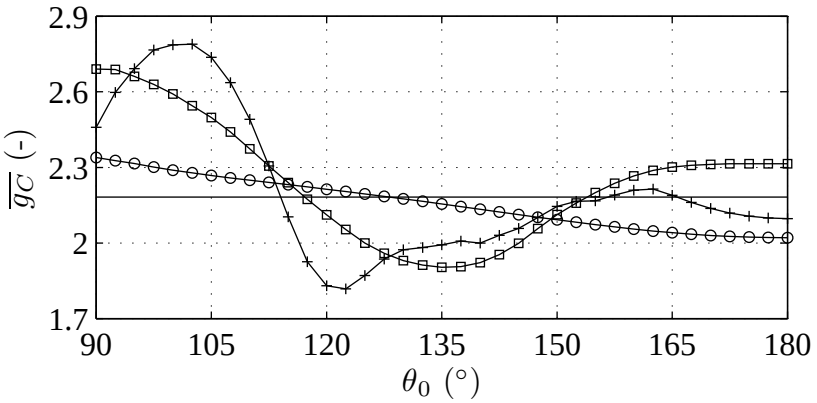

(c) $\overline{g_C}$.

Figure 3.11: Room-averaged performance metrics for phased-array AP antennas with isotropic elements as functions of θ_0. Solid line: single element, $\circ$: $N = 2$, $\square$: $N = 4$ and $+$: $N = 8$.

seem largely insensitive to these details, with maxima occurring between $\theta_0 = 120°$ and $\theta_0 = 125°$. This is consistent with aiming the main lobes of the AP antenna radiation patterns down toward the PD locations near the walls, thereby directly emphasizing LOS components over the largest possible surface area in the room. On the other hand, the maximizing value of θ_0 for $\overline{g_C}$ increases toward the centre of the expected θ_0 range as the AP antennas become more directional, reaching 103° for $N = 8$. This behaviour is consistent with directing the main lobes such that LOS components are not emphasized. For $N = 2$, the maximizing θ_0 associated with $\overline{g_C}$ is actually less than 90°, effectively directing the main lobes upward to avoid the LOS components. As the directivities of the AP antennas increase, it becomes possible to emphasize the wall-reflected NLOS components without also creating dominant LOS components. The maximizing value of θ_0 associated with $\overline{C_{\text{MIMO}}}$ appears to strike a balance between the competing results associated with $\overline{\rho_{\text{dB}}}$ and $\overline{g_C}$. For $N = 2$ the behaviour of the associated $\overline{C_{\text{MIMO}}}$ curve more closely resembles that of $\overline{\rho_{\text{dB}}}$ based on both similarities in the shapes of the curves and the fact that the maximizing θ_0 is relatively high at 115°. The opposite is true for $N = 8$, where the shape of $\overline{C_{\text{MIMO}}}$ resembles that of $\overline{g_C}$ and the maximum occurs at $\theta_0 = 108°$.

The results obtained for half-wavelength dipole and resonant loop elements are shown in Figures 3.12 and 3.13, respectively. Due to the nature of the element factor associated with the half-wavelength dipole, it is not possible to direct the main lobes down toward the floor. Consequently, the dipole results are only plotted up to θ_0 values of 120°, 140° and 150° for $N = 2$, 4 and 8, respectively. Qualitatively, the dipole and loop results are quite similar to those obtained with isotropic sources.

The primary objective associated with improving the quality of a communication link is to increase the channel capacity as it dictates the highest level of performance which can be achieved by the system. For MIMO communication, a secondary objective would be to increase the relative MIMO gain as it represents

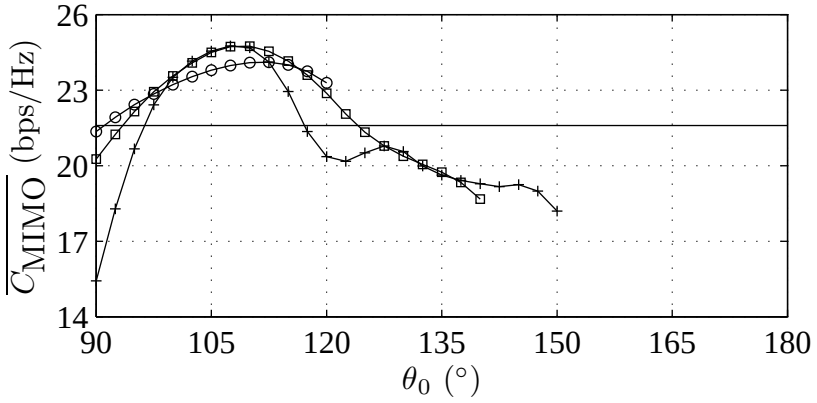

(a) $\overline{C_{\mathrm{MIMO}}}$.

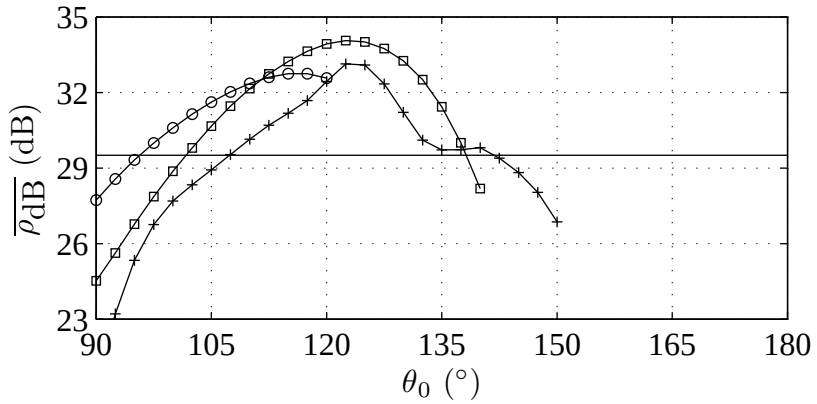

(b) $\overline{\rho_{\mathrm{dB}}}$.

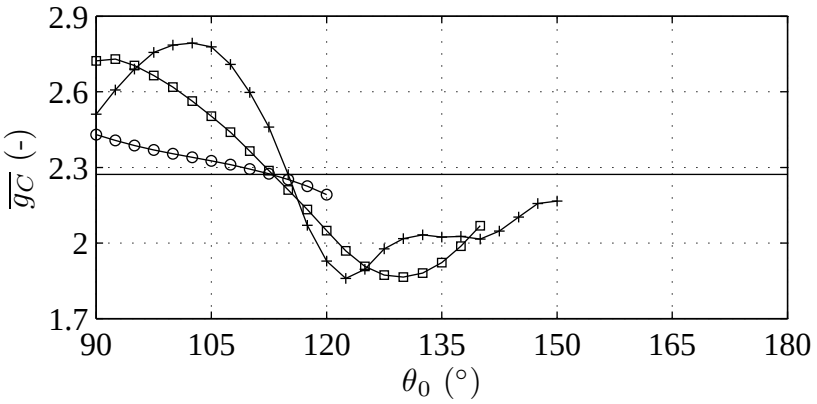

(c) $\overline{g_C}$.

Figure 3.12: Room-averaged performance metrics for phased-array AP antennas with half-wavelength dipole elements as functions of θ_0. Solid line: single element, ∘: $N = 2$, □: $N = 4$ and +: $N = 8$.

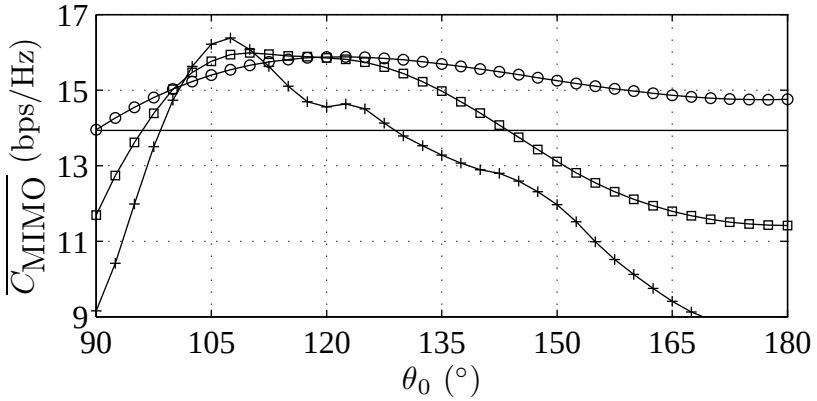

(a) $\overline{C_{\mathrm{MIMO}}}$.

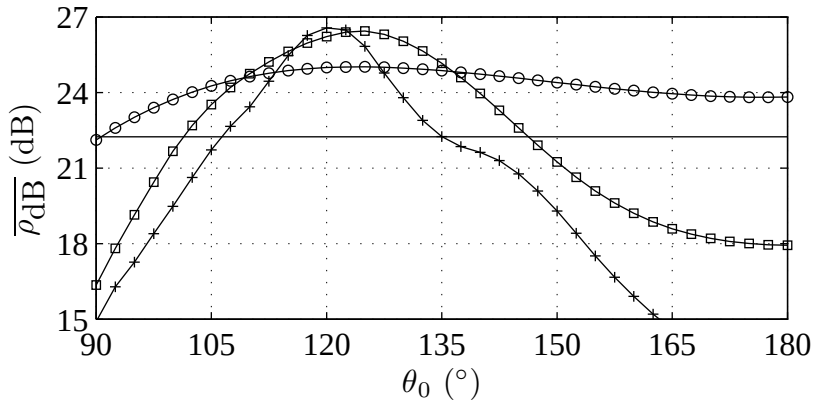

(b) $\overline{\rho_{\mathrm{dB}}}$.

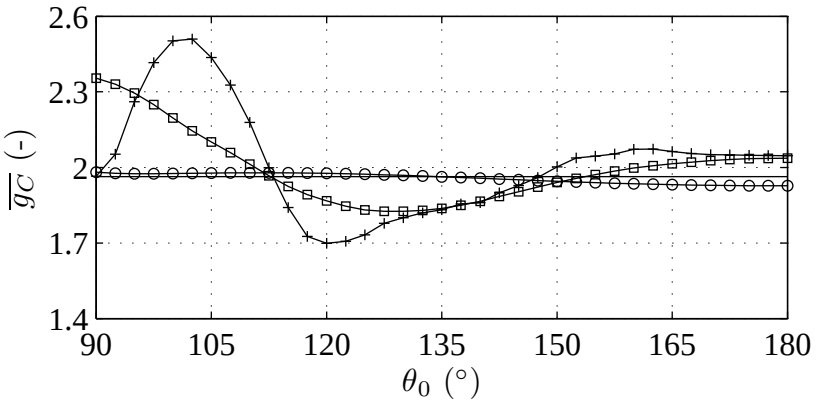

(c) $\overline{g_C}$.

Figure 3.13: Room-averaged performance metrics for phased-array AP antennas with resonant loop elements as functions of θ_0. Solid line: single element, $\circ$: $N = 2$, $\square$: $N = 4$ and $+$: $N = 8$.

the level of improvement associated with employing multiple antennas. Table 3.4 summarizes the MIMO performance results associated with the use of phased-array AP antennas. The θ_0 which maximizes $\overline{C_{\mathrm{MIMO}}}$ is identified for each antenna configuration and the corresponding values of both $\overline{C_{\mathrm{MIMO}}}$ and $\overline{g_C}$ are included. For each performance metric, the improvement relative to the single-element case, Δ_{SE}, is also shown as a percentage.

Table 3.4: The maximum $\overline{C_{\mathrm{MIMO}}}$ results along with the corresponding θ_0 values and the $\overline{g_C}$ results at those values for each phased-array AP antenna configuration under consideration.

Element Type	N	$\overline{C_{\mathrm{MIMO}}}$			$\overline{g_C}$	
		Max. (bps/Hz)	θ_0 (°)	Δ_{SE} (%)	At θ_0 (-)	Δ_{SE} (%)
Isotropic Source	2	23.5	115	+10.8	2.23	+2.29
	4	24.8	110	+17.0	2.37	+8.72
	8	25.0	108	+17.9	2.64	+21.1
Half-wavelength Dipole	2	24.1	113	+11.6	2.27	+0.00
	4	24.7	110	+14.4	2.37	+4.41
	8	24.8	108	+14.8	2.71	+19.4
Resonant Loop	2	15.9	123	+14.4	1.98	+1.02
	4	16.0	110	+15.1	2.01	+2.55
	8	16.4	108	+18.0	2.33	+18.9

The $\overline{C_{\mathrm{MIMO}}}$ results shown in Table 3.4 indicate that improvements of approximately 10–18 % can be achieved through the use of θ-directional AP antennas. The use of half-wavelength dipole elements yields the lowest overall improvement, which might be expected given that they exhibited the best performance in the single-element case. As previously mentioned, there tends to be relatively little change in $\overline{C_{\mathrm{MIMO}}}$ when N is increased from 4 to 8. While the θ_0 values are distinct among the different element types for $N = 2$, they tend to align as the antennas become more directional.

When the AP antennas are phased such that θ_0 approaches the value which maximizes $\overline{C_{\mathrm{MIMO}}}$, the degree of improvement in $\overline{g_C}$ strongly depends upon N. When $N = 2$, the improvements relative to the single-element case are negligible. The improvements remain quite low for the case of $N = 4$; however, for $N = 8$ they are far more significant, ranging between approximately 18–22 %. This behaviour is consistent with the main lobe becoming sufficiently narrow that the wall-reflected NLOS components can be solely emphasized.

Since $N = 8$ yields the most significant simultaneous improvement of $\overline{C_{\mathrm{MIMO}}}$ and $\overline{g_C}$, the remainder of the results will be evaluated for this case. Of course, achieving such high directivities would necessitate the construction of AP antennas which are electrically quite large. This suggests that the use of directional antennas to improve in-room MIMO performance might be best-suited for a system operating at a relatively high centre frequency so that the AP is not too physically large.

Figure 3.14 shows a surface plot of MIMO capacity for the case of $N = 8$, isotropic source elements and the $\overline{C_{\mathrm{MIMO}}}$-maximizing condition of $\theta_0 = 108°$. In comparison with the single-element results presented in Figure 3.8, the coverage provided by the phased-array AP antennas for this value of θ_0 tends to be more uniform. The range of capacity values observed throughout the room has shifted up from approximately 18–25 bps/Hz for the single-element case to approximately 19–26 bps/Hz; the spread of observed capacity values is largely unaffected.

Surface plots of C_{MIMO} associated with the use of phased-array AP antennas consisting of $N = 8$ half-wavelength dipole and resonant loop elements for $\theta_0 = 108°$ are shown in Figures 3.15 and 3.16, respectively. The MIMO capacity coverage resulting from the use of half-wavelength dipole phased-array elements is very similar to that of the single-element case; Figure 3.15 strongly resembles Figure 3.9 with the exception of an overall increase in capacity. In the case of resonant loop elements, Figure 3.16 shows far more uniform capacity coverage than was observed for the single-

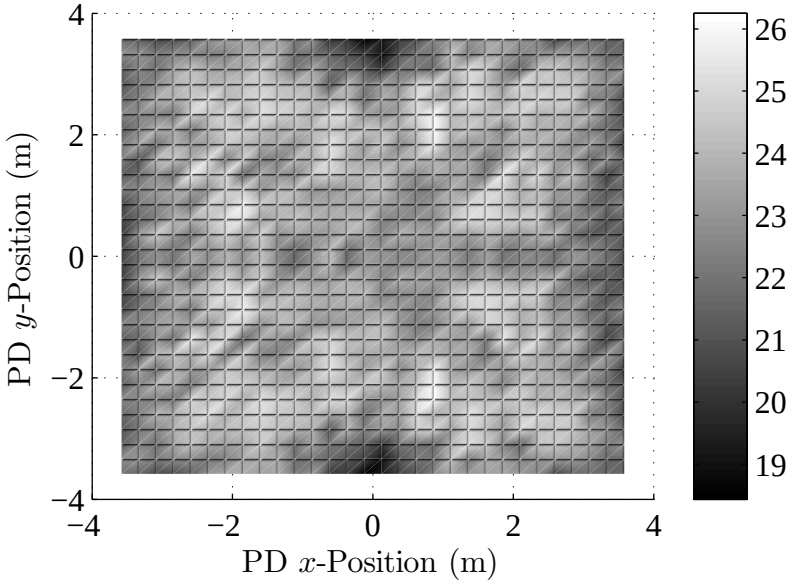

Figure 3.14: A surface plot of C_{MIMO} in bps/Hz for $M = 3$ phased-array AP antennas consisting of $N = 8$ isotropic source elements with $\theta_0 = 105°$ in a $d_x = d_y = 8$ m and $d_z = 3$ m room.

element case shown in Figure 3.10. Overall, comparing Figures 3.15 and 3.16 with Figure 3.14 reinforces the notion that the potential improvements associated with the use of elevation-directional AP antennas which emphasize wall-reflected NLOS components can be achieved regardless of minor changes in the terminal properties of the AP antennas.

3.2.2.1 Influence of Room Geometry

To this point, the results have been specific to the case of $d_x = d_y = 8$ m and $d_z = 3$ m. The concept of employing θ-directional AP antennas to improve in-room MIMO capacity should naturally apply to a variety of rooms. In order to investigate this, three distinct room geometries are considered: a small room with a high ceiling, a large room with a low ceiling and a room in which $d_x \neq d_y$. AP antennas consisting of 8-element phased arrays with isotropic elements are considered. Table 3.5 summarizes

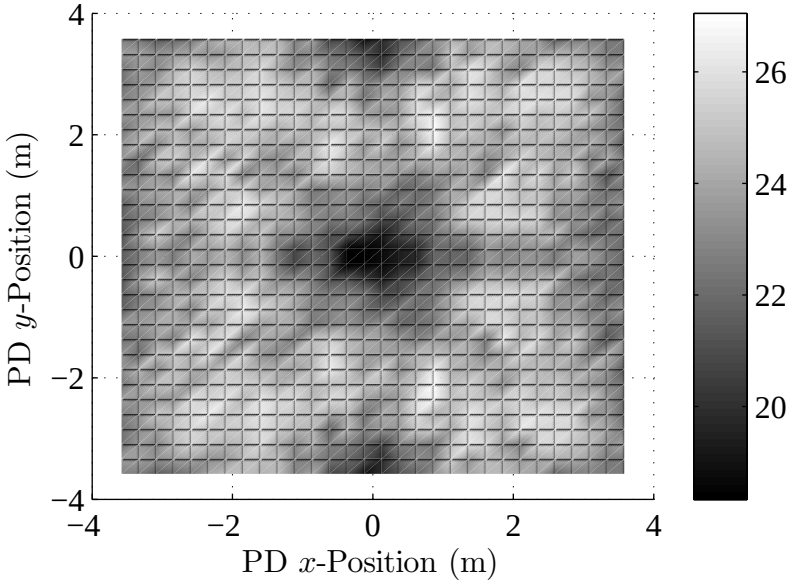

Figure 3.15: A surface plot of C_{MIMO} in bps/Hz for $M = 3$ phased-array AP antennas consisting of $N = 8$ half-wavelength dipole elements with $\theta_0 = 108°$ in a $d_x = d_y = 8$ m and $d_z = 3$ m room.

the results associated with each room geometry under consideration. The expected range of θ_0 values which would emphasize wall-reflected NLOS components is shown in addition to the $\overline{C_{\mathrm{MIMO}}}$-maximizing θ_0; in the case of $d_x = 6$ m, $d_y = 10$ m and $d_z = 3$ m, this range is obtained by averaging the x and y dimensions of the room. The results for $d_x = d_y = 8$ m and $d_z = 3$ m have been included for convenience.

In each case, the $\overline{C_{\mathrm{MIMO}}}$-maximizing value of θ_0 falls within the expected range given the geometry of the environment. It is found that the maximum $\overline{C_{\mathrm{MIMO}}}$ results tend be lower for larger rooms, which is expected as the relative multipath richness decreases with increasing room dimensions. However, the associated improvement over the single-element case increases for larger rooms because the θ_0 values which maximize $\overline{\rho_{\mathrm{dB}}}$ and $\overline{g_C}$ become closer together. Adjusting the room aspect ratio is found to have only a minor effect on the $\overline{C_{\mathrm{MIMO}}}$ results.

As the x and y dimensions of the room grow larger the LOS components

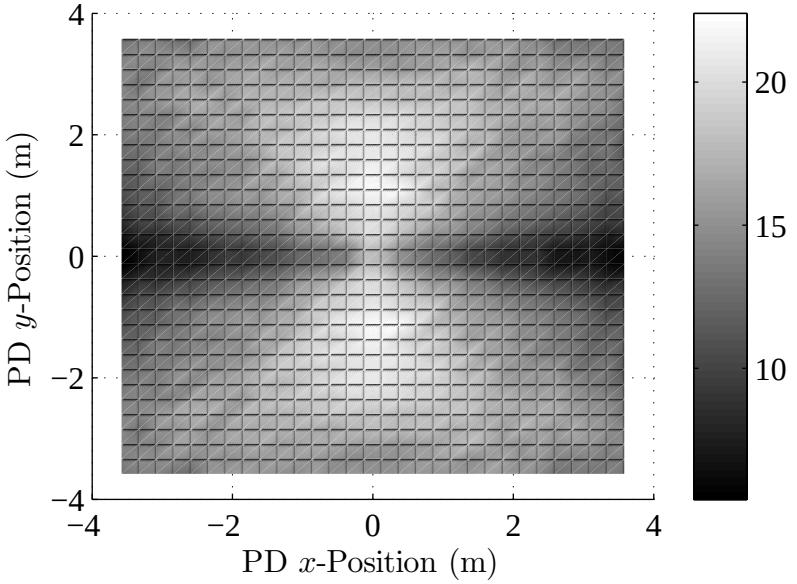

Figure 3.16: A surface plot of C_{MIMO} in bps/Hz for $M = 3$ phased-array AP antennas consisting of $N = 8$ resonant loop elements with $\theta_0 = 108°$ in a $d_x = d_y = 8$ m and $d_z = 3$ m room.

become increasingly dominant and, as a result, the corresponding values of $\overline{g_C}$ tend to decrease. However, the associated improvements relative to the single-element case are dictated by how well the wall-reflected NLOS components can be emphasized while avoiding the LOS components and, therefore, do not follow this trend. In addition, the improvement in $\overline{g_C}$ lowers when $d_x \neq d_y$ because it is more difficult to emphasize the wall-reflected NLOS components equally.

Of course, in a real room the presence of additional scatterers will impact the behaviour of $\overline{C_{\mathrm{MIMO}}}$ as a function of θ_0. Based on the results presented in Table 3.5, it is suggested that the MIMO performance can be improved in general by directing the main lobes of the AP antenna radiation patterns toward the middles of the walls at heights which correspond to the average of d_{PD} and d_{AP}. For the room geometries considered, this results in θ_0 values of 121°, 102°, 103° and 96° respectively, which agree quite well with the θ_0 results associated with $\overline{C_{\mathrm{MIMO}}}$.

Table 3.5: The maximum $\overline{C_{\text{MIMO}}}$ results along with the corresponding θ_0 values and the $\overline{g_C}$ results at those values for a variety of room geometries. The use of 8-element phased-array AP antennas with isotropic source elements is assumed. Based on the room geometries, the expected θ_0 range is also included.

d_x, d_y, d_z	Expected	$\overline{C_{\text{MIMO}}}$			$\overline{g_C}$	
(m)	θ_0 (°)	Max. (bps/Hz)	θ_0 (°)	Δ_{SE} (%)	At θ_0 (-)	Δ_{SE} (%)
$4, 4, 3.7$	90–141	26.9	124	+12.1	2.77	+16.4
$8, 8, 3$	90–114	25.0	108	+17.9	2.64	+21.1
$6, 10, 3$	90–114	25.2	108	+17.2	2.62	+18.0
$12, 12, 2.5$	90–102	24.5	100	+25.6	2.40	+7.14

3.3 Summary

Through simulation, it has been found that replacing the radiating elements comprising the AP antennas with N-element vertically oriented linear-phased-arrays could increase the in-room MIMO capacity, SNR and relative MIMO gain performance, depending on N and θ_0. Improvements in the received SNR are best achieved by simply directing the main lobes of the AP antenna radiation patterns toward the PD locations near the walls, thereby emphasizing LOS components over the largest possible area of the room. Conversely, the relative MIMO gain benefits from directing the main lobes such that LOS components are largely avoided, thus increasing multipath richness and reducing spatial correlation. Improvements in MIMO capacity are generally achieved for main lobe directions falling between those which maximize the room-averaged SNR and relative MIMO gain. The simulated results show that directing the main lobes of the AP antenna radiation patterns such that wall-reflected NLOS components are emphasized can improve in-room MIMO communication performance. Since the results were qualitatively similar for isotropic source, half-wavelength dipole and resonant loop elements, it can be concluded that the achievable performance improvements are robust to minor changes in the terminal properties of the AP antennas. It has also been found that the capacity improvements

are more significant for larger rooms in which LOS components are more dominant. However, the improvement in relative MIMO gain performance has a more complex relationship with the room dimensions as it is dictated by the degree to which the wall-reflected NLOS components can be emphasized while avoiding the LOS components.

Chapter 4

Improving In-room MIMO Capacity Using Elevation-directional Access Point Antennas: Measurements

The results of Chapter 3 suggest that the use of θ-directional AP antennas which emphasize wall-reflected NLOS components can improve MIMO performance in an in-room environment. However, they were obtained solely through simulation and must be verified experimentally. To accomplish this, a 2.4 GHz MIMO channel measurement campaign was carried out in an unoccupied classroom on the UNB Fredericton campus. The channel measurements were performed using an Agilent N5242A performance network analyzer (PNA) capable of acquiring S-parameter data on four distinct ports. This motivated performing MIMO channel measurements for $M = 2$, which differs from the simulations where $M = 3$ was considered. Ultimately, the same concepts can be explored regardless of the number of MIMO antennas.

4.1 Antennas

The design choices associated with the fabrication of the antennas are important because they impact the end results as evidenced by Table 3.4. Although the concept of employing θ-directional AP antennas to the in-room scenario applies most directly to the case of isotropic sources, such elements are impractical and cannot be readily approximated for measurement purposes. The performance improvements associated with the use of phased-arrays over the single-element case are most significant when resonant loop elements are used. However, the added complexity associated with constructing custom phased-arrays that conform to the geometry shown in Figure 3.4 coupled with the fact that the elements are not omnidirectional in azimuth made resonant loops an undesirable choice. Consequently, half-wavelength dipole elements were chosen for the measurements.

The results of Table 3.4 clearly demonstrate that the most significant improvements to both $\overline{C_{\mathrm{MIMO}}}$ and $\overline{g_C}$ at the same θ_0 occur for $N = 8$. The resulting antenna would be approximately 0.5 m long upon fabrication, which would be difficult to work with. Since the results of Table 3.4 also indicate that increasing N from 4 to 8 elements has only a minor impact on $\overline{C_{\mathrm{MIMO}}}$ when dipoles are used, 4-element phased-arrays of half-wavelength dipole elements were fabricated. As a result, the predicted improvements in $\overline{C_{\mathrm{MIMO}}}$ and $\overline{g_C}$ over the single-element case are only on the order of 12 % and 3 %, respectively. While the purpose of the measurements is to confirm that in-room MIMO performance can be improved using phased-array AP antennas, it is perhaps less important for the demonstrated improvements to be significantly large, but rather that they confirm the predicted behaviour of the metrics as a function of θ_0. If this is the case, simulation can be used to reliably determine if phased-array AP antennas would be effective for a particular room.

4.1.1 PD and Single-element AP Antennas

Due to the popularity of the half-wavelength dipole as a radiating element, generating a design for the PD and single-element AP antennas was unnecessary. A previously published design for a printed half-wavelength dipole with an integrated balun was selected for fabrication on flame resistant-4 (FR-4) board [109]. The presence of a balun is essential as the antennas will undoubtedly be driven by unbalanced coaxial cables throughout the measurements.

The printed dipole was modelled in Computer Simulation Technology (CST) Microwave Studio® to verify the findings of the corresponding paper [109] prior to fabrication and to generate a set of results with which the subsequent measurements could be compared. A printed circuit board (PCB) layout was created using the Agilent Advanced Design System (ADS) software package. The layout was exported in Gerber format for interpretation by a PCB router available at UNB and the boards were fabricated. Photographs of one of the completed dipoles are shown in Figure 4.1. An edge-mount subminiature version A (SMA) connector acts as the input while a short length of solid-core wire soldered to both sides of the hole—or via—drilled during the routing phase completes the feed network. Note that the design of the feed network is consistent with a quarter-wavelength balun [90]; therefore, the dipole conductors are driven by a balanced signal as desired.

The PNA was calibrated and measurements were carried out inside the UNB anechoic test chamber (ATC) to characterize the performance of a representative sample of the set of fabricated dipoles. Figure 4.2 presents measured and simulated input voltage standing wave ratio (VSWR) results from 2–3 GHz. The primary source of error between the measured and simulated results is the fact that the electromagnetic properties of the FR-4 dielectric are not generally controlled; the simulation is only based on the typical values of 4.3 and 0.025 for the relative permittivity and loss tangent, respectively. A VSWR of less than 2:1 is typically considered accept-

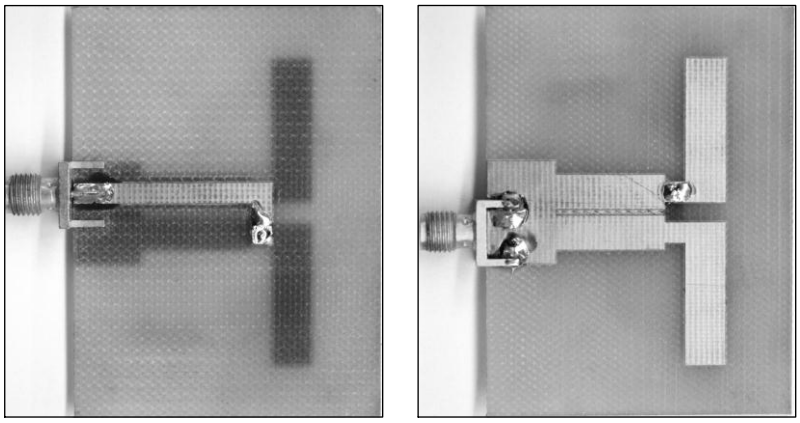

(a) Top layer photograph. (b) Bottom layer photograph.

Figure 4.1: Photographs of a printed dipole with an integrated balun fabricated for the PD and single-element AP antennas.

able in terms of input matching performance [104]. The measured results indicate that the fabricated dipole meets this specification over the desired frequency range of 2400–2483.5 MHz.

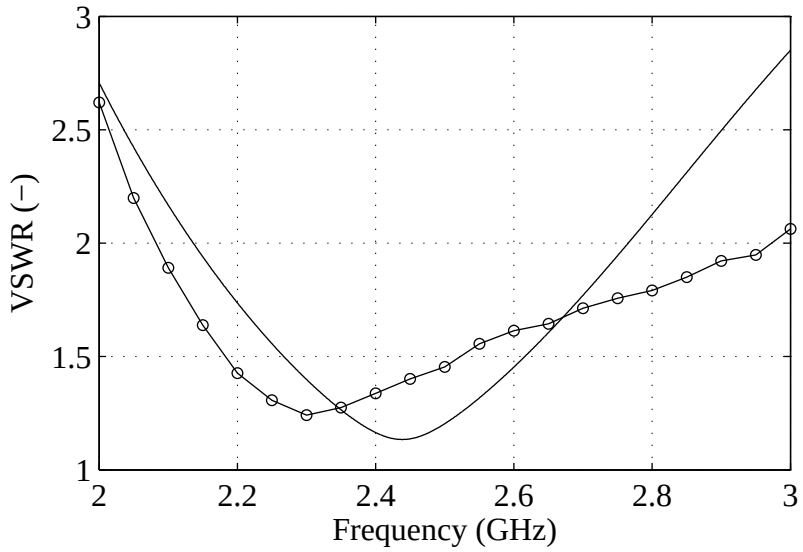

Figure 4.2: Measured and simulated input VSWR curves for one of the printed dipoles. Solid: simulated and ∘: measured.

Measured and simulated principal elevation-plane radiation patterns for the

printed dipole at 2.4 GHz are shown in Figure 4.3. The measured results agree well with those obtained through simulation. In addition to the aforementioned uncontrolled nature of the electromagnetic properties associated with the FR-4 dielectric, the presence of the SMA connector, feed cable and mounting apparatus are expected to impact the measured radiation patterns.

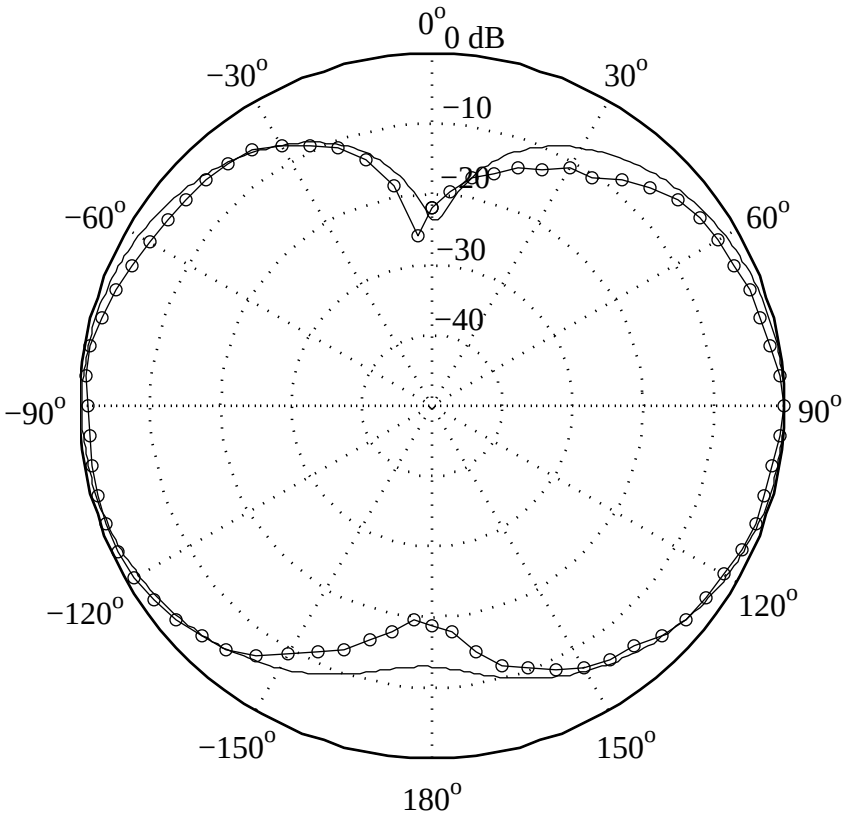

Figure 4.3: Measured and simulated elevation-plane ($\phi = 90°$) radiation patterns for one of the printed dipoles at 2.4 GHz. Solid: simulated and ∘: measured.

Figure 4.4 shows the measured and simulated principal azimuth-plane radiation patterns for the dipole. Note that the simulated curve is difficult to see because it lies very close to the outer edge of the plot. Results indicate that the fabricated dipoles are less omnidirectional in azimuth than predicted through simulation; a variation of as much as 3 dB is observed. This is most likely due to the presence of the

SMA connector and feed cable, which would tend to direct the radiation pattern in the forward direction.

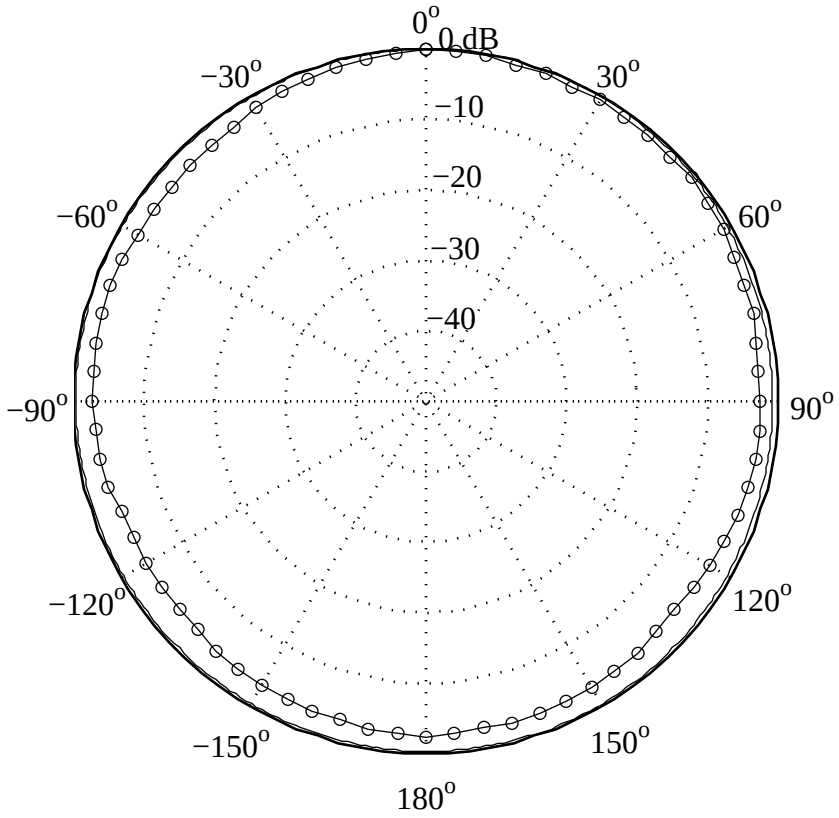

Figure 4.4: Measured and simulated azimuth-plane ($\theta = 90°$) radiation patterns for one of the printed dipoles. Solid: simulated and ∘: measured.

Finally, the maximum gain of the dipole was measured using the three antenna method [90]. A maximum gain of 2.0 dBi was obtained, which compared closely with the simulated value of 1.9 dBi. It would be reasonable to expect the measured gain to be lower than that obtained through simulation due to losses unaccounted for in CST Microwave Studio®. However, since it was found that the measured azimuth-plane radiation pattern slightly favoured the forward direction due to the presence of the feed apparatus, it is likely that the maximum directivity exhibited by the fabricated dipole is larger than that found through simulation. Consequently, even

if the measurements include extra losses it is still possible for the associated gain to exceed the simulated result. In any case, the measurements indicate that the printed dipoles behave largely as expected and are acceptable for use as PD and single-element AP antennas.

4.1.2 Phased-array AP Antennas

Since printed dipoles are used as radiating elements, it follows that each phased-array should consist of a single PCB which includes $N = 4$ such elements along with an appropriate feed network. The phased-arrays were required to be driven by a single coaxial input, deliver equal power to each element and support independent element phasing. A block diagram illustrating the phased-array design is shown in Figure 4.5. The corporate feed structure employing 3 dB splitters ideally serves to divide the input power among the element branches equally. It also ensures that the signals on each branch are in-phase prior to the implementation of the desired progressive phase shift.

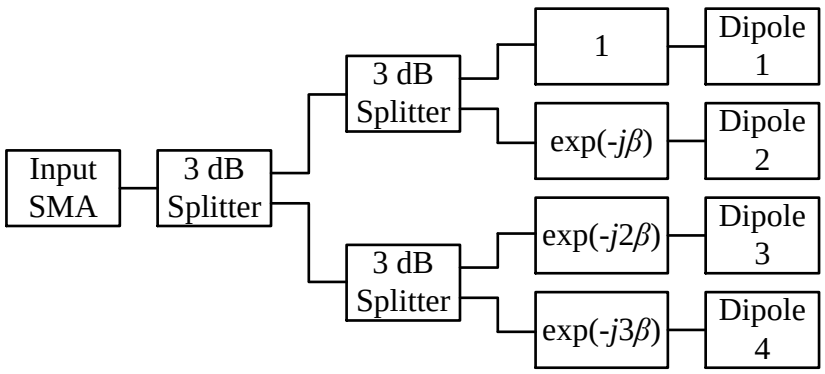

Figure 4.5: A block diagram illustrating the design of the phased-array AP antennas.

Microstrip transmission lines form the basis of the phased-array feed network as this type of line feeds the printed dipoles. An ideal microstrip line consists of

an infinite ground plane upon which rests an infinite dielectric slab of thickness d_{d} and a conductive trace of width d_{w}. An illustration of the cross-section of such a transmission line is shown in Figure 4.6. Since the dielectric is finite in thickness and does not envelop the trace, the fields associated with electromagnetic waves travelling along the line experience both the permittivity of free space and that of the dielectric. As a result, it is common to define the effective dielectric constant of the microstrip line, denoted by ϵ_{e}, which can be approximated as [104]

$$\epsilon_{\mathrm{e}} = \frac{\epsilon_{\mathrm{r}} + 1}{2} + \frac{\epsilon_{\mathrm{r}} - 1}{2} \frac{1}{\sqrt{1 + 12\left(\frac{d_{\mathrm{d}}}{d_{\mathrm{w}}}\right)}}. \tag{4.1}$$

Based on the desired characteristic impedance, Z_0, the ratio of the trace width to the thickness of the dielectric can be expressed for $d_{\mathrm{w}}/d_{\mathrm{d}} < 2$ as [104]

$$\frac{d_{\mathrm{w}}}{d_{\mathrm{d}}} = \frac{8\exp(a)}{\exp(2a) - 2}, \tag{4.2}$$

where

$$a = \frac{Z_0}{60}\sqrt{\frac{\epsilon_{\mathrm{r}} + 1}{2}} + \frac{\epsilon_{\mathrm{r}} - 1}{\epsilon_{\mathrm{r}} + 1}\left(0.23 + \frac{0.11}{\epsilon_{\mathrm{r}}}\right) \tag{4.3}$$

For example, achieving a 50 Ω microstrip transmission line on FR-4 board with a dielectric thickness of 1.6 mm and relative permittivity of 4.3 requires a trace width of approximately 3.1 mm; this is indeed the width of the trace feeding the printed dipole shown in Figure 4.1(a).

The 3 dB splitters in Figure 4.5 were implemented via equal-split Wilkinson power dividers. This type of divider is readily implemented using microstrip lines and presents a matched impedance at all three ports, exhibits isolation between the two output ports and is lossless provided that the outputs are match-terminated [104]. Figure 4.7 presents a block diagram illustrating the basic structure of the Wilkin-

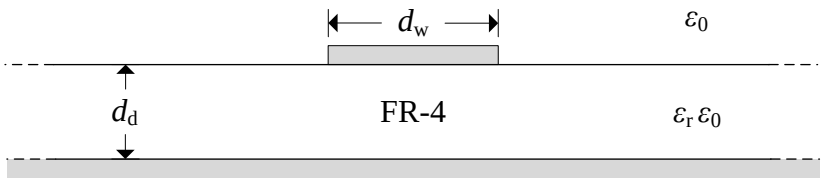

Figure 4.6: An illustration of the cross-section of a microstrip transmission line on FR-4 dielectric.

son power divider. The input is assumed to be a microstrip line of characteristic impedance Z_0 and is directly connected to two parallel microstrip lines of characteristic impedance $\sqrt{2}Z_0$. These lines are of length $l = \lambda_m/4$, where λ_m is the wavelength on the microstrip line. For the case of FR-4 and $Z_0 = 50\ \Omega$, the value of d_w associated with these microstrip lines is reduced to approximately 1.7 mm. The corresponding effective dielectric constant can be computed using Equation 4.1 to be approximately 3.1. Since λ_m is related to the free-space wavelength by [104]

$$\lambda_m = \frac{\lambda}{\sqrt{\epsilon_e}}, \tag{4.4}$$

the required length of these microstrip lines is approximately 17 mm. Each is directly connected to an output microstrip line of characteristic impedance Z_0. A lumped impedance of $2Z_0$—or 100 Ω in this case—is connected across the output terminals to ensure that they exhibit a matched impedance [104].

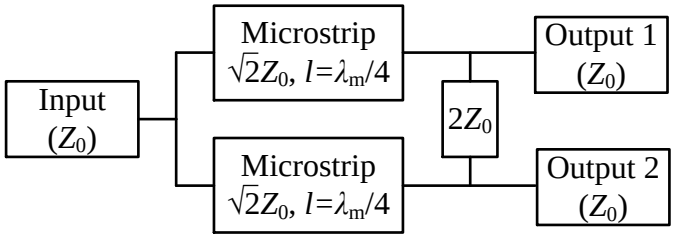

Figure 4.7: A block diagram illustrating the basic structure of the Wilkinson power divider.

Although RF phase shifters are available which would permit the main lobes of the phased-array radiation patterns to be steered electronically, the associated convenience would be outweighed by a significant increase in PCB complexity, prohibiting fabrication of the antennas at UNB. Furthermore, each antenna would require control and power lines in addition to the RF feed cable, which would act as additional sources of measurement inaccuracy and make the overall experimental set-up more cumbersome. Consequently, several sets of passive phased-arrays are used, each exhibiting a fixed main lobe elevation direction. Through in-room MIMO simulations it was determined that phased arrays with $\theta_0 = 90°$, $100°$, $110°$ and $120°$ would be sufficient to verify the findings of Chapter 3. The CST Microwave Studio® model for the printed dipole discussed in Section 4.1.1 was expanded to include four such elements separated by $s_e = 60$ mm on a single dielectric strip. Waveguide ports were defined to drive each element independently such that any value of β could be applied to the array without modelling the entire feed structure. Thus, the approximate β values required in order to achieve the desired main lobe elevation directions could be estimated; the results are summarized in Table 4.1.

Table 4.1: The θ_0 values desired for measurement purposes and the approximate β values required to achieve them for a 4-element array of printed dipoles with $s_e = 60$ mm.

Desired θ_0 (°)	Required β (°)
90	0
100	35
110	70
120	105

Phasing of the arrays is achieved by feeding the associated elements with microstrip transmission lines of different lengths. Referring to Figure 4.5, Dipole 2 would be fed by a transmission line which is longer than that feeding Dipole 1 by a length denoted by l_β. Similarly, the feeds for Dipole 3 and Dipole 4 would be longer by $2l_\beta$

and $3l_\beta$, respectively. Based on Equations 4.1 and 4.4, l_β can be expressed as

$$l_\beta = \frac{\lambda\,\beta}{2\pi\sqrt{\epsilon_\mathrm{e}}}, \tag{4.5}$$

where in this case the units of β would be radians. The value of ϵ_e associated with the 50 Ω microstrip line is approximately 3.3. Therefore, an l_β of approximately 6.6 mm would be required in order to achieve a θ_0 of 100°.

The feed networks for each phased-array were designed using ADS. In this way, the overall feed structure required to achieve the desired element phasing could be determined. A custom schematic symbol implementing the Wilkinson power divider was created and simulated separately to ensure proper operation. Where possible, right-angle bends in the microstrip lines were swept with a radius of curvature of $3d_\mathrm{w}$ to reduce the impact of the discontinuities [104]. In cases where sweeping was not practical, mitred bends were used [104]. Through simulation it was found that the loss in power delivered to each element due to conductor and dielectric losses in the PCB ranged from approximately 2.2–2.7 dB . The loss is not consistent for each element due to the additional microstrip line lengths used to achieve phasing. However, since the deviation is relatively low at less than 0.5 dB, the design was deemed acceptable.

PCB layouts for the phased-arrays were created in ADS and the boards were fabricated at UNB. Photographs of one of the completed phased-arrays exhibiting a θ_0 of 100° are shown in Figure 4.8. In addition to the edge-mount SMA input connector and the short wires required to complete the element feed networks, 100 Ω chip resistors were soldered to the board at the outputs of each of the Wilkinson power dividers.

The input VSWR was measured for each of the fabricated phased-arrays and it was confirmed to be less than 2:1 over the range of 2400–2483.5 MHz. Due to the complexity of the feed structure, the VSWR exhibited by the PCB input has little bearing on the radiation performance of the associated antenna. Consequently, the

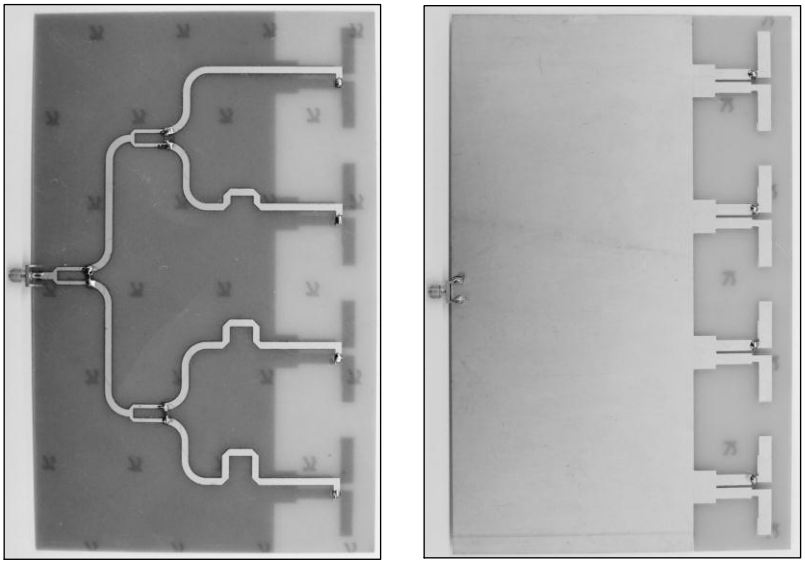

(a) Top layer photograph. (b) Bottom layer photograph.

Figure 4.8: Photographs of a fabricated phased-array exhibiting a θ_0 of 100°.

results of the VSWR measurements are not presented.

With the exception of the main lobe elevation angle, the antenna measurement results obtained for all of the fabricated phased-arrays are qualitatively similar. Therefore, only the results associated with one of the $\theta_0 = 100°$ antennas will be considered for ease and clarity of presentation. Figure 4.9 shows the measured and simulated elevation-plane ($\phi = 90°$) radiation patterns associated with this phased-array. There is a strong agreement between the simulated and measured results with respect to the shapes and elevation angles of the main lobes. The discrepancies associated with the minor lobes are largely attributed to the fact that the CST Microwave Studio® model did not include the feed network. Otherwise, the sources of error are similar to those associated with the printed dipole results in Section 4.1.1.

The measured and simulated azimuth-plane radiation patterns for the same antenna are presented in Figure 4.10. The simulated results are again difficult to see as they lie very near to the edge of the plot. The presence of the feed structure—

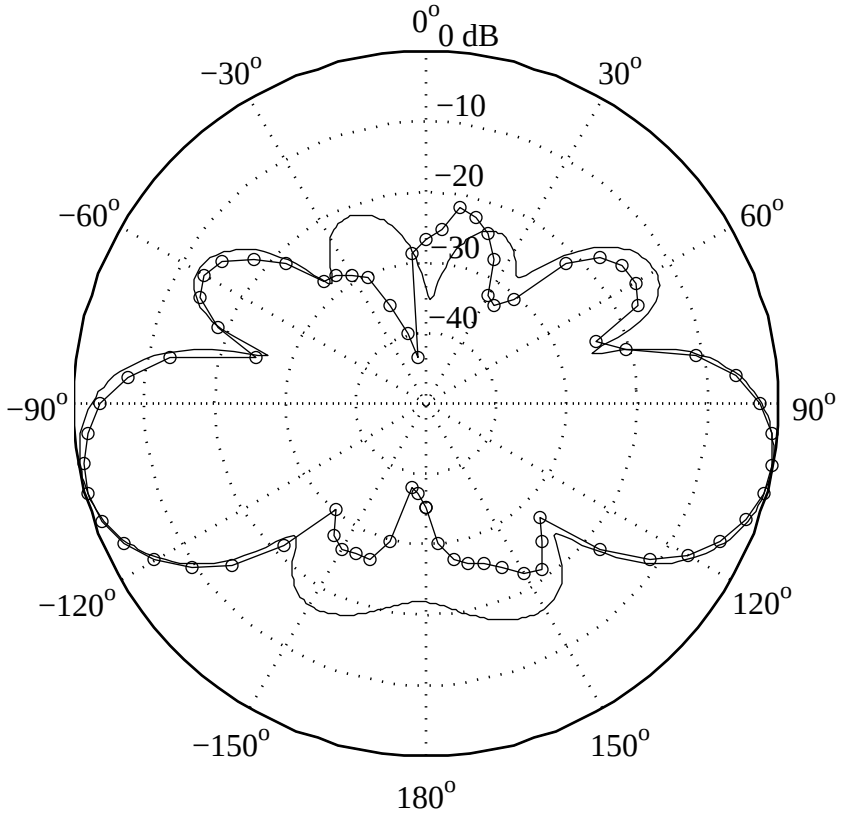

Figure 4.9: Measured and simulated elevation-plane ($\phi = 90°$) radiation patterns for one of the $\theta_0 = 100°$ phased-arrays. Solid: simulated and ∘: measured.

which was not included in the simulation—has a significant impact on the measured azimuth-plane pattern; instead of being omnidirectional, the pattern exhibits a front-to-back ratio of over 10 dB. This is unacceptable in the context of reproducing the conditions of the simulations from Chapter 3. Since the pattern is relatively constant from $-90° \leq \phi \leq 90°$, MIMO channel measurements obtained for PD locations in front of the antennas should be relatively accurate. Refer to Section 4.3 for more details regarding how this issue is addressed in the design of the experimental procedure.

The maximum gain exhibited by the fabricated phased-array was measured using the three antenna method [90] to be approximately 6.2 dBi, while the simu-

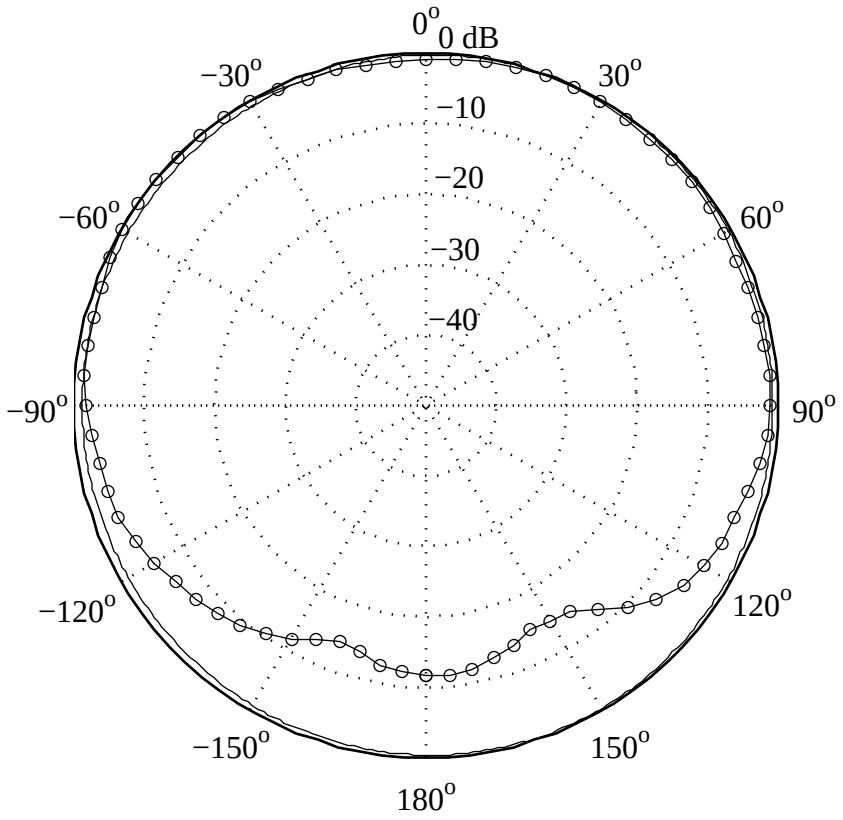

Figure 4.10: Measured and simulated azimuth-plane ($\theta = 100°$) radiation patterns for one of the $\theta_0 = 100°$ phased-arrays. Solid: simulated and ∘: measured.

lated gain was approximately 6.4 dBi. Considering the projected losses of 2.2–2.7 dB associated with the feed structure, the measured gain is higher than expected. However, both Figures 4.9 and 4.10 show that the fabricated phased-array tends to be more directive. Consequently, the maximum directivity is expected to be higher than that obtained through simulation, which most likely accounts for this discrepancy.

4.2 Room Selection and Characterization

Several factors impacted the selection of the room in which the channel measurements were taken. An unoccupied classroom was a logical choice due to availabil-

ity as the measurements were taken during the summer months and a general absence of conductive materials, which would not have been the case in a laboratory filled with equipment and computers. A classroom with reasonably square dimensions was desired in order to better match the simulation conditions. Furthermore, several of the classrooms on campus have been renovated such that they feature windows which have been treated with a low-emissivity (low-e) coating, making them near-perfect reflectors of radio signals [110]. This is undesirable because the presence of large and highly reflective planes along the walls would significantly reduce the dominance of the LOS components, making the use of θ-directional AP antennas somewhat unnecessary. Consequently, a classroom with regular windows was required. Unfortunately, the blackboard present in every classroom available exhibited near-perfect reflectivity and could not be avoided. This was addressed by tailoring the experimental set-up such that reflections coming from the associated wall are de-emphasized; refer to Section 4.3 for details.

Room HB-8 was ultimately chosen. Neglecting a small alcove at the entrance, the approximate dimensions of the room are $d_x = 9.1$ m, $d_y = 10.4$ m and $d_z = 3.1$ m. Three of the walls are made of concrete blocks while the fourth is made of plasterboard. One of the concrete block walls includes a set of regular windows while another supports the blackboard. The room features a tile floor and a dropped ceiling comprised of fibreglass tiles and lighting fixtures.

In order to characterize the room prior to the measurement campaign, the reflection losses associated with each of the boundary materials were measured via reflectometry. Figure 4.11 depicts the measurement set-up for the example of characterizing one of the walls. The PNA was configured for a reflection measurement on port 1 (S_{11}) over 1001 frequency points from 2–4 GHz and was calibrated to the end of an antenna feed cable. Applying an inverse discrete Fourier transform (IDFT) to the data yielded a time domain trace displaying the magnitudes and time delays

associated with all of the reflected signal components. The antenna consisted of a wideband horn specified for operation from 2–12 GHz. The maximum dimension of this horn is approximately 0.22 m, which results in a mid-band (3 GHz) far-field distance of approximately 0.97 m [90]. Consequently, the antenna was positioned 1 m from any obstructions. An aluminum sheet which exhibits a reflection loss of approximately 0 dB was used as a reference for the measurements. The required size of the sheet is governed by the half-power beamwidth (HPBW) associated with the radiation pattern of the horn, which is approximately 50° at 3 GHz. To a first approximation, the main lobe illuminates a circle of 0.9 m diameter at a distance of 1 m. As a result, a readily available square aluminum sheet of 1.2 m side-dimension was used.

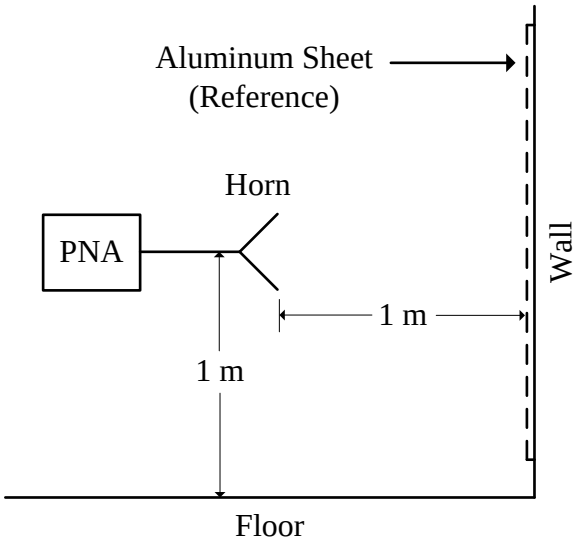

Figure 4.11: Reflectivity measurement set-up for determining the reflection loss associated with one of the classroom wall materials.

A plot of the reflected signal magnitude as a function of time for a section of concrete block wall is shown in Figure 4.12. The reference results obtained using the aluminum sheet in place of the wall are included for comparison. Below 7 ns, the two curves a very similar. The reflection due to the boundary occurs at approximately

8.8 ns; the magnitudes of the reflections due to the aluminum sheet and concrete block wall are approximately -29 dB and -37 dB, respectively. Therefore, the associated reflection loss at normal incidence is roughly 8 dB. This agrees reasonably well with the simulations of Chapter 3, which assumed a reflection loss of approximately 9.5 dB at normal incidence.

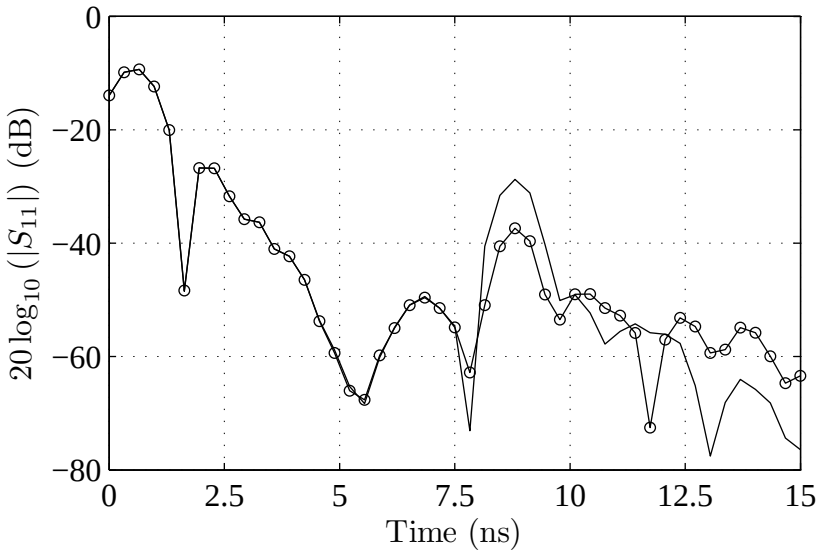

Figure 4.12: An example plot of the reflected signal magnitude as a function of time for a concrete block wall. Solid line: reference and ∘: wall.

In some cases, highly reflective objects located beyond the boundaries would generate stronger reflection components than the boundaries themselves. Figure 4.13 shows an example of this, in which the measured signal from the floor exhibited a strong secondary reflection. Consequently, the multipath richness associated with the real room may be higher than that predicted by the simulations, where signals which penetrated the boundaries were ignored. This phenomenon was only significant in the floor and ceiling measurements, where it is more likely that conductive surfaces would be present beyond the boundaries.

For each boundary, a number of measurements were taken and the results were

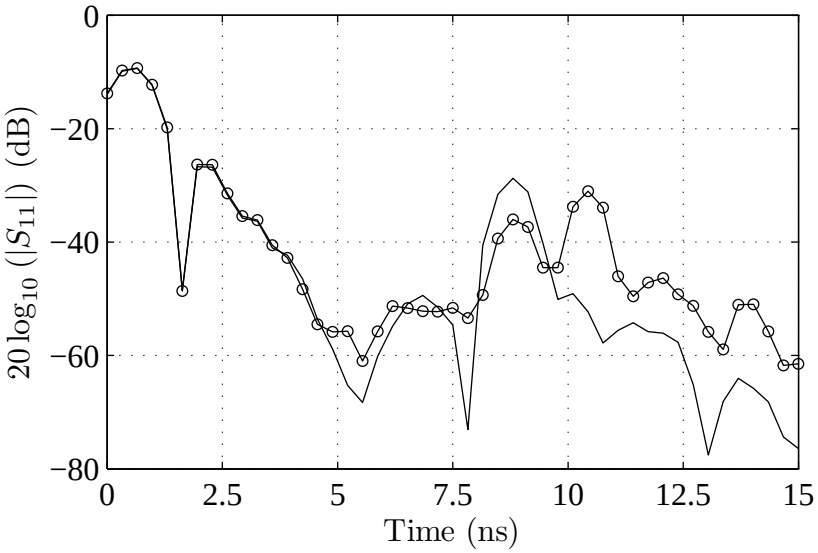

Figure 4.13: An example plot of the reflected signal magnitude as a function of time for the floor which shows a strong secondary reflection. Solid line: reference and ∘: floor.

averaged to give a first approximation to their electromagnetic behaviour. Table 4.2 summarizes the results. For the floor and ceiling results including multiple strong reflections, the averaging is based on the maximum observed reflection regardless of the associated time delay. Measurements associated with the windows and lighting fixtures are included in the averages computed for their respective boundaries; however, the effect of the blackboard is ignored as it is addressed in the design of the experimental procedure presented in Section 4.3.

In order to generate simulation results with which the measurements can be compared, the reflection losses included in Table 4.2 can be converted to relative permittivities. Let $|\Gamma_{\mathrm{RL}}|$ denote the magnitude of the normal-incidence boundary reflection coefficient associated with the reflection loss entries in Table 4.2. Assuming the boundary dielectrics to be lossless, the corresponding relative permittivity can be expressed as

Table 4.2: The average reflection losses and corresponding real-valued relative permittivities associated with the walls, floor and ceiling in room HB-8.

Boundary	Reflection Loss (dB)	Simulation ϵ_r (-)
Concrete Wall	7.5	6.0
Concrete Wall, Windows	8.3	5.1
Concrete Wall, Chalkboard	7.5	6.0
Plasterboard Wall	9.5	4.0
Floor	8.2	5.2
Ceiling	10.8	3.3

$$\epsilon_r = \left(\frac{1 - |\Gamma_{RL}|}{1 + |\Gamma_{RL}|} \right)^2 . \tag{4.6}$$

The results of these calculations have also been included in Table 4.2 for convenience.

4.3 Experimental Set-up and Procedure

An illustration of the complete measurement set-up is shown in Figure 4.14, while photographs of the most important components of the experiment are shown in Figure 4.15. The AP antennas were affixed to a table-mounted tripod located in the middle of the room; the resulting value of h_{AP} was 2.7 m. Due to the azimuth-directional nature of the phased-array AP antennas as evidenced by Figure 4.10, channel measurements could only be obtained for PD locations on one side of the room. The side opposite to the wall supporting the blackboard was used due to its near-perfect reflectivity at microwave frequencies. The AP antennas were separated along the x-direction by an s_{AP} of 1.5λ. By orienting the phased-arrays such that they were fed from the direction of the blackboard, the abnormally strong NLOS components incident from that direction were suppressed by the associated front-to-back ratios. A photograph of this AP configuration is shown in Figure 4.15(a). Since

the single-element AP antennas exhibit near-omnidirectional azimuth-plane radiation patterns as shown in Figure 4.4, the blackboard-reflected components were suppressed by suspending microwave absorber material with a measured attenuation of approximately 6 dB at 2.4 GHz in the far-field region behind the AP. Figure 4.15(b) shows a photograph of this AP configuration.

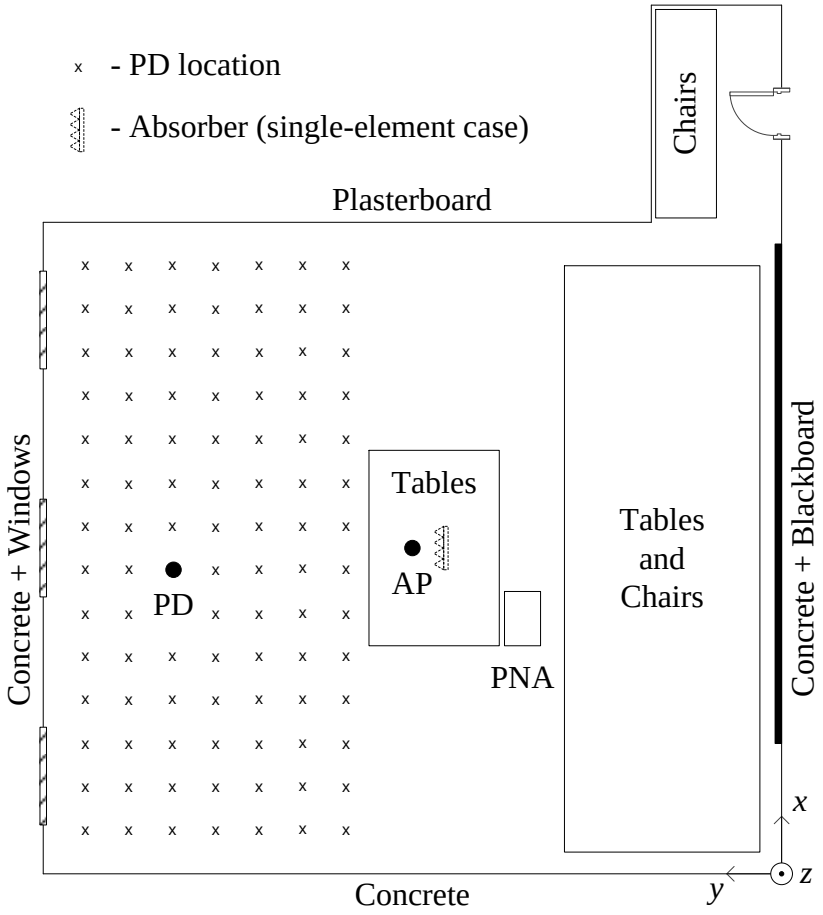

Figure 4.14: Experimental set-up.

The PD antennas were mounted on a floor-based tripod such that $h_{\mathrm{PD}} = 1$ m and the associated dipoles were separated along the x-direction by an s_{PD} of $\lambda/2$. A photograph of the PD is shown in Figure 4.15(c). The PD locations were defined by a 14 by 7 point grid in which the distance between adjacent points was approximately 0.6 m. This distance was also maintained between the locations on

the edges of the measurement area and the walls. Early experimentation revealed that the tables and chairs within the measurement area had only a minor impact on the results. The radiation patterns associated with the dipole-based antennas employed in the measurements most likely contributed to this behaviour; multipath components incident from above or below the antennas would be naturally suppressed. It is also worth noting that although the additional scattering from the tables and chairs would be expected to have a measurable effect on the channel conditions at a given PD location, it may not significantly contribute to the overall room coverage or the room-averaged performance metrics. On the other hand, the presence of the tables and chairs made moving the PD to each measurement location much more cumbersome. For these reasons, they were moved to the unused areas of the room.

Data acquisition was achieved using the PNA, which was located near and below the AP in an effort to minimize its effect on the measurements. Each antenna was connected to one of the four ports and the effects of the feed cables were removed via calibration. Figure 4.15(d) shows a photograph of the PNA set-up for the measurements. S-parameter data was obtained for 201 frequency samples over the range of 2400–2483.5 MHz. Therefore, the resulting frequency step, denoted by f_{step}, was 417.5 kHz. In the context of radio channel measurements, the unambiguous range, r_{unamb}, is defined as the range over which a received multipath component can be unambiguously related to a particular sounding pulse and can be expressed as [111]

$$r_{\text{unamb}} = \frac{c}{f_{\text{step}}}, \tag{4.7}$$

where c is the speed of light in free space. In this case, the unambiguous range is approximately 720 m which is more than sufficient for the in-room channel measurements. The PNA was configured such that all of the S-parameters were acquired and averaged before stepping to the next frequency point. This ensured that the effects of channel time-variation on the results could be readily observed; the traces were only

recorded when these variations were found to be negligible. An acceptable dynamic range was achieved with an averaging factor of 256.

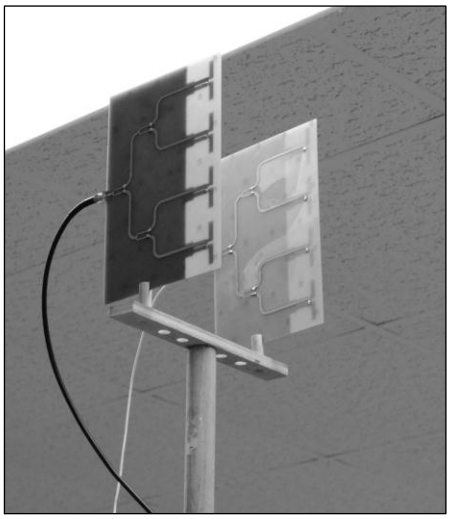

(a) Phased-array AP arrangement.

(b) Single-element AP arrangement with absorber.

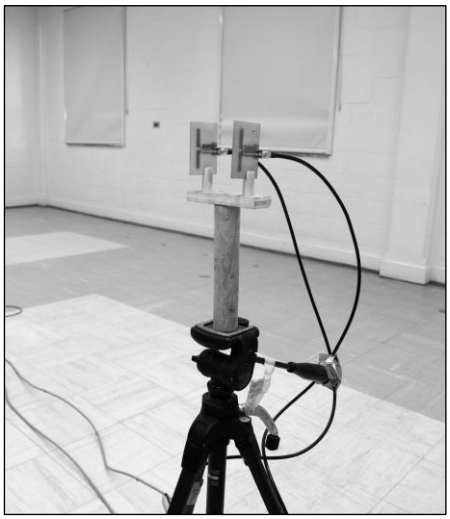

(c) PD arrangement.

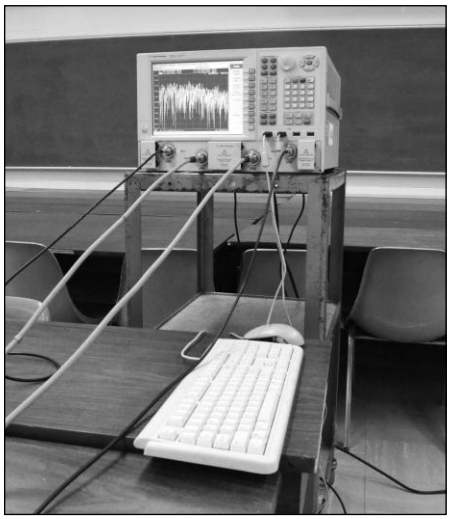

(d) PNA configured for S-parameter measurements.

Figure 4.15: Photographs of the AP, PD and PNA arrangements used during the measurements.

Each channel measurement involved placing the PD at the appropriate location, returning the PNA to restart the averaging and, once averaging was complete, recording the associated S-parameter data. The operator was therefore seated by the

PNA throughout the measurements. The AP antennas were connected to ports 1 and 2 on the PNA during the measurements while the PD antennas were connected to ports 3 and 4. As a result the relevant S-parameters were S_{13}, S_{14}, S_{23} and S_{24}. Channel measurements were conducted at all of the PD locations for each of the AP configurations under consideration.

4.4 Results

Based on the measured S-parameter results, the performance metrics given by Equations 3.51, 3.54 and 3.55 were computed; the effects of mutual coupling were neglected. The ratio $P_{\mathrm{T}}/P_{\mathrm{N}}$ was again assumed to be 80 dB and in this case the value of K was 201. The CTMs can be expressed in terms of the measured S-parameters as

$$\mathbf{H}_k = \begin{bmatrix} \mathrm{S}_{13k} & \mathrm{S}_{14k} \\ \mathrm{S}_{23k} & \mathrm{S}_{24k} \end{bmatrix}. \tag{4.8}$$

Figure 4.16 presents the room-averaged performance results. The in-room MIMO simulation parameters were adjusted to model the measurement scenario as closely as possible and the associated results are included for convenience. Although the simulation model is idealized, it does predict the qualitative behaviour of each of the performance metrics with θ_0 reasonably well. This is evident given that the measured $\overline{C_{\mathrm{MIMO}}}$, $\overline{\rho_{\mathrm{dB}}}$ and $\overline{g_C}$ results for phased-array AP antennas follow curves which are similar to those associated with the simulated results as a function of θ_0.

The increased multipath richness associated with the real environment results in a higher measured $\overline{C_{\mathrm{MIMO}}}$ relative to the simulated value for the case of single-element AP antennas; the associated $\overline{\rho_{\mathrm{dB}}}$ and $\overline{g_C}$ values are also higher. Of course, antennas which are relatively non-directional benefit more strongly from a rich multi-

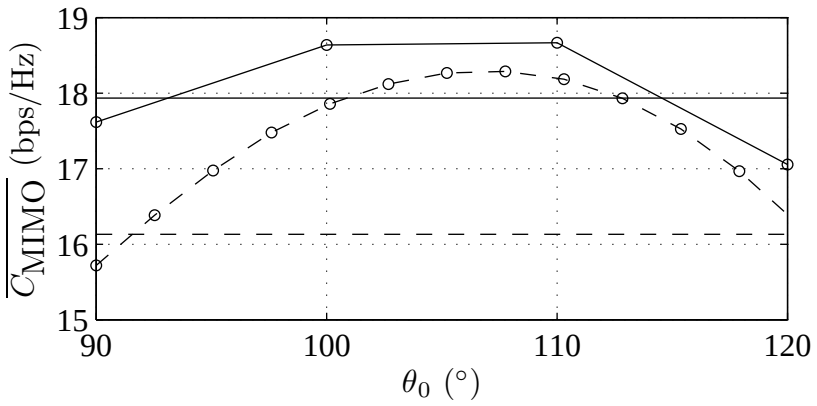

(a) $\overline{C_{\mathrm{MIMO}}}$.

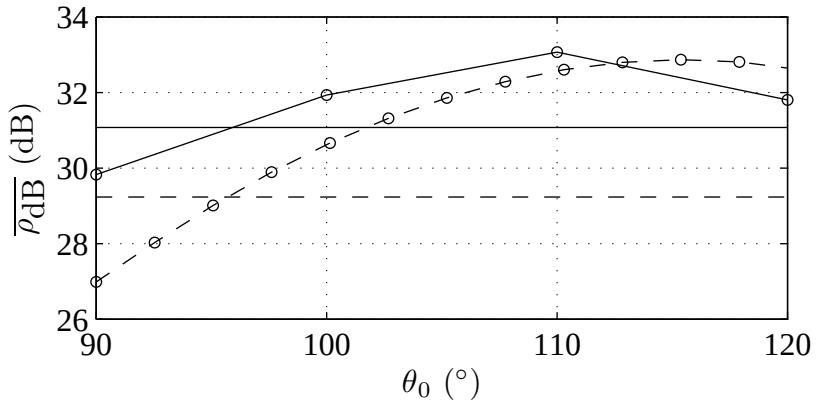

(b) $\overline{\rho_{\mathrm{dB}}}$.

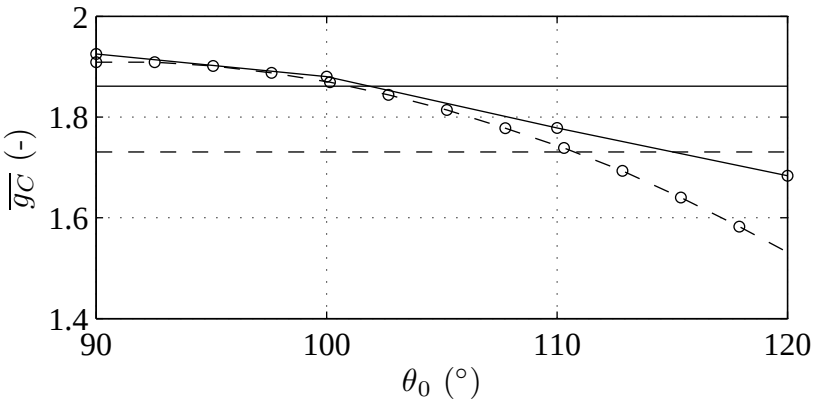

(c) $\overline{g_C}$.

Figure 4.16: Measured and simulated room-averaged performance metrics as functions of θ_0. Solid line: measured single-element, ∘: measured phased-array, dashed line: simulated single-element and dashed ∘: simulated phased-array.

path environment because they receive signals nearly equally from all directions. As a result, the measured improvements associated with the use of θ-directional AP antennas are modest relative to those observed through simulation. The peak improvement in the simulated $\overline{C_{\text{MIMO}}}$ relative to the single-element case occurs for $\theta_0 = 106°$ and is approximately 13 %. A relative improvement of only 4 % is observed in the measured results for $\theta_0 = 110°$. Since the shapes of the measured and simulated $\overline{C_{\text{MIMO}}}$ curves are quite similar, it is reasonable to suggest that better $\overline{C_{\text{MIMO}}}$ measurement results would be obtained for $\theta_0 \approx 106°$, in which case an improvement of 5 % might be expected. Unfortunately, the measured results indicate that operation at this steering angle would result in a net decrease in $\overline{g_C}$. It may be possible to achieve more significant performance improvements for in-room MIMO systems experiencing less multipath richness. This may be the case for systems operating in higher frequency bands; for example, a similar model to the one used in Chapter 3 was used to assess the feasibility of indoor millimetre-wave MIMO [112]. The use of phased-arrays with $N = 8$ elements may also be more physically feasible when operating at higher frequency bands, which could lead to more significant performance improvements. Finally, the results shown in Figure 4.16 were obtained with half-wavelength dipole elements, which inherently exhibit strong single-element in-room MIMO performance; the measured performance improvements may be more significant for other element types.

While the room-averaged results for C_{MIMO}, ρ_{dB} and g_C provide valuable insight regarding the relationship between θ_0 and MIMO performance, they do not express the degree of performance variability throughout the room. For the simulated results of Chapter 3, this variability was investigated via surface plots of C_{MIMO}. This approach is relatively ineffective when considering measured data obtained in a real room as there is far less order and symmetry to the behaviour of the environment. As a result, the observed spread in MIMO capacity results is investigated based on

the associated empirical cumulative distribution functions (CDFs). Figure 4.17 shows the empirical CDF curves associated with each of the AP antenna configurations.

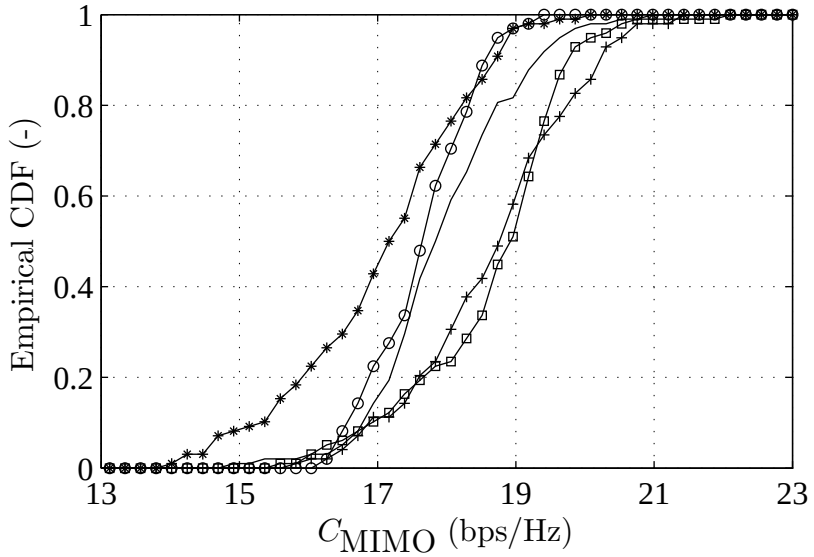

Figure 4.17: Empirical CDFs for the measured C_{MIMO} results. Solid line: single element, $\circ$: phased array with $\theta_0 = 90°$, $\square$: phased array with $\theta_0 = 100°$, $+$: phased array with $\theta_0 = 110°$ and $*$: phased array with $\theta_0 = 120°$.

The empirical CDFs for the $\overline{C_{\mathrm{MIMO}}}$-improving cases of $\theta_0 = 100°$ and $110°$ show that the spreads in the observed capacity values are comparable to that of the single-element case. It is interesting to note that the spread is smallest for $\theta_0 = 90°$ and tends to increase as the main lobe is tilted down toward the PD. This suggests that employing AP antennas with radiation patterns which avoid the LOS components might give more reliable capacity performance in addition to increasing $\overline{g_C}$.

4.5 Summary

Improving in-room MIMO capacity through the use of θ-directional AP antennas which emphasize wall-reflected NLOS components has been investigated experimentally in an unoccupied classroom. Through both measurement and simulation, it

was found that the application of phased-array AP antennas did not significantly affect the MIMO capacity coverage throughout the room. While simulations projected room-averaged MIMO capacity improvements on the order of 13 % coupled with minor increases in room-averaged relative MIMO gain, the measured results revealed more modest performance improvements due to the increased multipath richness exhibited by the real environment relative to the idealized simulation environment. The results suggested that a room-averaged capacity improvement on the order of 5 % could be achieved, but this would be accompanied by a minor degradation in room-averaged relative MIMO gain. Since the relationships between the room-averaged performance metrics and the main-lobe θ-directions of the AP antenna radiation patterns were well-defined by the simulation model in a qualitative sense, it is possible that more significant performance improvements could be obtained for in-room MIMO systems experiencing less multipath richness.

Chapter 5

Performance Evaluation of Conductive-paper Dipole Antennas

Antennas are typically constructed using metals such as copper or aluminium. The widespread use of these metals as conductors can be attributed to the fact that they are highly conductive, linear and isotropic. However, in applications such as UHF RFID tag design, the cost of the antenna is a significant portion of the total cost of the tag. Consequently, there has been recent interest in investigating more cost-effective antenna conductor materials at the expense of radiation efficiency [9].

The use of silver ink has been proposed as a low-cost alternative to copper in UHF RFID tag design [8]. Despite the fact that silver ink is less conductive than copper, a carefully designed silver ink antenna can offer similar performance to a corresponding copper antenna [8]. In addition, silver ink antennas can be applied to an appropriate substrate via inkjet-printing technology, which is a cost- and resource-efficient alternative to the wet-etching technique typical of copper RFID tag antennas [113]. In a further effort to lower antenna costs, the effect of reducing the thickness of the printed silver-ink antennas to a single skin depth was studied [114] and the resulting performance degradation was found to be acceptable for some ap-

plications.

Advanced carbon-fibre composites have also been introduced for the purpose of antenna construction [9,115]. Along with conductivities of 10^3 to 10^4 S/m, carbon-fibre composites exhibit more favourable structural properties than most metals such as a high strength-to-weight ratio. Reduction in antenna radiation efficiency due to the relatively low material conductivity can be mitigated by increasing the conductor thickness [9].

Electrically conductive paper has recently been developed by Huang et al. [10, 11] as a low cost and eco-friendly material for applications such as electrostatic discharge (ESD) packaging. The feasibility of constructing antennas using conductive paper will be presented here, with a focus on application to UHF RFID systems. It should be noted that this research is largely unrelated to that presented in Chapters 3 and 4, which dealt with improving in-room MIMO capacity using elevation-directional access point antennas. Both sets of contributions involve the development of antennas to meet specific goals relating to wireless communication systems, otherwise they are independent.

5.1 Conductive Paper

Conductive paper consists of pulp in which the cellulose fibres have been modified with a conductive polymer [11]. The result is a conducting material which is otherwise very similar to regular paper. For example, the tensile strength of conductive paper is very similar to that of regular paper. Since the conductive fibres are realized using polymers as opposed to metals, conductive paper is still biodegradable and can be recycled [11]. A conductive paper design can therefore be easily integrated into a sheet of regular paper. In the case of UHF RFID tag design, an antenna made of conductive paper could be built into the packaging of a product and recycled along

with it. This would greatly increase the eco-friendliness of RFID systems, in addition to reducing costs.

5.1.1 Conductivity Measurement

The conductivity of the paper was measured using the van der Pauw method. It is a four-point conductivity measurement technique which can be applied to a flat sample of arbitrary shape without knowledge of the associated current pattern so long as the following conditions are met [116]:

- the measurement contacts are at the edge of the sample;
- the measurement contacts are very small relative to the surface area of the sample;
- the sample is isotropic and homogeneous in both conductivity and thickness; and
- the surface of the sample is singly connected, meaning that it does not have any isolated holes.

A theoretical treatment of the van der Pauw method can be found in Appendix B.

The measurement set-up for determining the paper conductivity is depicted in Figure 5.1. A sample was prepared by cutting a thin sheet of conductive paper into a square as symmetrical sample geometries simplify the conductivity calculations [116]. Wires were connected to each corner using relatively small amounts of conductive epoxy and the resulting test points were designated as A, B, C and D. A power supply configured as a current source was used to drive a current through points A and B, denoted by I_{AB}, while the voltage appearing across points D and C, denoted by V_{DC}, was measured. The resistance $R_{\mathrm{AB,CD}}$ was then obtained by dividing V_{DC} by I_{AB}. In a similar manner, the resistance $R_{\mathrm{BC,DA}}$ was obtained. The thickness of the paper

sample was measured using a caliper. Care was taken to apply a minimal amount of force to the paper to avoid any deformation. A variety of thickness measurements were taken at different points on the sample and averaged. Given the symmetry of the sample, the resistances $R_{\mathrm{AB,CD}}$ and $R_{\mathrm{BC,DA}}$ were similar, allowing the material conductivity, σ, to be expressed as [116]

$$\sigma = \frac{\ln 2}{\pi d_{\mathrm{t}}} \left(\frac{2}{R_{\mathrm{AB,CD}} + R_{\mathrm{BC,DA}}} \right), \tag{5.1}$$

where d_{t} is the thickness of the sample. This technique was applied to a 0.4 mm thick paper sample and a 1 mm thick paper sample. The resulting conductivities were 52.6 S/m and 45.5 S/m, respectively. The nominal conductivity of the paper is therefore taken to be approximately 50 S/m.

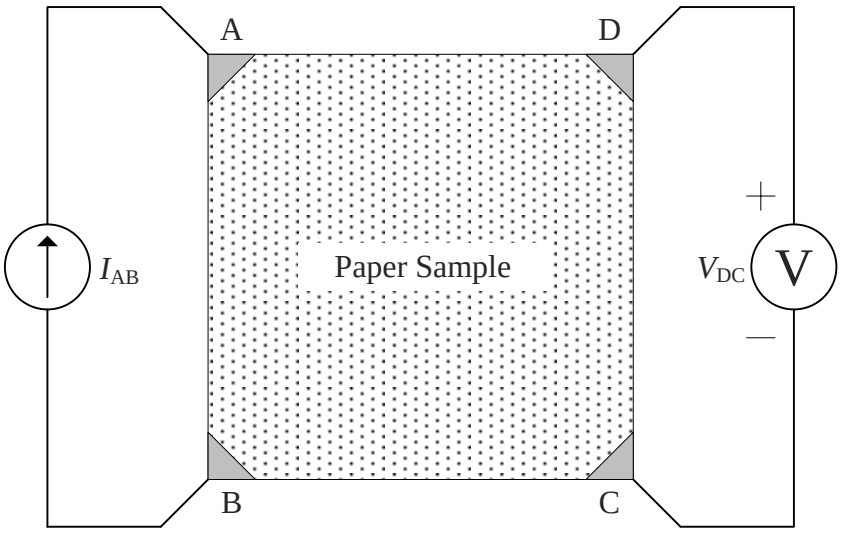

Figure 5.1: Measurement set-up for determining the conductivity of a paper sample using the van der Pauw method.

Since this conductivity is quite low, a dipole constructed using the conductive paper is expected to be lossy. Lossy dipole antennas have been explored mathematically [117, 118] and numerically [119] and the resulting concepts have been applied

to the development of semiconductor antennas [120] and carbon nanotube antennas [121]. CST Microwave Studio® will be used here to characterize the lossy nature of a conductive-paper antenna.

5.1.2 Antenna Construction

A conductive-paper dipole antenna of rectangular conductor cross-section was constructed. The basic dimensions of the prototype are shown in Figs. 5.2(a) and 5.2(b), while a photograph of the feed network is shown in Figure 5.2(c). A centre frequency of 915 MHz was chosen; therefore, the length of the antenna was 164 mm, or half of a free space wavelength. Although paper samples of thickness 0.4 mm and 1 mm were available, the 0.4 mm thickness is standard. The antenna was adhered to an FR-4 board using epoxy for mechanical support. Thin wires were bonded to the antenna using conductive epoxy and served to connect the antenna to an SMA connector through a 2:1 balun (Mini-Circuits® TCN2-122+).

5.2 Paper Antenna Modelling

The antenna was modelled using CST Microwave Studio®. The geometry depicted in Figures 5.2(a) and 5.2(b) was implemented; the antenna was driven by a discrete S-parameter port for simplicity. While all of the key results are evaluated at the centre frequency of 915 MHz, the frequency range of the excitation signal was configured to extend from 415 MHz to 1415 MHz. The FR-4 board upon which the antenna conductors were adhered was simply modelled using the lossy FR-4 material library entry; however, additional steps were required in order to effectively model the conductors over the conductivity range of 1 S/m to 10^8 S/m due to the skin effect.

The lossy behaviour of the antenna conductors is characterized by the associated ohmic resistance per unit length, denoted by R_{lo}. While general formulations

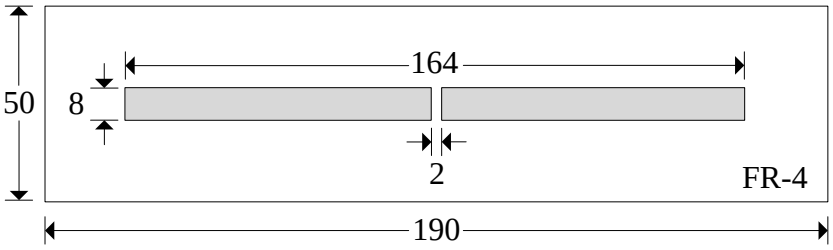

(a) Top view (without feed network).

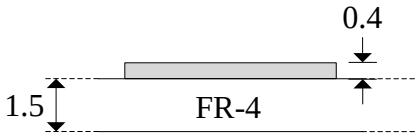

(b) Side view.

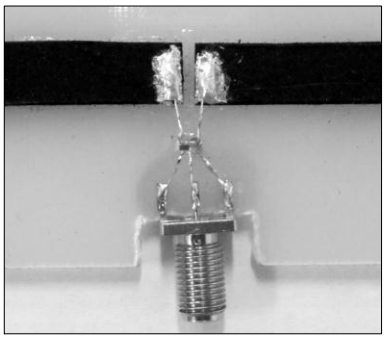

(c) A photograph of the feed network.

Figure 5.2: Paper antenna prototype construction details (dimensions are in mm).

are often difficult to obtain, the value of R_{lo} can be approximated based on whether or not the conductor thickness is larger than the corresponding skin depth, δ_s, given by [100]

$$\delta_s = \sqrt{\frac{1}{\pi \mu \sigma f}}, \tag{5.2}$$

where μ and σ are the material permeability and conductivity respectively. For example, at 915 MHz the skin depth in conductive paper is approximately 2.4 mm, while in copper—which exhibits a conductivity of approximately 5.8×10^7 S/m—it is only 2.2 μm. If the thickness of a conductor is less than the corresponding skin depth, it is assumed that the current density is uniform over the cross-section of the conductor; this situation is depicted in Figure 5.3(a). In this case, R_{lo} can be approximated as

$$R_{lo} \approx \frac{1}{d_{\mathrm{w}} d_{\mathrm{t}} \sigma}, \qquad d_{\mathrm{t}} < \delta_s, \tag{5.3}$$

where d_{w} and d_{t} are the width and thickness of the conductor cross-section, respectively. For conductors with thicknesses exceeding the skin depth, the current density decreases exponentially as one moves from the edge of the cross-section to the centre. This is considerably more complex to model; however, it is often a reasonable approximation to assume that the current is uniformly distributed along the perimeter of the conductor cross-section to a depth equal to δ_{s} [122]. This is depicted in Figure 5.3(b) and the corresponding expression for R_{lo} is

$$R_{lo} \approx \frac{1}{2(d_{\mathrm{w}} + d_{\mathrm{t}})\delta_s \sigma}, \qquad d_{\mathrm{t}} > \delta_s. \tag{5.4}$$

If the width of the conductor is much larger than the thickness, d_{t} can be dropped from Equation 5.4, which effectively means that the three-dimensional conductor is modelled as a two-dimensional conductive sheet. In any case, R_{lo} can be reduced by increasing either the conductivity or the dimensions of the conductor cross-section. Since increasing the cross-section dimensions results in a more expensive antenna, only changes in conductivity will be considered.

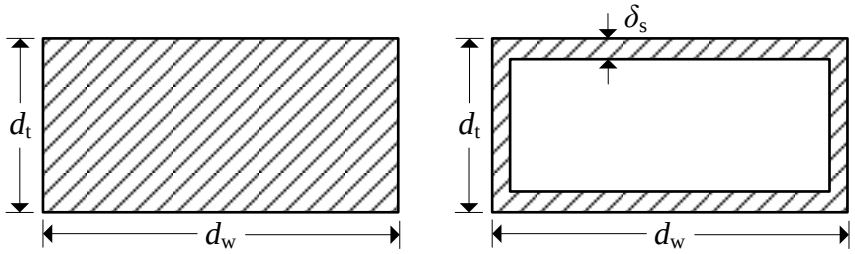

(a) $d_{\mathrm{t}} < \delta_{\mathrm{s}}$. (b) $d_{\mathrm{t}} > \delta_{\mathrm{s}}$.

Figure 5.3: Illustrations of the approximate current density distribution over the cross-section of a rectangular conductor.

In CST Microwave Studio® the midpoint between the approximations illustrated by Figures 5.3(a) and 5.3(b) occurs when the conductivity is approximately

10^5 S/m. Below this threshold, the antenna conductors are modelled using the material library entry for paper, with the electrical conductivity set to the desired value. In an effort to properly model the skin effect for conductivities near 10^5 S/m, a local edge refinement factor of 10 is applied to the conductors so that there is a much greater concentration of mesh cells near their edges. Expert-system-based mesh adaptation is applied, with the change in R_{lo} between successive mesh realizations acting as a metric for convergence. In other words, the simulation results are deemed acceptable when R_{lo} is found to be relatively insensitive to further mesh refinement. Unfortunately, mesh convergence could not be achieved for conductivities below 500 S/m. This is because the conductors become so lossy at these conductivities that the antenna begins to resemble an open circuit. A mesh realization achieved via convergence for a higher conductivity was therefore used for these conductivities; the associated results are expected to be less accurate than those obtained for conductivities of 500 S/m and above.

For conductivities above 10^5 S/m, the antenna conductors were modelled more effectively using the lossy metal material type. Under normal conditions, accurately modelling the current flow in a good conductor would require a huge number of mesh cells as the skin depth would be very small. The lossy metal material type addresses this issue by making similar assumptions as those associated with Figure 5.3(b) and Equation 5.4; the three-dimensional conductor is modelled by a two-dimensional conductive sheet based on the skin depth of the material. The sensitivity of R_{lo} to the mesh was again used as a metric for convergence, but the energy-based mesh adaptation scheme was found to be more effective in this case. A local edge refinement factor of 10 was applied to the antenna conductors as before.

5.2.1 Current Distribution

The relevant properties of a dipole antenna are primarily derived from the antenna current. Assume that to a first approximation the dipole can be considered filamentary, which means that it resembles a conducting line as opposed to a three-dimensional structure. If the antenna is oriented along the z-axis, the associated current is expressed as [123]

$$i(z,t) = I_0\, I(z)\, \exp(-j2\pi f t), \tag{5.5}$$

where $i(z,t)$ is the antenna current, I_0 is the peak current, $I(z)$ is the normalized current distribution.

For a half-wavelength dipole, it is typical to assume that $I(z)$ is sinusoidal with z, vanishing at the antenna end points [90]. However, this is not necessarily the case for antennas which are lossy and non-filamentary. In general the current distribution depends on the dimensions of the conductors and R_{lo}; a sinusoidal current distribution is observed only when the antenna is constructed using lossless and filamentary conductors [117, 124]. Relatively little attention will be given to the non-filamentary nature of the paper antenna conductors in the interest of focusing on the relationship between conductivity and antenna performance.

The current distributions were computed in CST Microwave Studio® by defining a set of curves upon which the magnetic field intensity could be evaluated. More specifically, 25 loops encircling the conductors were defined along the length of the antenna and the corresponding tangential components of the magnetic field intensity were obtained for each in post processing. The total current passing a particular loop could then be obtained by simply integrating the tangential magnetic field intensity along its circumference. Performing this for every loop yielded a set of current values which defined the antenna current distribution.

Figure 5.4 shows the $I(z)$ curves for a variety of conductivities. Above approximately 500 S/m the lossy nature of the conductor has little effect on the current distribution; in terms of antenna properties only the radiation efficiency and therefore the gain of the antenna would benefit from further increases in conductivity. The distribution is not perfectly sinusoidal for conductivities above 500 S/m due to fringing electric fields at the conductor edges [125] and the presence of the dielectric material, both of which serve to increase the electrical length of the conductor. For lower conductivities, such as those exhibited by conductive paper, the current distribution appears to be dampened by an exponential decay. As a result, the corresponding current is relatively strong at the feed point but almost non-existent near the ends of the antenna.

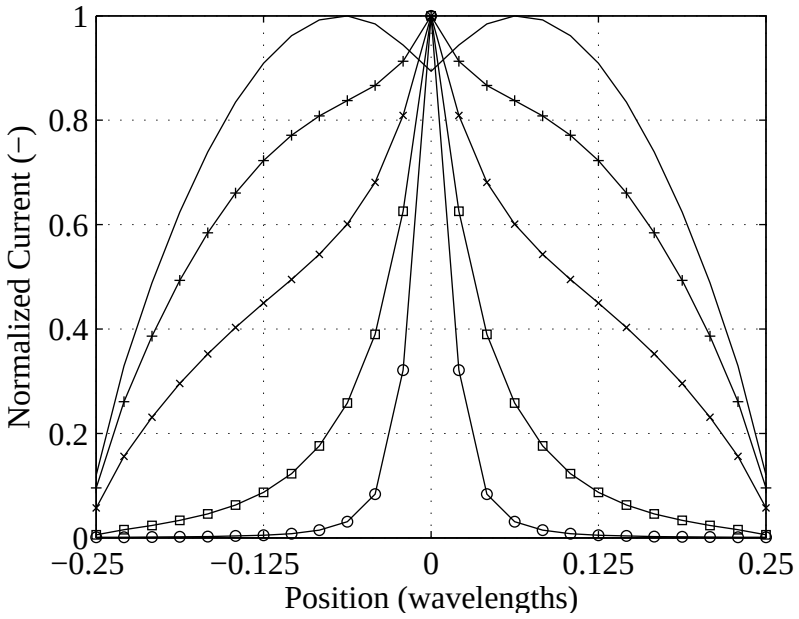

Figure 5.4: Plots of $I(z)$ along the antenna for a variety of paper conductivities. ○: $\sigma = 1$ S/m, □: $\sigma = 10$ S/m, ×: $\sigma = 50$ S/m, +: $\sigma = 100$ S/m, solid: $\sigma \geq 500$ S/m.

5.2.2 Input Impedance

The impedance at the input terminals of an antenna is of considerable practical importance because the impedance of the source which drives the antenna must be its complex conjugate in order to achieve maximum power transfer. Consider

$$Z_{\text{in}} = R_{\text{in}} + jX_{\text{in}}, \tag{5.6}$$

where R_{in} is the input resistance and X_{in} is the input reactance. The input resistance can be further expressed as the sum of the loss resistance, R_{loss}, and the radiation resistance. In the context of the equivalent circuit model for an antenna, the loss resistance accounts for the power dissipated by driving current through the lossy antenna conductors. If the dipole is oriented along the z-axis and approximately filamentary, the loss resistance can be expressed as [123]

$$R_{\text{loss}} = R_{lo} \int_{-l/2}^{+l/2} |I(z)|^2 \, dz. \tag{5.7}$$

As the antenna conductors become increasingly lossy, the result of the integral in Equation 5.7 reduces due to the aforementioned dampening of $I(z)$; however, the direct proportionality between R_{loss} and R_{lo} outweighs this effect and an overall increase in loss resistance is observed.

For a filamentary dipole antenna, R_{rad} can be expressed in terms of $I(z)$ as

$$R_{\text{rad}} = \frac{\eta\pi}{2\lambda^2} \int_0^{\pi} \left| \int_{-l/2}^{+l/2} I(z) \, \exp\left(-j\frac{2\pi}{\lambda} z \cos\theta\right) dz \right|^2 \sin^3\theta \, d\theta. \tag{5.8}$$

Therefore, the radiation resistance is expected to decrease once the antenna conductors become lossy enough that $I(z)$ is affected.

In CST Microwave Studio®, the use of an S-parameter port to drive the antenna allows the input impedance to be readily obtained in post processing. The values of R_{rad} and R_{loss} can then be computed based on the antenna radiation effi-

ciency, discussed in Section 5.2.3.

The antenna input and radiation resistances are plotted versus conductivity in Figure 5.5. As expected, for low conductivities the input resistance is dominated by R_{loss}, exhibiting very high values. It should be noted that the R_{in} curve begins to level off unexpectedly for conductivities below 5 S/m; this is a result of the aforementioned simulation inaccuracies arising due to the overly lossy nature of the antenna at low conductivities. As the conductivity increases and R_{loss} decreases the input resistance asymptotically approaches R_{rad}.

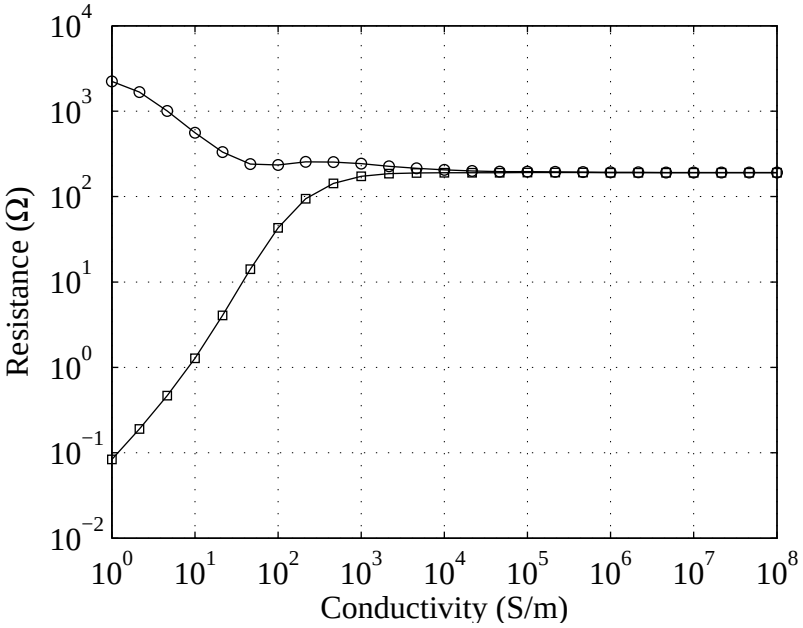

Figure 5.5: The input and radiation resistances of the paper dipole antenna as a function of paper conductivity. ∘: R_{in} and □: R_{rad}.

Since the current along the antenna diminishes for low conductivities, the associated radiation resistance becomes very small. As the conductors approach the lossless case, R_{rad} quickly increases, reaching its final value of approximately 190 Ω near 10^4 S/m. A radiation resistance of 73 Ω is typically expected for a half-wavelength dipole; however this quantity varies significantly based on the electrical size of the conductor cross-section [117, 124]. The radiation resistance at 50 S/m is only 16 Ω,

while at 500 S/m it is 141 Ω which is reasonable.

Where possible, it is common to design antennas such that they are resonant at the centre frequency of interest; in other words, $X_{\text{in}} = 0\ \Omega$ at the centre frequency. For example, trimming the length of a lossless filamentary dipole antenna to 95 % of one half-wavelength reduces the input impedance to approximately $70 + j0\ \Omega$, which matches well with the 75 Ω characteristic impedance typical of coaxial transmission lines employed in telecommunication systems. Unfortunately, this is not always possible as the antenna conductors become increasingly lossy. Figure 5.6 shows the input reactance as a function of frequency for a variety of conductivities. For conductivities exceeding 500 S/m the curves cross the $X_{\text{in}} = 0\ \Omega$ line, meaning that the resonance condition can be met by adjusting the length of the antenna. Below 500 S/m, X_{in} never reaches a value of 0 Ω, meaning that an external matching network would be required to achieve resonance.

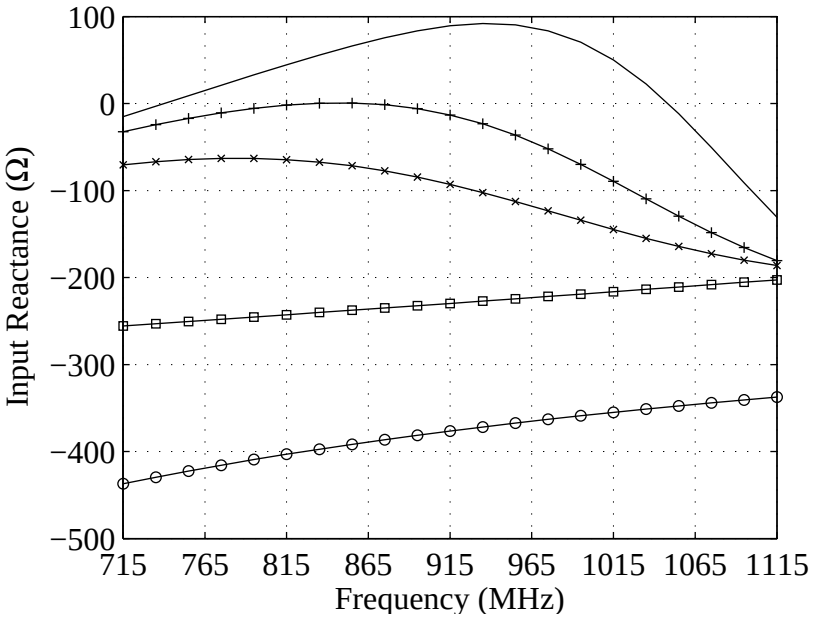

Figure 5.6: Plots of X_{in} as a function of frequency for a variety of paper conductivities. ○: $\sigma = 10$ S/m, □: $\sigma = 50$ S/m, ×: $\sigma = 200$ S/m, +: $\sigma = 500$ S/m, solid: $\sigma = 10^8$ S/m.

5.2.3 Radiation Efficiency, Directivity and Gain

The value of R_{lo} has a significant impact on the radiation efficiency of the antenna, e_{rad}, which is defined as the ratio of total radiated power to the total power delivered to the antenna input terminals. It can be expressed in terms of R_{rad} and R_{loss} as [90]

$$e_{\text{rad}} = \frac{R_{\text{rad}}}{R_{\text{rad}} + R_{\text{loss}}}. \tag{5.9}$$

Based on Equation 5.9 and the fact that R_{loss} increases and R_{rad} diminishes as R_{lo} grows large, it is evident that the radiation efficiency of an antenna degrades quickly as the conductors become more lossy.

Antenna radiation efficiency can be obtained in CST Microwave Studio® as a far-field result in post processing; this is also the case for directivity and gain, discussed later. Figure 5.7 shows a plot of e_{rad} at 915 MHz as a function of conductivity. As expected, the radiation efficiency decreases from close to 100 % for high conductivities to nearly 0 % for low conductivities. The radiation efficiency at 50 S/m is approximately 6.7 %, suggesting that an antenna constructed using the current conductive paper technology would be a poor radiator. It is also interesting to note that if the conductivity of the paper was 500 S/m the corresponding radiation efficiency would be 56 %. Since the current distribution will have already reached its final shape, increasing the conductivity beyond 500 S/m improves efficiency largely by reducing R_{loss}.

In the context of antenna parameters which can be easily measured, the reduction of e_{rad} with increasing conductor losses most significantly impacts the maximum gain of the antenna, G_0, which is expressed as [90]

$$G_0 = e_{\text{rad}}\, D_0, \tag{5.10}$$

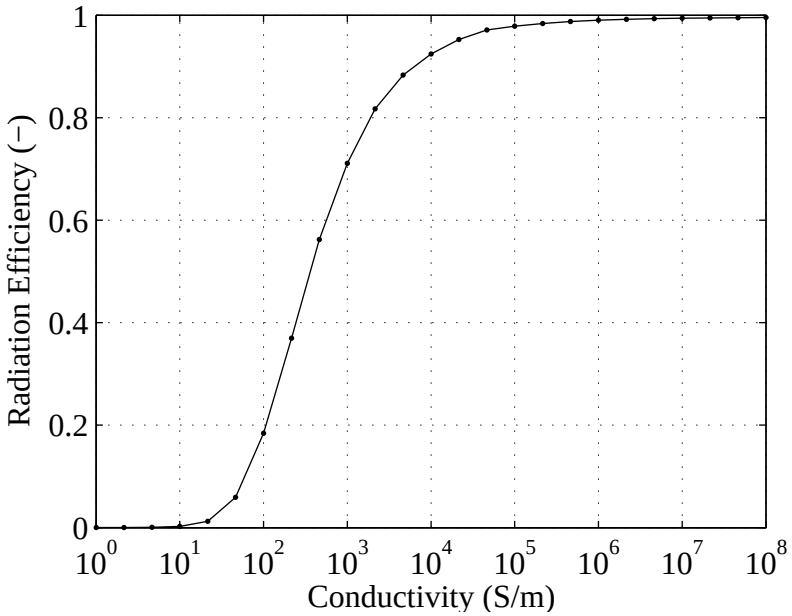

Figure 5.7: The radiation efficiency of the paper dipole antenna as a function of paper conductivity.

where D_0 is the maximum directivity of the antenna. It is evident that the maximum gain also decreases rapidly as R_{lo} increases. The value of D_0 is mildly impacted by R_{lo} in that its value can be related to $I(z)$. For example, a half-wavelength dipole with a sinusoidal current distribution exhibits a maximum directivity of approximately 2.15 dBi, whereas the maximum directivity of a short dipole with an approximately triangular current distribution is approximately 1.76 dBi [90].

Figure 5.8 shows a plot of both the maximum directivity and maximum gain associated with the antenna as the conductivity is varied. The directivity is constant at approximately +2.2 dBi above 100 S/m. Below 100 S/m the directivity decreases to approximately +1.7 dBi. This is expected given the curves shown in Figure 5.4, which indicate that the current distributions associated with these conductivities are better approximated as triangular rather than sinusoidal.

As expected, the antenna gain closely matches the directivity for high conductivities where the radiation efficiency is close to unity and at low conductivities it

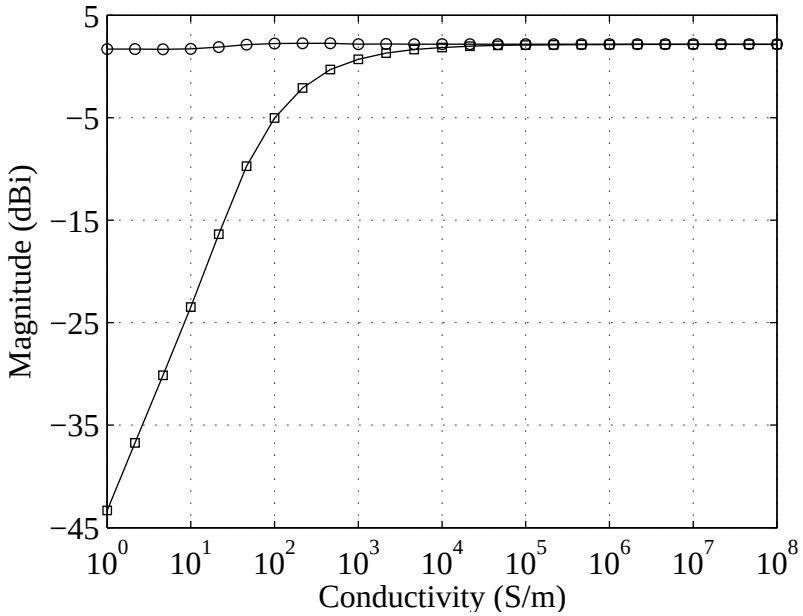

Figure 5.8: The maximum directivity and maximum gain of the paper dipole antenna as a function of paper conductivity. ∘: D_0 and □: G_0.

drops off considerably. For conductive paper at 50 S/m the gain of the antenna is approximately −9.7 dBi; a gain penalty of roughly 12 dB is incurred due to conductor losses. At 500 S/m the gain is approximately −0.2 dBi, which is slightly less than the gain of an isotropic radiator and may be acceptable in some applications.

For a dipole antenna where $l \leq \lambda$, the shape of the radiation pattern is directly related to D_0. Since conductor losses are expected to reduce the maximum directivity by less than 1 dB, the impact of reducing conductivity on the radiation pattern is also expected to be minor. Consequently, the full radiation pattern is not shown; however, the familiar omnidirectional pattern is observed [90], with a slight broadening at low conductivities corresponding to the associated reduction in directivity.

5.2.4 Application to UHF RFID

As mentioned in Section 2.2.1, the RFID read range is one of the most important tag performance metrics. Both the gain of the tag antenna and the associated

power transfer coefficient significantly impact this range. In order to assess the applicability of the conductive paper to UHF RFID tag design, the relative read range is defined as the ratio of the RFID read range associated with the use of a conductive-paper dipole antenna to that of a perfectly conjugate-matched tag constructed using a lossless isotropic radiator. Based on Equation 2.23, the RFID read range for this idealized isotropic radiator case, denoted by $r_{\mathrm{max,isotropic}}$, is given by

$$r_{\mathrm{max,isotropic}} = \frac{\lambda}{4\pi}\sqrt{\frac{P_{\mathrm{EIRP}}}{P_{\mathrm{min}}}}. \tag{5.11}$$

Consequently, the relative read range, r_{rel}, can be written as

$$r_{\mathrm{rel}} = \frac{r_{\mathrm{max}}}{r_{\mathrm{max,isotropic}}} = \sqrt{G_{0,\mathrm{tag}}\,\kappa}, \tag{5.12}$$

where in this case $G_{0,\mathrm{tag}}$ is simply equal to G_0.

The input impedance of a tag IC is dictated by the associated electronics and it is the responsibility of the antenna designer to ensure that power transmission from the tag antenna to the IC is optimized. Based on the results of Section 5.2.2, it is evident that this task becomes much more difficult as conductor losses increase; the input resistance is dominated by R_{loss} and X_{in} is always negative. However, it is assumed that a perfect conjugate match has been achieved via some ideal matching network, in which case $\kappa = 1$ and the relative read range is completely dictated by G_0. A plot of the relative read range as a function of conductivity is shown in Figure 5.9. For a conductivity of 50 S/m, r_{rel} is approximately 0.33. This would generally be considered poor in terms of RFID tag antenna performance [77], and translates to 25 % of the read range obtained using copper. At 500 S/m r_{rel} is approximately 0.97, which translates to 73 % of that obtained with copper and may be acceptable for some applications.

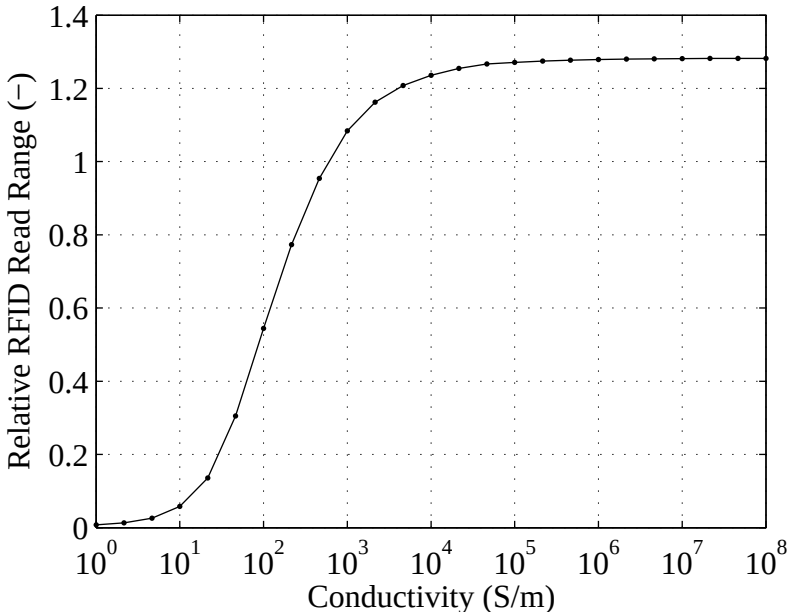

Figure 5.9: The relative RFID read range associated with a UHF RFID tag featuring a paper dipole antenna as a function of paper conductivity. It is assumed that $\kappa = 1$.

5.3 Experimental Results

While the results of Section 5.2 are valuable in terms of understanding the relationship between the paper conductivity and the key antenna properties, they must be validated experimentally. In order to achieve this, three additional antennas were constructed: a 1 mm thick paper antenna and two identical antennas built using copper tape of approximately 0.05 mm thickness. The construction details of these antennas were similar to those presented in Section 5.1.2 with the exception of conductor thickness and, in the case of the copper antennas, the feed wires were soldered to the conductors. The 1 mm thick paper and copper tape antennas were simulated and the gain results are shown in Table 5.1.

Figure 5.10 depicts the antenna gain measurement set-up. The antennas were mounted approximately 2 m apart inside the ATC and were polarization-aligned. The PNA was calibrated and used to measure the S-parameters of the set-up. In order to reduce reflection losses, the lengths of the copper antennas were trimmed until the

Table 5.1: Simulated and measured gain results for conductive-paper and copper antennas.

Antenna	G_0		
	Simulated (dBi)	Measured (dBi)	Error (dB)
Copper 1 (tape)	+2.1	+1.8	0.3
Copper 2 (tape)	+2.1	+1.7	0.4
Paper (0.4 mm)	−9.7	−11	1.3
Paper (1 mm)	−4.7	−6.6	1.9

magnitude of the input reactance was minimized at 915 MHz and the input VSWR was below 2:1. For the paper antennas, this was achieved using single-stub matching networks. The three antenna method [90] was executed in order to determine the gains of the two copper antennas and the 0.4 mm paper antenna. The gain of the 1 mm paper antenna was then measured using the substitution method. These results are also shown in Table 5.1.

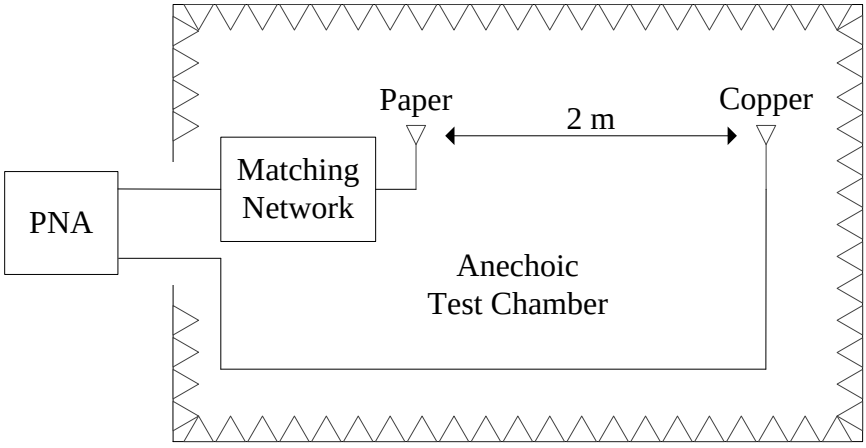

Figure 5.10: An illustration of the antenna gain measurement set-up.

Although the copper antennas are largely identical, the gain results differ by approximately 0.1 dB; this gives an indication of the error tolerance associated with the ATC measurements. Since the errors between the measured and simulated gains are less than 0.5 dB, the results appear to be in agreement; discrepancies could be

largely attributed to the insertion loss of the balun, which is stated to be as high as 1 dB.

For the conductive-paper antennas a higher degree of error is observed between simulations and measurements. The baluns are expected to be a more significant source of error for the paper antennas as they present a relatively poor impedance match on the balanced side. The aforementioned difficulties associated with mesh convergence in CST Microwave Studio® for low paper conductivities may also contribute some inaccuracy in the simulated paper gain results. Finally, the matching networks employed with the paper antennas are expected to contribute some additional loss. In any case, the measurements do show a significant performance improvement associated with increasing the thickness of the conductor, which is reflected in the simulated results.

Based on the measured gain of -11 dBi associated with the 0.4 mm paper antenna, the radiation efficiency is found to be 5.0 %. The corresponding relative RFID read range is 0.28, which is only 22 % of that obtained using copper.

5.4 Summary

Electrically conductive paper has been presented as an alternative antenna conductor to copper. Despite the low-cost and eco-friendly nature of conductive paper, the relatively low conductivity of 50 S/m is prohibitive to its application in wireless systems such as UHF RFID. Due to the lossy nature of the conductive paper, the current distribution along the antenna is diminished. Consequently, the radiation resistance is reduced and the loss resistance is greatly increased, resulting in a very inefficient radiator. In other words, an antenna constructed using conductive paper is shown to exhibit very low gain and therefore poor RFID read range performance. Simulations suggested a gain of -9.7 dBi when the conductivity is 50 S/m, which

corresponds to a relative RFID read range of 25 % of that achieved using copper. Measurements revealed even lower values: −11 dBi and 22 %, respectively. In addition, the resonance condition would not be achievable without the use of an external matching network, which may be undesirable.

A reasonable conductivity target for improved paper antenna performance was found to be 500 S/m. At this conductivity, the resonance condition could be met without external components, the current distribution would be roughly sinusoidal meaning the radiation resistance would have nearly reached its maximum value for the given geometry and the antenna gain would be just under 0 dBi. This would translate into an RFID read range of just below that obtained with an isotropic radiator. The most significant effect associated with improving the conductivity beyond this value would be a reduction in R_{lo} and, consequently, the loss resistance, thereby improving the overall efficiency of the radiator.

Chapter 6

Conclusion

Cellular base stations and WLAN APs employing MIMO are being installed closer together in order to meet the increasing wireless capacity demands. This motivates the investigation of in-room MIMO communication. Simulation results associated with improving in-room MIMO capacity using θ-directional AP antennas which emphasize wall-reflected NLOS components were presented in Chapter 3. It was found that performance improvements could be achieved depending on the directivity and main lobe θ-direction associated with the AP antennas. In general, the maximum room-averaged MIMO capacity was observed for main lobe θ-directions falling between those which maximized the room-averaged relative MIMO gain and received SNR results. Simultaneous improvements to both MIMO capacity and relative MIMO gain were obtained using AP antennas which were sufficiently directive to emphasize wall-reflected NLOS components without also emphasizing LOS components. The use of θ-directional AP antennas was shown to be most effective in larger rooms which tend to be LOS-dominated.

Chapter 4 detailed an experimental investigation of the in-room MIMO results obtained through simulation. MIMO channel measurements collected in an unoccupied classroom revealed a maximum improvement in the room-averaged MIMO

capacity of approximately 5 % when θ-directional AP antennas were used. For the same main-lobe θ-direction, a minor reduction in the room-averaged relative MIMO gain was observed. These results were compared to simulations in which the associated parameters were altered from those used in Chapter 3 to better match the measurement conditions. Although a reasonable agreement between the measured and simulated results was observed in terms of the qualitative behaviour of the associated performance metrics, the simulated results suggested a room-averaged MIMO capacity improvement on the order of 13 % coupled with a minor increase in the room-averaged relative MIMO gain. Therefore, the measured performance improvements were modest compared to those predicted through simulation. This is largely due to the increased multipath richness associated with the real environment relative to that exhibited by the idealized simulation environment. More significant improvements may be possible for in-room environments exhibiting less multipath richness.

Alternative antenna conductor materials have recently been investigated in an effort to reduce the cost of UHF RFID tags. An evaluation of the performance of dipole antennas constructed using conductive paper was presented in Chapter 5. The conductivity of a sample of the current paper technology was measured to be approximately 50 S/m. Through both simulations and experimental measurements, this was found to be prohibitively low in the context of antenna design. For example, gain results associated with a conductive-paper dipole antenna were found to be -9.7 dBi and -11 dBi through simulation and measurement, respectively. The performance of the dipole as a function of paper conductivity was characterized via simulation. This revealed a target conductivity of 500 S/m at which the properties of the resulting antenna more closely resemble those of a copper antenna. The associated gain would be close to 0 dBi in this case, making the antenna far more applicable to UHF RFID systems.

6.1 Future Work

There remain several avenues to explore in the context of improving in-room MIMO capacity using θ-directional AP antennas. For example, the simulations assumed that for $M > 2$ the MIMO antennas were arranged in UCAs. This may not be possible in practice, especially at the PD. Consequently, the impact of changing the antenna configurations and orientations on the resulting performance improvements could be explored. The effect of using more practical performance metrics such as mean squared error (MSE) and BER could also be examined. In addition, the simulation software could be altered such that the locations, orientations, directivities and main lobe directions associated with AP antennas could be optimized using an evolutionary algorithm.

The in-room MIMO measurements were obtained in a particular room and for a very specific set of conditions. Since the measured results in the 2.4 GHz ISM band suggested that the multipath exhibited by the room was relatively dense, it would be interesting to perform the measurements in a higher frequency band. In this case, the MIMO channels are expected to be more LOS-dominated and, as result, the corresponding improvements associated with the application of θ-directional AP antennas may be more significant. Performing measurements in a variety of rooms with different geometries and construction materials would also add practical insight into the resulting performance improvements.

Many opportunities for additional contributions also exist in the context of developing conductive-paper UHF RFID tag antennas. Once paper exhibiting a conductivity on the order of 500 S/m can be produced, the associated performance predictions found in Chapter 5 should be verified experimentally. If the results are acceptable, the practical considerations associated with designing a conductive-paper tag antenna must be addressed. For example, the nature of the interface between the paper antenna and the tag IC must be developed. An investigation of more complex

antenna designs such as meander-line dipoles may be required. The behaviour of such antennas as a function of paper conductivity would also have to be characterized. Once a functional conductive-paper UHF RFID tag has been developed, RFID read range measurements conducted in the ATC would provide a final assessment of their feasibility.

Bibliography

[1] A. Bleicher, "A surge in small cells," *IEEE Spectrum*, vol. 50, no. 1, pp. 38–39, Jan. 2013.

[2] A. Knopp, M. Chouayakh, R. Schwarz, and B. Lankl, "Measured MIMO capacity enhancement in correlated LOS indoor channels via optimized antenna setups," in *International Conference on Wireless Information Networks and Systems*, Setúbal, Portugal, Aug. 7–10 2006, pp. 187–193.

[3] A. Knopp, M. Chouayakh, and B. Lankl, "MIMO-capacities for broadband in-room quasi-deterministic line-of-sight radio channels derived from measurements," in *IEEE 17th International Symposium on Personal, Indoor and Mobile Radio Communication*, Helsinki, Finland, Sept. 11–14 2006, pp. 1–7.

[4] M. Nebel, A. Knopp, and B. Lankl, "Spatial capacity optimization for indoor MIMO LOS channels applying methods of high-rank transfer matrix construction," in *IEEE 18th International Symposium on Personal, Indoor and Mobile Radio Communication*, Athens, Greece, Sept. 3–7 2007, pp. 1–5.

[5] C. H. Y. Eugene, K. Sakaguchi, and K. Araki, "Experimental and analytical investigation of MIMO channel capacity in an indoor line-of-sight environment," in *IEEE 15th International Symposium on Personal, Indoor and Mobile Radio Communication*, vol. 1, Barcelona, Spain, Sept. 5–8 2004, pp. 295–300.

[6] P. L. Kafle, A. Intarapanich, A. B. Sesay, J. McRory, and R. J. Davies, "Spatial correlation and capacity measurements for wideband MIMO channels in indoor office environment," *IEEE Transactions on Wireless Communications*, vol. 7, no. 5, pp. 1560–1571, May 2008.

[7] J.-P. Curty, M. Declercq, C. Dehollain, and N. Joehl, *Design and Optimization of Passive UHF RFID Systems*. New York, New York: Springer Science+Business Media, LLC, 2007.

[8] P. V. Nikitin, S. Lam, and K. V. S. Rao, "Low cost silver ink RFID tag antennas," in *IEEE Antennas and Propagation Society International Symposium*, vol. 2B, Washington, District of Columbia, July 2005, pp. 353–356.

[9] A. Mehdipour, C. W. Trueman, A. R. Sebak, and S. V. Hoa, "Carbon-fiber composite T-match folded bow-tie antenna for RFID applications," in *IEEE Antennas and Propagation Society International Symposium*, Charleston, South Carolina, June 2009, pp. 1–4.

[10] B. Huang, G. Kang, and Y. Ni, "Electrically conductive fibre composites prepared from polypyrrole-engineered pulp fibres," *The Canadian Journal of Chemical Engineering*, vol. 83, no. 5, pp. 896–903, Oct. 2005.

[11] B. Huang, G. J. Kang, and Y. Ni, "Preparation of conductive paper by in-situ polymerization of pyrrole in a pulp fibre system," *Pulp & Paper Canada*, vol. 107, no. 2, pp. 38–42, 2006.

[12] C. C. Martin, J. H. Winters, and N. R. Sollenberger, "MIMO radio channel measurements: performance comparison of antenna configurations," in *IEEE 54th Vehicular Technology Conference*, vol. 2, Atlantic City, New Jersey, Oct. 7–11 2001, pp. 1225–1229.

[13] K. Sulonen, P. Suvikunnas, L. Vuokko, J. Kivinen, and P. Vainikainen, "Comparison of MIMO antenna configurations in picocell and microcell environments," *IEEE Journal on Selected Areas in Communications*, vol. 21, no. 5, pp. 703–712, June 2003.

[14] M. Elnaggar, S. Safavi-Naeini, and S. K. Chaudhuri, "Simulation of the achievable indoor MIMO capacity by using an adaptive phased-array," in *IEEE Radio and Wireless Symposium*, Atlanta, Georgia, Sept. 19–22 2004, pp. 155–158.

[15] A. Forenza and R. W. Heath, "Impact of antenna geometry on MIMO communication in indoor clustered channels," in *IEEE Antennas and Propagation Society International Symposium*, vol. 2, Monterey, California, June 20–25 2004, pp. 1700–1703.

[16] M. Blanco, R. Kokku, K. Ramachandran, S. Rangarajan, and K. Sundaresan, "On the effectiveness of switched beam antennas in indoor environments," in *Proceedings of the 9th International Conference on Passive and Active Network Measurement*, Cleveland, Ohio, Apr. 29–30 2008, pp. 122–131.

[17] C. Hermosilla, R. Feick, R. A. Valenzuela, and L. Ahumada, "Improving MIMO capacity with directive antennas for outdoor-indoor scenarios," *IEEE Transactions on Wireless Communications*, vol. 8, no. 5, pp. 2177–2181, May 2009.

[18] C. D. Rouse, M. R. Kurz, B. R. Petersen, and B. G. Colpitts, "Performance evaluation of conductive-paper dipole antennas," *IEEE Transactions on Antennas and Propagation*, vol. 61, no. 3, pp. 1427–1430, Mar. 2013.

[19] C. E. Shannon, "A mathematical theory of communication," *The Bell System Technical Journal*, vol. 27, pp. 379–423, 623–656, Oct. 1948.

[20] A. Goldsmith, *Wireless Communications*. New York, NY: Cambridge University Press, 2005.

[21] G. J. Foschini and M. J. Gans, "On limits of wireless communications in a fading environment when using multiple antennas," *Wireless Personal Communications*, vol. 6, pp. 311–335, Mar. 1998.

[22] A. F. Molisch, M. Steinbauer, M. Toeltsch, E. Bonek, and R. S. Thomä, "Capacity of MIMO systems based on measured wireless channels," *IEEE Journal on Selected Areas in Communications*, vol. 20, no. 3, pp. 561–569, Apr. 2002.

[23] R. Stridh, K. Yu, B. Ottersten, and P. Karlsson, "MIMO channel capacity and modeling issues on a measured indoor radio channel at 5.8 GHz," *IEEE Transactions on Wireless Communications*, vol. 4, no. 3, pp. 895–903, May 2005.

[24] W. C. Jakes, *Microwave Mobile Communications*, W. Perkins, Ed. Pisctataway, New Jersey: IEEE Press, 1993.

[25] R. H. Clarke, "A statistical theory of mobile radio reception," *The Bell System Technical Journal*, vol. 47, no. 6, pp. 957–1000, July/Aug. 1968.

[26] W. C. Y. Lee, "Antenna spacing requirement for a mobile radio base-station diversity," *The Bell System Technical Journal*, vol. 50, no. 6, pp. 1859–1876, July/Aug. 1971.

[27] J. H. Winters, "Optimum combining in digital mobile radio with cochannel interference," *IEEE Journal on Selected Areas in Communications*, vol. SAC-2, no. 4, pp. 528–539, July 1984.

[28] S. M. Alamouti, "A simple transmit diversity technique for wireless communications," *IEEE Journal on Selected Areas in Communications*, vol. 16, no. 8, pp. 1451–1458, Oct. 1998.

[29] B. Vucetic and J. Yuan, *Space-Time Coding*. Hoboken, New Jersey: John Wiley & Sons Ltd., 2003, vol. 1.

[30] L. Zheng and D. N. C. Tse, "Diversity and multiplexing: A fundamental tradeoff in multiple-antenna channels," *IEEE Transactions on Information Theory*, vol. 49, no. 5, pp. 1073–1096, May 2003.

[31] E. Telatar, "Capacity of multi-antenna Gaussian channels," AT&T Bell Laboratories, Internal Technical Memorandum, June 1995.

[32] M. T. Heath, *Scientific Computing: An Introductory Survey*, C. L. Liu, Ed. New York, NY: The McGraw-Hill Companies, Inc., 1997.

[33] M. A. Jensen and J. W. Wallace, "A review of antennas and propagation for MIMO wireless communications," *IEEE Transactions on Antennas and Propagation*, vol. 52, no. 11, pp. 2810–2824, Nov. 2004.

[34] D. Gesbert, H. Bölcskei, D. Gore, and A. Paulraj, "MIMO wireless channels: Capacity and performance prediction," in *IEEE Global Telecommunications Conference*, vol. 2, San Francisco, California, Nov. 2000, pp. 1083–1088.

[35] A. Goldsmith, S. A. Jafar, N. Jindal, and S. Vishwanath, "Capacity limits of MIMO channels," *IEEE Journal on Selected Areas in Communications*, vol. 21, no. 5, pp. 684–702, 2003.

[36] J. H. Winters, "Optimum combining for indoor radio systems with multiple users," *IEEE Transactions on Communications*, vol. COM-35, no. 11, pp. 1222–1230, Nov. 1987.

[37] E. Telatar, "Capacity of multi-antenna gaussian channels," *European Transactions on Telecommunications*, vol. 10, no. 6, pp. 585–595, Dec. 1999.

[38] G. G. Raleigh and J. M. Cioffi, "Spatio-temporal coding for wireless communication," *IEEE Transactions on Communications*, vol. 46, no. 3, pp. 357–366, Mar. 1998.

[39] D. Gesbert, M. Shafi, D.-S. Shiu, P. J. Smith, and A. Naguib, "From theory to practice: An overview of MIMO space-time coded wireless systems," *IEEE Journal on Selected Areas in Communications*, vol. 21, no. 3, pp. 281–302, Apr. 2003.

[40] D.-S. Shiu, G. J. Foschini, M. J. Gans, and J. M. Kahn, "Fading correlation and its effect on the capacity of multielement antenna systems," *IEEE Transactions on Communications*, vol. 48, no. 3, pp. 502–513, Mar. 2000.

[41] M. Chiani, M. Z. Win, and A. Zanella, "On the capacity of spatially correlated MIMO Rayleigh-fading channels," *IEEE Transactions on Information Theory*, vol. 49, no. 10, pp. 2363–2371, Oct. 2003.

[42] T. Svantesson and A. Ranheim, "Mutual coupling effects on the capacity of multielement antenna systems," in *IEEE International Conference on Acoustics, Speech and Signal Processing*, vol. 4, Salt Lake City, Utah, May 7–11 2001, pp. 2485–2488.

[43] J. W. Wallace and M. A. Jensen, "Mutual coupling in MIMO wireless systems: A rigorous network theory analysis," *IEEE Transactions on Wireless Communications*, vol. 3, no. 4, pp. 1317–1325, July 2004.

[44] D. Chizhik, G. J. Foschini, and R. A. Valenzuela, "Capacities of multi-element transmit and receive antennas: Correlations and keyholes," *Electronics Letters*, vol. 36, no. 13, pp. 1099–1100, June 2000.

[45] D. Chizhik, G. J. Foschini, M. J. Gans, and R. A. Valenzuela, "Keyholes, correlations, and capacities of multielement transmit and receive antennas," *IEEE Transactions on Wireless Communications*, vol. 1, no. 2, pp. 361–368, Apr. 2002.

[46] P. Almers, F. Tufvesson, and A. F. Molisch, "Keyhole effect in MIMO wireless channels: Measurements and theory," *IEEE Transactions on Wireless Communications*, vol. 5, no. 12, pp. 3596–3604, Dec. 2006.

[47] R. W. Heath, S. Sandhu, and A. Paulraj, "Antenna selection for spatial multiplexing systems with linear receivers," *IEEE Communications Letters*, vol. 5, no. 4, pp. 142–144, Apr. 2001.

[48] D. A. Gore and A. J. Paulraj, "MIMO antenna subset selection with space-time coding," *IEEE Transactions on Signal Processing*, vol. 50, no. 10, pp. 2580–2588, Oct. 2002.

[49] H. Bölcskei, D. Gesbert, and A. J. Paulraj, "On the capacity of OFDM-based spatial multiplexing systems," *IEEE Transactions on Communications*, vol. 50, no. 2, pp. 225–234, Feb. 2002.

[50] G. J. Foschini, "Layered space-time architecture for wireless communication in a fading environment when using multi-element antennas," *Bell Labs Technical Journal*, vol. 1, no. 2, pp. 41–59, Autumn 1996.

[51] G. J. Foschini, G. D. Golden, R. A. Valenzuela, and P. W. Wolniansky, "Simplified processing for high spectral efficiency wireless communication employing multi-element arrays," *IEEE Journal on Selected Areas in Communications*, vol. 17, no. 11, pp. 1841–1852, Nov. 1999.

[52] A. Lozano and C. Papadias, "Layered space-time receivers for frequency-selective wireless channels," *IEEE Transactions on Communications*, vol. 50, no. 1, pp. 65–73, Jan. 2002.

[53] M. J. Gans, N. Amitay, Y. S. Yeh, H. Xu, T. C. Damen, R. A. Valenzuela, T. Sizer, R. Storz, D. Taylor, W. M. MacDonald, C. Tran, and A. Adamiecki, "Outdoor BLAST measurement system at 2.44 GHz: Calibration and initial

results," *IEEE Journal on Selected Areas in Communications*, vol. 20, no. 3, pp. 570–583, Apr. 2002.

[54] D. N. C. Tse, P. Viswanath, and L. Zheng, "Diversity-multiplexing tradeoff in multiple-access channels," *IEEE Transactions on Information Theory*, vol. 50, no. 9, pp. 1859–1874, Sept. 2004.

[55] R. B. Ertel, P. Cardieri, K. W. Sowerby, T. S. Rappaport, and J. H. Reed, "Overview of spatial channel models for antenna array communication systems," *IEEE Personal Communications Magazine*, vol. 5, no. 1, pp. 10–22, Feb. 1998.

[56] F. Bøhagen, P. Orten, and G. E. Øien, "Design of optimal high-rank line-of-sight MIMO channels," *IEEE Transactions on Wireless Communications*, vol. 6, no. 4, pp. 1420–1425, Apr. 2007.

[57] L. Liu, W. Hong, H. Wang, G. Yang, N. Zhang, H. Zhao, J. Chang, C. Yu, X. Yu, H. Tang, H. Zhu, and L. Tian, "Characterization of line-of-sight MIMO channel for fixed wireless communications," *IEEE Antennas and Wireless Propagation Letters*, vol. 6, pp. 36–39, 2007.

[58] I. Sarris and A. R. Nix, "Design and performance assessment of high-capacity MIMO architectures in the presence of a line-of-sight component," *IEEE Transactions on Vehicular Technology*, vol. 56, no. 4, pp. 2194–2202, July 2007.

[59] B. T. Walkenhorst, T. G. Pratt, and M. A. Ingram, "Improving MIMO capacity in a line-of-sight environment," in *IEEE 50th Global Telecommunications Conference*, Washington, District of Columbia, Nov. 26–30 2007, pp. 3623–3628.

[60] J. Shen, Y. Oda, T. Furuno, T. Maruyama, and T. Ohya, "A novel approach for capacity improvement of 2×2 MIMO in LOS channel using reflectarray," in

IEEE 73rd Vehicular Technology Conference, Budapest, Hungary, May 15–18 2011, pp. 1–5.

[61] P. F. Driessen and G. J. Foschini, "On the capacity formula for multiple input-multiple output wireless channels: A geometric interpretation," *IEEE Transactions on Communications*, vol. 47, no. 2, pp. 173–176, Feb. 1999.

[62] A. A. Hutter, G. Platbrood, and J. Ayadi, "Analysis of MIMO capacity gains for indoor propagation channels with LOS component," in *IEEE 13th International Symposium on Personal, Indoor and Mobile Radio Communication*, vol. 3, Lisbon, Portugal, Sept. 15–18 2002, pp. 1337–1341.

[63] T. Haustein and U. Krüger, "Smart geometrical antenna design exploiting the LOS component to enhance a MIMO system based on Rayleigh-fading in indoor scenarios," in *IEEE 14th International Symposium on Personal, Indoor and Mobile Radio Communication*, Beijing, China, Sept. 7–10 2003, pp. 1144–1148.

[64] J. Lv, Y. Lu, Y. Wang, H. Zhao, and C. Y. Han, "Antenna spacing effect on indoor MIMO channel capacity," in *Asia Pacific Microwave Conference Proceedings*, vol. 3, Suzhou, China, Dec. 4–7 2005.

[65] M. L. Morris and M. A. Jensen, "The impact of array configuration on MIMO wireless channel capacity," in *IEEE Antennas and Propagation Society International Symposium*, vol. 3, San Antonio, Texas, June 16–21 2002, pp. 214–217.

[66] L. Xiao, L. Dal, H. Zhuang, S. Zhou, and Y. Yao, "A comparative study of MIMO capacity with different antenna topologies," in *The 8th International Conference on Communication Systems*, vol. 1, Singapore, Nov. 25–28 2002, pp. 431–435.

[67] H.-C. Lo, D.-B. Lin, T.-C. Yang, and H.-J. Li, "Effect of polarization on the correlation and capacity of indoor MIMO channels," *International Journal of Antennas and Propagation*, vol. 2012, pp. 1–11, 2012.

[68] D. Gesbert, H. Bölcskei, D. A. Gore, and A. J. Paulraj, "Outdoor MIMO wireless channels: Models and performance prediction," *IEEE Transactions on Communications*, vol. 50, no. 12, pp. 1926–1934, Dec. 2002.

[69] Z. Tang and A. S. Mohan, "Experimental investigation of indoor MIMO Ricean channel capacity," *IEEE Antennas and Wireless Propagation Letters*, vol. 4, pp. 55–58, 2005.

[70] Q. Li, G. Li, W. Lee, M.-I. Lee, D. Mazzarese, B. Clerckx, and Z. Li, "MIMO techniques in WiMAX and LTE: a feature overview," *IEEE Communications Magazine*, vol. 48, no. 5, pp. 86–92, May 2010.

[71] G. Zhu, "On the signalling length in digital wireless communications," Master's thesis, University of New Brunswick, 2005.

[72] V. V. S. N. Polu, "Receiver antenna separation over symbol wavelengths in a MIMO-multiuser UWB system with near LOS channels," Master's thesis, University of New Brunswick, Jan. 2007.

[73] T. Kaiser, F. Zheng, and E. Dimitrov, "An overview of ultra-wide-band systems with MIMO," *Proceedings of the IEEE*, vol. 97, no. 2, pp. 285–312, Feb. 2009.

[74] K. Finkenzeller, *RFID Handbook: fundamentals and applications in contactless smart cards and identification*, 2nd ed. Hoboken, New Jersey: John Wiley & Sons Inc., 2003.

[75] G. Marrocco, "The art of UHF RFID antenna design: impedance-matching and size-reduction techniques," *IEEE Antennas and Propagation Magazine*, vol. 50, no. 1, pp. 66–79, Feb. 2008.

[76] R. Glidden, C. Bockorick, S. Cooper, C. Diorio, D. Dressler, V. Gutnik, C. Hagen, D. Hara, T. Hass, T. Humes, J. Hyde, R. Oliver, O. Onen, A. Pesavento, K. Sundstrom, and M. Thomas, "Design of ultra-low-cost UHF RFlD tags for supply chain applications," *IEEE Communications Magazine*, vol. 42, no. 8, pp. 140–151, Aug. 2004.

[77] K. V. S. Rao, P. V. Nikitin, and S. F. Lam, "Antenna design for UHF RFID tags: A review and a practical application," *IEEE Transactions on Antennas and Propagation*, vol. 53, no. 12, pp. 3870–3876, Dec. 2005.

[78] P. V. Nikitin and K. V. S. Rao, "Theory and measurement of backscattering from RFID tags," *IEEE Antennas and Propagation Magazine*, vol. 48, no. 6, pp. 212–218, Mar. 2006.

[79] T. Umeda, H. Yoshida, S. Sekine, Y. Fujita, T. Suzuki, and S. Otaka, "A 950-MHz rectifier circuit for sensor network tags with 10-m distance," *IEEE Journal of Solid-State Circuits*, vol. 41, no. 1, pp. 35–41, Jan. 2006.

[80] D. Kuester and Z. Popovic, "How good is your tag?: RFID backscatter metrics and measurements," *IEEE Microwave Magazine*, vol. 14, no. 5, pp. 47–55, July–Aug. 2013.

[81] H. Stockman, "Communication by means of reflected power," *Proceedings of the I.R.E.*, vol. 36, no. 10, pp. 1196–1204, Oct. 1948.

[82] R. F. Harrington, "Theory of loaded scatterers," *Proceedings of the IEEE*, vol. 111, no. 4, pp. 617–623, April 1964.

[83] A. R. Koelle, S. W. Depp, and R. W. Freyman, "Short-range radio-telemetry for electronic identification, using modulated RF backscatter," *Proceedings of the IEEE*, vol. 63, no. 8, pp. 1260–1261, Aug. 1975.

[84] J. Landt, "The history of RFID," *IEEE Potentials*, vol. 24, no. 4, pp. 8–11, Oct.–Nov. 2005.

[85] U. Karthaus and M. Fischer, "Fully integrated passive UHF RFID transponder IC with 16.7-μW minimum RF input power," *IEEE Journal of Solid-State Circuits*, vol. 38, no. 10, pp. 1602–1608, Oct. 2003.

[86] J.-P. Curty, N. Joehl, C. Dehollain, and M. J. Declercq, "Remotely powered addressable UHF RFID integrated system," *IEEE Journal of Solid-State Circuits*, vol. 40, no. 11, pp. 2193–2202, Nov. 2005.

[87] H. Nakamoto, D. Yamazaki, T. Yamamoto, H. Kurata, S. Yamada, K. Mukaida, T. Ninomiya, T. Ohkawa, S. Masui, and K. Gotoh, "A passive UHF RF identification CMOS tag IC using ferroelectric RAM in 0.35-μm technology," *IEEE Journal of Solid-State Circuits*, vol. 42, no. 1, pp. 101–110, Jan. 2007.

[88] T. Svantesson and J. Wallace, "On signal strength and multipath richness in multi-input multi-output systems," in *IEEE International Conference on Communications*, vol. 4, Anchorage, Arkansas, May 11–15 2003, pp. 2683–2687.

[89] D. W. Browne, J. Guterman, M. P. Fitz, and Y. Rahmat-Samii, "Expermental validation of capacity preserving design for MIMO arrays," in *International Workshop on Antenna Technology*, Cambridge, United Kingdom, Mar. 21–23 2007, pp. 203–206.

[90] C. A. Balanis, *Antenna Theory: Analysis and Design*, 3rd ed. Hoboken, New Jersey: John Wiley & Sons Inc., 2005.

[91] M. Elnaggar, S. Safavi-Naeini, and S. K. Chaudhuri, "Simulation and maximum capacity verification of indoor MIMO antenna systems in a simple multipath-rich environment," in *IEEE Antennas and Propagagation Society International Symposium*, vol. 2, Columbus, Ohio, June 22–27 2003, pp. 527–530.

[92] D. H. Werner, "An exact integration procedure for vector potentials of thin circular loop antennas," *IEEE Transactions on Antennas and Propagation*, vol. 44, no. 2, pp. 157–165, Feb. 1996.

[93] J. D. Kraus, *Antennas*, 2nd ed. New York, New York: McGraw-Hill, Inc., 1988.

[94] H. Yordanov, P. Russer, M. T. Ivrlač, and J. A. Nossek, "Arrays of isotropic radiators—a field-theoretic justification," in *Proceedings of the IEEE/ITG International Workshop on Smart Antennas*, Berlin, FR Germany, Feb. 16–18 2009.

[95] R. Valenzuela, "A ray tracing approach to predicting indoor wireless transmission," in *IEEE 43rd Vehicular Technology Conference*, Secaucus, New Jersey, May 18–20 1993, pp. 214–218.

[96] K. A. Remley, H. R. Anderson, and A. Weisshar, "Improving the accuracy of ray-tracing techniques for indoor propagation modeling," *IEEE Transactions on Vehicular Technology*, vol. 49, no. 6, pp. 2350–2358, Nov. 2000.

[97] A. S. Glassner, Ed., *An Introduction to Ray Tracing*. San Diego, California: Academic Press Limited, 1989.

[98] K. R. Schaubach, N. J. Davis IV, and T. S. Rappaport, "A ray tracing method for predicting path loss and delay spread in microcellular environments," in *IEEE 42nd Vehicular Technology Conference*, vol. 2, Denver, Colorado, May 1992, pp. 932–935.

[99] J.-S. Jiang and M. A. Ingram, "Spherical-wave model for short-range MIMO," *IEEE Transactions on Communications*, vol. 53, no. 9, pp. 1534–1541, Sept. 2005.

[100] M. N. O. Sadiku, *Elements of Electromagnetics*, 4th ed. New York, New York: Oxford University Press, Inc., 2007.

[101] H. Goldstein, *Classical Mechanics*, 2nd ed. Reading, Massachusetts: Addison-Wesley Publishing Company, Inc., 1980.

[102] B. W. M. Kuipers and L. M. Correia, "Modelling the relative MIMO gain," in *IEEE 19th International Symposium on Personal, Indoor and Mobile Radio Communication*, Cannes, France, Sept. 13–16 2008, pp. 1–5.

[103] B. T. Walkenhorst, "Achieving near-optimal MIMO capacity in a rank-deficient LOS environment," Ph.D. dissertation, Georgia Institute of Technology, Aug. 2009.

[104] D. M. Pozar, *Microwave Engineering*, 3rd ed. Hoboken, New Jersey: John Wiley & Sons Inc., 2005.

[105] I. Cuiñas, J.-P. Pugliese, A. Hammoudeh, and M. G. Sánchez, "Frequency dependence of dielectric constant of construction materials in microwave and millimeter-wave bands," *Microwave and Optical Technology Letters*, vol. 30, no. 2, pp. 123–124, July 2001.

[106] B. De Backer, H. Börjeson, D. De Zutter, and F. Olyslager, "Propagation mechanisms for UHF wave transmission through walls and windows," *IEEE Transactions on Vehicular Technology*, vol. 52, no. 5, pp. 1297–1307, Sept. 2003.

[107] D. Porrat and D. C. Cox, "UHF propagation in indoor hallways," *IEEE Transactions on Wireless Communications*, vol. 3, no. 4, pp. 1188–1198, July 2004.

[108] G. Chouinard, "RF sensing in the TV white space," in *8th Annual Communication and Networks and Services Research Conference*, Montreal, Canada, May 11–14 2010, pp. 8–14.

[109] H.-R. Chuang and L.-C. Kuo, "3-D FDTD design analysis of a 2.4-GHz polarization-diversity printed dipole antenna with integrated balun and polarization-switching circuit for WLAN and wireless communication applications," *IEEE Transactions on Microwave Theory and Techniques*, vol. 51, no. 2, pp. 374–381, Feb. 2003.

[110] M. Gustafsson and A. Karlsson, "Design of frequency selective windows for improved indoor outdoor communication," *IEEE Transactions on Antennas and Propagation*, vol. 54, no. 6, pp. 1897–1900, June 2006.

[111] G. J. M. Janssen, P. A. Stigter, and R. Prasad, "Wideband indoor channel measurements and BER analysis of frequency selective multipath channels at 2.4, 4.75, and 11.5 GHz," *IEEE Transactions on Communications*, vol. 44, no. 10, pp. 1272–1288, Oct. 1996.

[112] E. Torkildson, U. Madhow, and M. Rodwell, "Indoor millimeter wave MIMO: Feasibility and performance," *IEEE Transactions on Wireless Communications*, vol. 10, no. 12, pp. 4150–4160, Dec. 2011.

[113] L. Yang, A. Rida, R. Vyas, and M. M. Tentzeris, "RFID tag and RF structures on a paper substrate using inkjet-printing technology," *IEEE Transactions on Microwave Theory and Techniques*, vol. 55, no. 12, pp. 2894–2901, Dec. 2007.

[114] S. L. Merilampi, T. Björninen, A. Vuorimäki, L. Ukkonen, P. Ruuskanen, and L. Sydänheimo, "The effect of conductive ink layer thickness on the functioning of printed UHF RFID antennas," *Proceedings of the IEEE*, vol. 98, no. 9, pp. 1610–1619, Sept. 2010.

[115] A. Galehdar, P. J. Callus, and K. Ghorbani, "A novel method of conductivity measurements for carbon-fiber monopole antenna," *IEEE Transactions on Antennas and Propagation*, vol. 59, no. 6, pp. 2120–2126, June 2011.

[116] L. J. van der Pauw, "A method of measuring specific resistivity and hall effect of discs of arbitrary shape," *Philips Research Reports*, vol. 13, no. 1, pp. 1–9, Feb. 1958.

[117] R. W. P. King and T. T. Wu, "The imperfectly conducting cylindrical transmitting antenna," *IEEE Transactions on Antennas and Propagation*, vol. AP-14, no. 5, pp. 524–534, Sept. 1966.

[118] B. D. Popović and Z. D. Popović, "Imperfectly conducting cylindrical antenna: Variational approach," *IEEE Transactions on Antennas and Propagation*, vol. AP-19, no. 3, pp. 435–436, May 1971.

[119] R. W. P. King, C. W. Harrison, Jr., and E. A. Aronson, "The imperfectly conducting cylindrical transmitting antenna: Numerical results," *IEEE Transactions on Antennas and Propagation*, vol. AP-14, no. 5, pp. 535–541, Sept. 1966.

[120] P. D. Patel, "Semiconductor dipole: possible radiating element for microwave/millimetre-wave monolithic integrated circuits (MMICs)," *IEE Proceedings, Pt. H*, vol. 136, no. 6, pp. 455–461, Dec. 1989.

[121] G. W. Hanson, "Fundamental transmitting properties of carbon nanotube antennas," *IEEE Transactions on Antennas and Propagation*, vol. 53, no. 11, pp. 3426–3435, Nov. 2005.

[122] H. W. Ott, *Electromagnetic Compatibility Engineering*. Hoboken, New Jersey: John Wiley & Sons Inc., 2009.

[123] R. G. FitzGerrell, "Radiation efficiencies of half-wave dipole antennas," *IEEE Transactions on Antennas and Propagation*, vol. 13, no. 2, pp. 326–327, Mar. 1965.

[124] R. King and C. W. Harrison, "The distribution of current along a symmetrical center-driven antenna," *Proceedings of the I.R.E.*, vol. 31, no. 10, pp. 548–567, Oct. 1943.

[125] S. A. Schelkunoff and H. T. Friis, *Antennas: Theory and Practice.* New York: John Wiley & Sons Inc., 1952.

[126] L. J. van der Pauw, "A method of measuring the resistivity and hall coefficient on lamellae of arbitrary shape," *Philips Technical Review*, vol. 20, no. 8, pp. 220–224, 1958/59.

[127] L. V. Bewley, *Two-Dimensional Fields in Electrical Engineering.* New York, New York: Dover Publications, Inc., 1963.

Appendix A

MATLAB® Code for In-room MIMO Modelling

```
% The following code can be used to generate Figure 3.11 in the
% dissertation.  The "matlabpool" command can be used on multicore
% machines to reduce simulation times.  NOTE: If loops are to be used,
% the phased array element spacing and element orientation MUST be left
% at their default values, otherwise the mutual coupling calculations
% will be invalid.

clear;
clc;

simulationOptions = NewSimulationOptions();

wavelength = (3 * 10 ^8) / simulationOptions.centreFrequency;
theta_0 = (90:2.5:180)';
numPhasingAngles = length(theta_0);
N = [2,4,8];
M = 3;

simulationOptions.roomWidth = 8;
simulationOptions.roomLength = 8;
simulationOptions.roomHeight = 3;
simulationOptions.wallRelativePermittivity = 4;
simulationOptions.numReflections = 2;
simulationOptions.numEvaluationPointsPerSide = 30;

simulationOptions.accessPointAntennaType = AntennaType.Isotropic;
simulationOptions.accessPointAntennaSpacing = 2 * wavelength;
simulationOptions.accessPointArrayDistanceBelowCeiling = 2 * wavelength;
```

```
simulationOptions.mobileAntennaType = AntennaType.Isotropic;
simulationOptions.mobileAntennaSpacing =  0.5 * wavelength;

simulationOptions.numAccessPointAntennas = 1;
simulationOptions.numMobileAntennas = 1;

accessPointArray = BuildAccessPointArray(simulationOptions);
[SISOCapacities, SISOSNRs] = EvaluateRoomCapacity(accessPointArray,
   simulationOptions);

simulationOptions.numAccessPointAntennas = M;
simulationOptions.numMobileAntennas = M;

accessPointArray = BuildAccessPointArray(simulationOptions);
[MIMOCapacities, MIMOSNRs] = EvaluateRoomCapacity(accessPointArray,
   simulationOptions);

meanSISOCapacity = mean(reshape(SISOCapacities, simulationOptions.
   numEvaluationPointsPerSide^2, 1));
meanSISOSNRdB = mean(10*log10(reshape(SISOSNRs, simulationOptions.
   numEvaluationPointsPerSide^2, 1)));
meanMIMOCapacity = mean(reshape(MIMOCapacities, simulationOptions.
   numEvaluationPointsPerSide^2, 1));
meanMIMOSNRdB = mean(10*log10(reshape(MIMOSNRs, simulationOptions.
   numEvaluationPointsPerSide^2, 1)));

simulationOptions.phasedArrays = true;

PASISOCapacities = cell(numPhasingAngles, length(N));
PASISOSNRs = cell(numPhasingAngles, length(N));
PAMIMOCapacities = cell(numPhasingAngles, length(N));
PAMIMOSNRs = cell(numPhasingAngles, length(N));

meanPASISOCapacity = zeros(numPhasingAngles, length(N));
meanPASISOSNRdB = zeros(numPhasingAngles, length(N));
meanPAMIMOCapacity = zeros(numPhasingAngles, length(N));
meanPAMIMOSNRdB = zeros(numPhasingAngles, length(N));

for J = 1 : length(N)

    simulationOptions.phasedArrayNumElements = N(J);

    if simulationOptions.accessPointAntennaType == AntennaType.Isotropic

        beta = -pi*cos(theta_0*pi/180);

    elseif simulationOptions.accessPointAntennaType == AntennaType.
       Dipole

        if simulationOptions.phasedArrayNumElements == 2

            beta = 5*(theta_0-90)*pi/180;
```

```
    elseif simulationOptions.phasedArrayNumElements == 4

        beta = 3.5*(theta_0-90)*pi/180;

    else

        beta = 2.875*(theta_0-90)*pi/180;

    end

else

    if simulationOptions.phasedArrayNumElements == 2

        beta = (-0.0001619*theta_0.^3+0.05498*theta_0.^2-4.25*
            theta_0+55.2)*pi/180;

    elseif simulationOptions.phasedArrayNumElements == 4

        beta = 169*sin((theta_0-90)*pi/180)*pi/180;

    else

        beta = 177*sin((theta_0-90)*pi/180)*pi/180;

    end

end


for I = 1 : numPhasingAngles

    simulationOptions.phasedArrayProgressivePhaseShift = beta(I);

    simulationOptions.numAccessPointAntennas = 1;
    simulationOptions.numMobileAntennas = 1;

    PAAccessPointArray = BuildAccessPointArray(simulationOptions);
    [PASISOCapacities{I, J}, PASISOSNRs{I, J}] =
        EvaluateRoomCapacity(PAAccessPointArray, simulationOptions);

    simulationOptions.numAccessPointAntennas = M;
    simulationOptions.numMobileAntennas = M;

    PAAccessPointArray = BuildAccessPointArray(simulationOptions);
    [PAMIMOCapacities{I, J}, PAMIMOSNRs{I, J}] =
        EvaluateRoomCapacity(PAAccessPointArray, simulationOptions);

end

for I = 1 : numPhasingAngles

    meanPASISOCapacity(I, J) = mean(reshape(PASISOCapacities{I, J},
        simulationOptions.numEvaluationPointsPerSide^2, 1));
```

```
        meanPASISOSNRdB(I, J) = mean(10*log10(reshape(PASISOSNRs{I, J},
            simulationOptions.numEvaluationPointsPerSide^2, 1)));
        meanPAMIMOCapacity(I, J) = mean(reshape(PAMIMOCapacities{I, J},
            simulationOptions.numEvaluationPointsPerSide^2, 1));
        meanPAMIMOSNRdB(I, J) = mean(10*log10(reshape(PAMIMOSNRs{I, J},
            simulationOptions.numEvaluationPointsPerSide^2, 1)));

    end

end

subplot(3,1,1)
plot(theta_0, ones(length(theta_0),1)*meanMIMOCapacity, 'k')
hold on
plot(theta_0, meanPAMIMOCapacity(:,1), 'ko-', 'MarkerSize', 4)
plot(theta_0, meanPAMIMOCapacity(:,2), 'ks-', 'MarkerSize', 4)
plot(theta_0, meanPAMIMOCapacity(:,3), 'k+-', 'MarkerSize', 4)
hold off
axis([90 180 14 26])
set(gca, 'XTick', 90:15:180, 'FontSize', 12, 'FontName', 'Times New
    Roman');
set(gca, 'YTick', 14:3:26, 'FontSize', 12, 'FontName', 'Times New Roman'
    );
xlabel('θ_0 (°)',...
'interpreter','latex',...
'FontSize',12)
ylabel('C̄_MIMO (bps/Hz)',...
'interpreter','latex',...
'FontSize',12)
grid on

subplot(3,1,2)
plot(theta_0, ones(length(theta_0),1)*meanMIMOSNRdB, 'k')
hold on
plot(theta_0, meanPAMIMOSNRdB(:,1), 'ko-', 'MarkerSize', 4)
plot(theta_0, meanPAMIMOSNRdB(:,2), 'ks-', 'MarkerSize', 4)
plot(theta_0, meanPAMIMOSNRdB(:,3), 'k+-', 'MarkerSize', 4)
hold off
axis([90 180 23 35])
set(gca, 'XTick', 90:15:180, 'FontSize', 12, 'FontName', 'Times New
    Roman');
set(gca, 'YTick', 23:3:35, 'FontSize', 12, 'FontName', 'Times New Roman'
    );
xlabel('θ_0 (°)',...
'interpreter','latex',...
'FontSize',12)
ylabel('ρ̄_dB (dB)',...
'interpreter','latex',...
'FontSize',12)
grid on

subplot(3,1,3)
plot(theta_0, ones(length(theta_0),1)*meanMIMOCapacity/meanSISOCapacity,
    'k')
```

```
hold on
plot(theta_0, meanPAMIMOCapacity(:,1)./meanPASISOCapacity(:,1), 'ko-', '
    MarkerSize', 4)
plot(theta_0, meanPAMIMOCapacity(:,2)./meanPASISOCapacity(:,2), 'ks-', '
    MarkerSize', 4)
plot(theta_0, meanPAMIMOCapacity(:,3)./meanPASISOCapacity(:,3), 'k+-', '
    MarkerSize', 4)
hold off
axis([90 180 1.7 2.9])
set(gca, 'XTick', 90:15:180, 'FontSize', 12, 'FontName', 'Times New
    Roman');
set(gca, 'YTick', 1.7:0.3:2.9, 'FontSize', 12, 'FontName', 'Times New
    Roman');
xlabel('θ_0 (°)',...
'interpreter','latex',...
'FontSize',12)
ylabel('\overline{g_C} (-)',...
'interpreter','latex',...
'FontSize',12)
grid on


function ray = AddBoundaryToRay(ray, boundaryNumber)
% This function accepts a ray structure and a number corresponding to a
% particular boundary and adds this number to the list of boundary
% numbers associated with the ray and increments the number of ray
% reflections by 1.

ray.numReflections = ray.numReflections + 1;
ray.reflectionBoundaries(ray.numReflections) = boundaryNumber;


function ray = AddPointToRay(ray, newPoint)
% This function accepts a ray structure and the coordinates of a
% particular point and adds the point to the list of points associated
% with the ray. As a result, the number of ray points is also
% incremented.

ray.numPoints = ray.numPoints + 1;
ray.points(:, ray.numPoints) = newPoint;


classdef Antenna
% This class definition describes an antenna object.  The object is
% defined by the following instance variables:
%
%   antennaType - The type of antenna under consideration.  The
%   possible values are defined by the AntennaType object.
%
%   centrePosition - The location of the origin of the antenna's local
%   coordinate system in metres.
%
%   wavelength - The resonant wavelength of the antenna in metres.
```

```
%
%   orientation — A matrix of three column unit vectors which point in
%   the directions of the x—, y— and z—axes of the antenna's local
%   coordinate system.
%
%   inputImpedance — The antenna input impedance at resonance.

    properties
        antennaType;
        centrePosition;
        wavelength;
        orientation;
        inputImpedance;
    end

    methods

        function obj = Antenna(antennaType, centrePosition, wavelength,
            orientation)

            if ¬nargin

                antennaType = AntennaType.Isotropic;
                centrePosition = [0; 0; 0];
                wavelength = 1;
                orientation = [1, 0, 0; 0, 1, 0; 0, 0, 1];

            end

            obj.antennaType = antennaType;
            obj.centrePosition = centrePosition;
            obj.wavelength = wavelength;
            obj.orientation = [UnitVector(orientation(:, 1)), UnitVector
                (orientation(:, 2)), UnitVector(orientation(:,3))];

            if antennaType == AntennaType.Isotropic

                obj.inputImpedance = 377;

            elseif antennaType == AntennaType.Dipole

                obj.inputImpedance = 73;

            elseif antennaType == AntennaType.Loop

                obj.inputImpedance = 135;

            else

                sprintf('Invalid antenna type; isotropic is assumed.')
                obj.inputImpedance = 377;

            end
```

```
        end

    end

end


classdef AntennaArray < Antenna
% This class definition describes an antenna array object.  It inherits
% antenna element parameters from the antenna class.  It is further
% defined by the following instance variables:
%
%   numElements — The number of elements in the array.  Note that
%   unless the array is made of isotropic radiators, this value should
%   not exceed 2 as the mutual impedances for arrays of realistic
%   antennas with more than 2 elements has not been implemented.
%
%   elementSpacing — The physical distance in meters which separates
%   the elements.
%
%   progressivePhaseShift — The progressive phase shift between
%   elements in the array.
%
%   mutualImpedances — The mutual impedance matrix for the array.
%
% NOTE: If loops are to be used, the default values for elementSpacing
% and orientation MUST be used.  Otherwise the mutual resistances will
% be invalid.

    properties
        numElements;
        elementSpacing;
        progressivePhaseShift;
        mutualImpedances;
    end

    methods

        function obj = AntennaArray(antennaType, centrePosition,
            wavelength, orientation, numElements, elementSpacing,
            progressivePhaseShift)

            if ¬nargin

                antennaType = AntennaType.Isotropic;
                centrePosition = [0; 0; 0];
                wavelength = 0.122;
                orientation = [1, 0, 0; 0, 1, 0; 0, 0, 1];
                numElements = 2;
                elementSpacing = wavelength / 2 + eps;
                progressivePhaseShift = 0;

            end
```

```
            obj = obj@Antenna(antennaType, centrePosition, wavelength,
                orientation);
            obj.numElements = numElements;
            obj.elementSpacing = elementSpacing;
            obj.progressivePhaseShift = progressivePhaseShift;
            obj.mutualImpedances = real(ComputeMutualImpedance(obj));

        end

    end

end


classdef(Enumeration) AntennaType < int32
% This class definition assigns a numerical value to each of the three
% antenna types under consideration.  For example, the type of antenna
% can be addressed as "AntennaType.Isotropic", making the code more
% readable.

    enumeration

        Isotropic(0)
        Dipole(1)
        Loop(2)

    end

end


function antennas = BuildAccessPointArray(simulationOptions)
% This function returns a vector of antenna or phased antenna array
% objects which comprise the access point array based on the input
% simulation options.  The positions of the individual antennas are
% first determined based on the global coordinate system.  They are then
% translated to the coordinate system of the access point.  Finally, the
% antenna or antenna array objects are defined.

arrayPosition = [0; 0; simulationOptions.roomHeight/2 -
    simulationOptions.accessPointArrayDistanceBelowCeiling];

if simulationOptions.numAccessPointAntennas > 1

    if simulationOptions.accessPointMIMOArrayGeometry ==
        MIMOArrayGeometry.Linear

        relativeElementPositions = [zeros(2, simulationOptions.
            numAccessPointAntennas); linspace(-simulationOptions.
            numAccessPointAntennas / 2, simulationOptions.
            numAccessPointAntennas / 2, simulationOptions.
            numAccessPointAntennas)] * simulationOptions.
            accessPointAntennaSpacing;
```

```
elseif simulationOptions.accessPointMIMOArrayGeometry ==
   MIMOArrayGeometry.Circular

    arrayRadius = simulationOptions.accessPointAntennaSpacing / (
       sqrt(2 * (1 - cos(2 * pi / simulationOptions.
       numAccessPointAntennas))));
    elementThetas = (0 : (simulationOptions.numAccessPointAntennas
       -1)) * (2 * pi / simulationOptions.numAccessPointAntennas);
    relativeElementPositions = [arrayRadius * cos(elementThetas);
       arrayRadius * sin(elementThetas); zeros(1, simulationOptions
       .numAccessPointAntennas)];

end

rotationMatrix = EulerRotation(simulationOptions.
   accessPointArrayOrientation);
elementPositions = rotationMatrix * (relativeElementPositions +
   repmat(arrayPosition, 1, simulationOptions.
   numAccessPointAntennas));

if ~simulationOptions.phasedArrays

    antennas(simulationOptions.numAccessPointAntennas) = Antenna(
       simulationOptions.accessPointAntennaType, elementPositions
       (:, simulationOptions.numAccessPointAntennas), (3 * 10^8 /
       simulationOptions.centreFrequency), simulationOptions.
       accessPointAntennaOrientation);

    for nAccessPointAntenna = 1 : simulationOptions.
       numAccessPointAntennas - 1

        antennas(nAccessPointAntenna) = Antenna(simulationOptions.
           accessPointAntennaType, elementPositions(:,
           nAccessPointAntenna), (3 * 10^8 / simulationOptions.
           centreFrequency), simulationOptions.
           accessPointAntennaOrientation);

    end

else

    antennas(simulationOptions.numAccessPointAntennas) =
       AntennaArray(simulationOptions.accessPointAntennaType,
       elementPositions(:, simulationOptions.numAccessPointAntennas
       ), (3 * 10^8 / simulationOptions.centreFrequency),
       simulationOptions.accessPointAntennaOrientation,
       simulationOptions.phasedArrayNumElements, simulationOptions.
       phasedArrayElementSpacing, simulationOptions.
       phasedArrayProgressivePhaseShift);

    for nAccessPointAntenna = 1 : simulationOptions.
       numAccessPointAntennas - 1

        antennas(nAccessPointAntenna) = AntennaArray(
```

```
                simulationOptions.accessPointAntennaType,
                elementPositions(:, nAccessPointAntenna), (3 * 10^8 /
                simulationOptions.centreFrequency), simulationOptions.
                accessPointAntennaOrientation, simulationOptions.
                phasedArrayNumElements, simulationOptions.
                phasedArrayElementSpacing, simulationOptions.
                phasedArrayProgressivePhaseShift);

        end

    end

else

    if ¬simulationOptions.phasedArrays

        antennas = Antenna(simulationOptions.accessPointAntennaType,
            arrayPosition, (3 * 10^8 / simulationOptions.centreFrequency
            ), simulationOptions.accessPointAntennaOrientation);

    else

        antennas = AntennaArray(simulationOptions.accessPointAntennaType
            , arrayPosition, (3 * 10^8 / simulationOptions.
            centreFrequency), simulationOptions.
            accessPointAntennaOrientation, simulationOptions.
            phasedArrayNumElements, simulationOptions.
            phasedArrayElementSpacing, simulationOptions.
            phasedArrayProgressivePhaseShift);

    end

end


function mobileArray = BuildMobileArray(position, simulationOptions)
% This function is largely similar to "BuildAccessPointArray" but is
% intended for the mobile unit.  As a result, there are no provisions
% for the antennas being phased arrays.

if simulationOptions.numMobileAntennas > 1

    if simulationOptions.mobileMIMOArrayGeometry == MIMOArrayGeometry.
        Linear

        relativeElementPositions = [zeros(2, simulationOptions.
            numMobileAntennas); linspace(-simulationOptions.
            numMobileAntennas / 2, simulationOptions.numMobileAntennas /
             2, simulationOptions.numMobileAntennas)] *
            simulationOptions.mobileAntennaSpacing;

    elseif simulationOptions.mobileMIMOArrayGeometry ==
        MIMOArrayGeometry.Circular
```

```
        arrayRadius = simulationOptions.mobileAntennaSpacing / (sqrt(2 *
            (1 - cos(2 * pi / simulationOptions.numMobileAntennas))));
        elementThetas = (0 : (simulationOptions.numMobileAntennas - 1))
            * (2 * pi / simulationOptions.numMobileAntennas);
        relativeElementPositions = [arrayRadius * cos(elementThetas);
            arrayRadius * sin(elementThetas); zeros(1, simulationOptions
            .numMobileAntennas)];

    end

    rotationMatrix = EulerRotation(simulationOptions.
        mobileArrayOrientation);
    elementPositions = rotationMatrix * (relativeElementPositions +
        repmat(position, 1, simulationOptions.numMobileAntennas));

    mobileArray(simulationOptions.numMobileAntennas) = Antenna(
        simulationOptions.mobileAntennaType, elementPositions(:,
        simulationOptions.numMobileAntennas), (3 * 10^8 /
        simulationOptions.centreFrequency), simulationOptions.
        mobileAntennaOrientation);
    for nMobileAntenna = 1 : simulationOptions.numMobileAntennas - 1

        mobileArray(nMobileAntenna) = Antenna(simulationOptions.
            mobileAntennaType, elementPositions(:, nMobileAntenna), (3 *
             10^8 / simulationOptions.centreFrequency),
            simulationOptions.mobileAntennaOrientation);

    end

else

    mobileArray = Antenna(simulationOptions.mobileAntennaType, position,
         (3 * 10^8 / simulationOptions.centreFrequency),
        simulationOptions.mobileAntennaOrientation);

end


function roomWalls = BuildRoom( simulationOptions )
% This functions returns a vector containing wall objects associated
% with a room defined by the simulation options.  The "front" wall is
% defined by y = roomLength/2 and the "right" wall is defined by x =
% roomWidth/2. The other wall names are therefore self-evident.

frontWall = Wall([0; 0.5 * simulationOptions.roomLength; 0],
    simulationOptions.wallRelativePermittivity, [1, 0, 0; 0, 0, 1; 0,
    -1, 0]', simulationOptions.roomWidth, simulationOptions.roomHeight);
rightWall = Wall([0.5 * simulationOptions.roomWidth; 0; 0],
    simulationOptions.wallRelativePermittivity, [0, 0, 1; 0, 1, 0; -1,
    0, 0]', simulationOptions.roomHeight, simulationOptions.roomLength);
backWall = Wall([0; -0.5 * simulationOptions.roomLength; 0],
    simulationOptions.wallRelativePermittivity, [-1, 0, 0; 0, 0, 1; 0,
    1, 0]', simulationOptions.roomWidth, simulationOptions.roomHeight);
leftWall = Wall([-0.5 * simulationOptions.roomWidth; 0; 0],
```

```
    simulationOptions.wallRelativePermittivity, [0, 0, -1; 0, -1, 0; 1,
    0, 0]', simulationOptions.roomHeight, simulationOptions.roomLength);
ceiling = Wall([0; 0; 0.5 * simulationOptions.roomHeight],
    simulationOptions.wallRelativePermittivity, [-1, 0, 0; 0, 1, 0; 0,
    0, -1]', simulationOptions.roomWidth, simulationOptions.roomLength);
floor = Wall([0; 0; -0.5 * simulationOptions.roomHeight],
    simulationOptions.wallRelativePermittivity, [1, 0, 0; 0, 1, 0; 0, 0,
     1]', simulationOptions.roomWidth, simulationOptions.roomLength);

roomWalls = [frontWall; rightWall; backWall; leftWall; ceiling; floor];


function reflectionCoefficient = CalculateReflectionCoefficient(
    incidentTheta, boundary )
% This function accepts an angle of incidence and an electromagnetic
% boundary object and returns a structure of reflection coefficients
% associated with electric field components which are perpendicular and
% parallel to the plane of incidence.

boundaryRefractiveIndex = sqrt(boundary.relativePermittivity);
transmitTheta = asin(sin(incidentTheta) / boundaryRefractiveIndex);

reflectionCoefficient.perpendicular = (cos(incidentTheta) -
    boundaryRefractiveIndex * cos(transmitTheta)) / (cos(incidentTheta)
    + boundaryRefractiveIndex * cos(transmitTheta));
reflectionCoefficient.parallel      = (cos(transmitTheta) -
    boundaryRefractiveIndex * cos(incidentTheta)) / (cos(transmitTheta)
    + boundaryRefractiveIndex * cos(incidentTheta));


function [channelCapacity, SNR] = ChannelCapacity(
    channelTransferFunctions, transmittedSNR, room)
% This function accepts a column matrix of the transfer functions
% associated with a MIMO channel, the transmitted SNR and a room object.
% It returns the frequency-averaged channel capacity and received SNR.

numFrequencySamples = size(channelTransferFunctions, 1);
channelCapacity = 0;
SNR = 0;

for nFrequencySample = 1 : numFrequencySamples

    channelMatrix = reshape(channelTransferFunctions(nFrequencySample,
        :), room.numAccessPointAntennas, room.numMobileAntennas);
    channelCapacity = channelCapacity + log2(det(eye(room.
        numAccessPointAntennas) + ( transmittedSNR / room.
        numMobileAntennas ) * (channelMatrix * channelMatrix'))) /
        numFrequencySamples;
    SNR = SNR + (transmittedSNR * norm(channelMatrix, 'fro')^2 / (room.
        numAccessPointAntennas * room.numMobileAntennas)) /
        numFrequencySamples;

end
```

```
channelCapacity = real(channelCapacity);


function impulseResponses = ChannelImpulseResponses(rays, room,
   simulationOptions)
% This function computes the channel impulse responses associated with
% each of the rays computed for the communication situation.  This is
% accomplished by computing the complex gain and propagation delay
% associated with each ray.  It returns an array of impulse response
% structures.

c = 3 * 10^8;

numMultipathComponents = size(rays, 1);
numAntennaPairs = room.numMobileAntennas * room.numAccessPointAntennas;
impulseResponses(numAntennaPairs) = NewImpulseResponse(
   numMultipathComponents);

for nAntennaPair = 1 : numAntennaPairs

    impulseResponse = NewImpulseResponse(numMultipathComponents);

    for nMultipathComponent = 1 : numMultipathComponents

        ray = rays(nMultipathComponent, nAntennaPair);
        gain = 0;
        delay = 0;

        if ray.isValid

            gain = ComputeRayGain(ray, room, simulationOptions);
            delay = ray.totalLength / c;

        end

        impulseResponse.gains(nMultipathComponent) = gain;
        impulseResponse.delays(nMultipathComponent) = delay;

    end

    impulseResponses(nAntennaPair) = impulseResponse;

end


function transferFunctions = ChannelTransferFunctions(
   complexBasebandImpulseResponses)
% This function accepts a column matrix of complex baseband channel
% impulse responses and returns a column matrix of the corresponding
% channel transfer functions.

nfft = 2^(nextpow2(size(complexBasebandImpulseResponses, 1)));
transferFunctions = fft(complexBasebandImpulseResponses, nfft, 1);
```

```
function Z_matrix = ComputeMutualImpedance(antennaArray)
% This function computes the impedance matrix associated with the input
% antenna array.  The diagonal elements of the matrix are the antenna
% self-impedances while the off-diagonal entries are the associated
% mutual impedances.  The impedances are assumed to be purely real; each
% antenna has been individually tuned for resonance.  NOTE: The mutual
% resistances for loops were calculated manually for the default array
% element spacing and element orientation settings; the resistances will
% NOT be valid for any other arrangment.

if antennaArray.antennaType == AntennaType.Isotropic

    k = 2 * pi / antennaArray.wavelength;
    Z1n = [antennaArray.inputImpedance; zeros(antennaArray.numElements -
        1, 1)];

    for nCoupling = 2 : (antennaArray.numElements)

        d = antennaArray.elementSpacing * (nCoupling - 1);
        R_mutual = real(antennaArray.inputImpedance) * sin(k * d) / (k *
            d);
        Z1n(nCoupling) = R_mutual * cos((nCoupling - 1) * antennaArray.
           progressivePhaseShift);

    end

    Z_matrix = toeplitz(Z1n, Z1n);

elseif antennaArray.antennaType == AntennaType.Dipole

    L = antennaArray.wavelength / 2;
    k = 2 * pi / antennaArray.wavelength;
    Z1n = [antennaArray.inputImpedance; zeros(antennaArray.numElements -
        1, 1)];

    for nCoupling = 2 : (antennaArray.numElements)

        d = antennaArray.elementSpacing * (nCoupling - 1);
        s = d - L;
        h = L + s;

        R_mutual = -15*cos(k*h)*(-2*cosint(2*k*h)+cosint(2*k*(h-L))+
           cosint(2*k*(h+L))-log((h^2 - L^2)/h^2)) ...
                  +15*sin(k*h)*(+2*sinint(2*k*h)-sinint(2*k*(h-L))-
                     sinint(2*k*(h+L)));

        Z1n(nCoupling) = R_mutual * cos((nCoupling - 1) * antennaArray.
           progressivePhaseShift);

    end

    Z_matrix = toeplitz(Z1n, Z1n);

elseif antennaArray.antennaType == AntennaType.Loop
```

```
    R_mutuals = [-44.57, +13.66, -6.466, +3.681, -2.373, +1.645,
       -1.196];
    Z1n = [antennaArray.inputImpedance; zeros(antennaArray.numElements -
        1, 1)];

    for nCoupling = 2 : (antennaArray.numElements)

        R_mutual = R_mutuals(nCoupling - 1);
        Z1n(nCoupling) = R_mutual * cos((nCoupling - 1) * antennaArray.
           progressivePhaseShift);

    end

    Z_matrix = toeplitz(Z1n, Z1n);

end


function signalGain = ComputeRayGain( ray, room, simulationOptions )
% This function computes the complex gain associated with a particular
% ray in the room subject to the simulation options.  The transmitted
% electric (without the effects of the propagation) is first computed.
% Then, effects of all of the reflections are accounted for in order.
% Finally the effects of propagation over the total length of the ray
% are included, and the resulting output voltage is computed.  Note: in
% the case of different transmit and receive antennas, the gain is
% scaled by the square root ratio of the transmitter input impedance to
% the receiver input impedance.

c = 3 * 10^8;

transmittingAntenna = room.mobileAntennas(ray.mobileAntenna);
receivingAntenna = room.accessPointAntennas(ray.accessPointAntenna);

electricField = SignalTransmission(transmittingAntenna, ray.points(:, 2)
   );
waveNumber = 2 * pi * simulationOptions.centreFrequency / c;

for nReflection = 1 : ray.numReflections

    rayOrigin = ray.points(:, nReflection);
    rayReflectionPoint = ray.points(:, nReflection + 1);
    boundary = room.walls(ray.reflectionBoundaries(nReflection));
    electricField = EvaluateReflection(electricField, rayOrigin,
       rayReflectionPoint, boundary);

end

outputVoltage = SignalReception(electricField, ray.points(:, ray.
   numPoints - 1), receivingAntenna) * exp(-1i * waveNumber * ray.
   totalLength) / ray.totalLength;
signalGain = outputVoltage * sqrt(transmittingAntenna.inputImpedance /
   receivingAntenna.inputImpedance);
```

```
classdef ElectromagneticBoundary
% This class definition describes an electromagnetic boundary object.
% It is defined by the following instance variables:
%
%   centrePosition — The location of the origin of the boundary's local
%   coordinate system in metres.
%
%   relativePermittivity — The relative permittivity associated with
%   the boundary.  It is assumed that these boundaries
%   are non—magnetic.
%
%   orientation — A matrix of unit vectors which point in x—, y— and
%   z—directions of the boundary's local coordinate system.
%
%   normalVector — The normal vector associated with the boundary.
%
%   planeEquation — The coefficients of the boundary plane equation
%   in the global coordinate system.

    properties
        centrePosition;
        relativePermittivity;
        orientation;
        normalVector;
        planeEquation;
    end

    methods

        function obj = ElectromagneticBoundary(centrePosition,
           relativePermittivity, orientation)
            obj.centrePosition = centrePosition;
            obj.relativePermittivity = relativePermittivity;
            obj.orientation = [UnitVector(orientation(:, 1)), UnitVector
                (orientation(:, 2)), UnitVector(orientation(:, 3))];
            obj.normalVector = obj.orientation(:,3);
            obj.planeEquation = [obj.normalVector; —dot(obj.normalVector
               , centrePosition)];
        end

    end

end


function rotationMatrix = EulerRotation( Orientation )
% This function accepts an orientation matrix whose rows contain the
% unit vectors of a desired coordinate system in terms of the standard
% cartesian coordinate system.  It returns a rotation matrix which can
% be used to convert a point or vector expressed in the global
% coordinate system to one expressed in the desired coordinate system.

ux = [1;0;0];
uz = [0;0;1];
```

```
Ox = Orientation(:,1);
Oz = Orientation(:,3);

V = cross(uz, Oz);

alpha = 0;
beta = acos(dot(Oz, uz));
gamma = 0;

if norm(V) ≠ 0;

    V = UnitVector(V);
    alpha = atan2(V(2), V(1));

    if norm(Ox) ≠ 0

        gamma = acos(dot(V, Ox));

    end

else

    if norm(Ox) ≠ 0

        gamma = acos(dot(ux, Ox));

    end

end

rotationMatrix_alpha = [ cos(alpha) sin(alpha) 0 ;
                        −sin(alpha) cos(alpha) 0 ;
                             0          0      1 ];

rotationMatrix_beta = [ 1      0          0     ;
                        0  cos(beta) sin(beta) ;
                        0 −sin(beta) cos(beta) ;];

rotationMatrix_gamma = [ cos(gamma) sin(gamma) 0 ;
                        −sin(gamma) cos(gamma) 0 ;
                              0          0      1 ];


rotationMatrix = rotationMatrix_gamma * rotationMatrix_beta *
   rotationMatrix_alpha;


function ray = EvaluateNLOSRay(ray, finalRayDestination,
   boundaryCombination, room)
% This function modifies and returns an input ray structure based on the
% final destination of the ray, the combination of boundaries upon which
% it must reflect and the room object associated with the simulation.
```

```
numBoundaries = length(boundaryCombination);
numRaySegments = numBoundaries + 1;
currentRayDestination = finalRayDestination;
rayDestinations = [zeros(3, numBoundaries), finalRayDestination];

for nBoundary = numBoundaries : -1 : 1

    boundaryNumber = boundaryCombination(nBoundary);
    planeEquation = room.walls(boundaryNumber).planeEquation;
    currentRayDestination = MirrorPoint(currentRayDestination,
       planeEquation);
    rayDestinations(:, nBoundary) = currentRayDestination;

end

for nRaySegment = 1 : numRaySegments

    if ray.isValid

        if nRaySegment ≤ numBoundaries

            ray = EvaluateRayReflection(ray, rayDestinations(:,
               nRaySegment), boundaryCombination(nRaySegment), room);

        else

            ray = EvaluateRaySegment(ray, rayDestinations(:, nRaySegment
               ));

        end

    end

end


function ray = EvaluateRayReflection( ray, rayDestination,
   boundaryNumber, room )
% This function modifies and returns a ray structure based on the
% destination of the ray (usually a point that is mirrored about a
% particular boundary), the number associated with the boundary and the
% correseponding room object.  If, on its way to its (mirrored)
% destination, the ray intersects the intended boundary, this associated
% information is added to the ray structure.  Otherwise, the ray is
% deemed invalid.

rayOrigin = ray.points(:, ray.numPoints);
rayDirection = UnitVector(rayDestination - rayOrigin);
t_destination = dot(rayDirection, rayDestination - rayOrigin);

boundary = room.walls(boundaryNumber);

if dot(rayDirection, boundary.planeEquation(1:3)) ≠ 0
```

```
    t_boundary = -(dot(boundary.planeEquation(1:3), rayOrigin) +
       boundary.planeEquation(4)) / (dot(boundary.planeEquation(1:3),
       rayDirection));

else

    t_boundary = 10^6;

end

if t_boundary <= 0 || t_boundary >= t_destination

    ray.isValid = false;

else

    planeIntersectionPoint = rayOrigin + rayDirection * t_boundary;

    if IsPointOnWall(planeIntersectionPoint, boundary)

        ray = EvaluateRaySegment(ray, planeIntersectionPoint);
        ray = AddBoundaryToRay(ray, boundaryNumber);

    else

        ray.isValid = false;

    end

end


function ray = EvaluateRaySegment(ray, rayDestination)
% This function modifies and returns an input ray sructure based on the
% current destination of the ray.

raySegmentOrigin = ray.points(:, ray.numPoints);
ray.totalLength = ray.totalLength + norm(rayDestination -
   raySegmentOrigin);
ray = AddPointToRay(ray, rayDestination);


function reflectedElectricField = EvaluateReflection(
   incidentElectricField, rayOrigin, rayReflectionPoint, boundary)
% This function computes the electric field vector resulting from the
% reflection of an input electric field vector off a particular boundary
% based on the origin and reflection point associated with a given ray.
% The majority of the computations are performed relative to the local
% coordinate system of the boundary.  The normal vector associated with
% the plane of incidence of the ray upon the boundary is first computed;
% if it is the zero vector, we have normal incidence and the calculation
% is simple.  Otherwise, more complex operations must be carried out
% based on the theory of wave reflections at oblique incidence.
```

```
boundaryRotationMatrix = EulerRotation(boundary.orientation);
boundaryRayOrigin = boundaryRotationMatrix * (rayOrigin -
    rayReflectionPoint);
boundaryNormalVector = boundary.planeEquation(1:3);

rayPropagationVector = rayReflectionPoint - rayOrigin;
incidencePlaneNormalVector = UnitVector(cross(rayPropagationVector,
    boundaryNormalVector));

if any(incidencePlaneNormalVector ~= zeros(3, 1))

    boundaryIncidentTheta = acos(boundaryRayOrigin(3) / norm(
        boundaryRayOrigin));

    reflectionCoefficient = CalculateReflectionCoefficient(
        boundaryIncidentTheta, boundary);

    boundaryIncidentElectricField = boundaryRotationMatrix *
        incidentElectricField;
    boundaryRotatedIncidentElectricField = boundaryIncidentElectricField
         .* [+1; +1; -1];
    rotatedIncidentElectricField = boundaryRotationMatrix' *
        boundaryRotatedIncidentElectricField;

    rotatedIncidentElectricFieldPerpendicular = dot(
        incidencePlaneNormalVector, rotatedIncidentElectricField) *
        incidencePlaneNormalVector;
    rotatedIncidentElectricFieldParallel = rotatedIncidentElectricField
        - rotatedIncidentElectricFieldPerpendicular;

    reflectedElectricField = rotatedIncidentElectricFieldPerpendicular *
         reflectionCoefficient.perpendicular +
        rotatedIncidentElectricFieldParallel * reflectionCoefficient.
        parallel;

else

    boundaryRefractiveIndex = sqrt(boundary.relativePermittivity);
    reflectionCoefficient = (1 - boundaryRefractiveIndex) / (1 +
        boundaryRefractiveIndex);
    reflectedElectricField = reflectionCoefficient *
        incidentElectricField;

end


function [capacities, SNRs] = EvaluateRoomCapacity(accessPointAntennas,
    simulationOptions)
% This function returns the capacity and SNR results associated with the
% simulation subject to a particular access point array and the desired
% simulation options.  This is done by first defining the room and the
% mobile device, then performing the required calculations.
```

```
if nargin < 2

    simulationOptions = NewSimulationOptions();

end

roomWalls = BuildRoom(simulationOptions);

roomCapacityEvaluationWidth = simulationOptions.roomWidth - (4 + sqrt(8)
    ) * (3 * 10^8) / simulationOptions.centreFrequency;
roomCapacityEvaluationLength = simulationOptions.roomLength - (4 + sqrt
    (8)) * (3 * 10^8) / simulationOptions.centreFrequency;
roomCapacityEvaluationHeight = 1 - simulationOptions.roomHeight / 2;
numEvaluationPoints = simulationOptions.numEvaluationPointsPerSide^2;

xLocations = 0;
yLocations = 0;

if numEvaluationPoints > 1

    xLocations = linspace(-roomCapacityEvaluationWidth / 2,
        roomCapacityEvaluationWidth / 2, simulationOptions.
        numEvaluationPointsPerSide);
    yLocations = linspace(-roomCapacityEvaluationLength / 2,
        roomCapacityEvaluationLength / 2, simulationOptions.
        numEvaluationPointsPerSide);

end

[mobileXLocations, mobileYLocations] = meshgrid(xLocations, yLocations);
mobileZLocations = roomCapacityEvaluationHeight * ones(simulationOptions
    .numEvaluationPointsPerSide, simulationOptions.
    numEvaluationPointsPerSide);

capacities = zeros(simulationOptions.numEvaluationPointsPerSide,
    simulationOptions.numEvaluationPointsPerSide);
SNRs = zeros(simulationOptions.numEvaluationPointsPerSide,
    simulationOptions.numEvaluationPointsPerSide);

parfor nLocation = 1 : numEvaluationPoints

    mobilePosition = [mobileXLocations(nLocation); mobileYLocations(
        nLocation); mobileZLocations(nLocation)];
    mobileAntennas = BuildMobileArray(mobilePosition, simulationOptions)
        ;

    room = Room(roomWalls, mobileAntennas, accessPointAntennas);

    rays = RayTracing(room, simulationOptions.numReflections);
    impulseResponses = ChannelImpulseResponses(rays, room,
        simulationOptions);
    complexBasebandImpulseResponses = ImpulseResponseSampling(
        simulationOptions.bandwidth, impulseResponses);
    transferFunctions = ChannelTransferFunctions(
```

```
        complexBasebandImpulseResponses);
    [capacities(nLocation), SNRs(nLocation)] = ChannelCapacity(
        transferFunctions, simulationOptions.transmittedSNR, room);

end


function reflectionBoundaryCombinations =
    GenerateReflectionBoundaryCombinations(numBoundaries, numReflections
    )
% This function creates a matrix containing row vectors of 1s and 0s
% which express the possible combinations of boundaries which a ray may
% reflect off of, subject to the total number of boundaries and the
% number of reflections under consideration.  Since nchoosek is used,
% there is a chance that some of the combinations will be repeated;
% these are removed using the "unique" command.  Furthermore, it is
% impossible for a ray to bounce off of the same boundary twice in a
% row; any combination which indicates that this occurring is
% subsequently removed.

reflectionBoundaryCombinations = unique(nchoosek(repmat(1 :
    numBoundaries, 1, numReflections), numReflections), 'rows');

if numReflections > 1

    shiftedBoundaryCombinations = circshift(
        reflectionBoundaryCombinations, [0, -1]);
    [validRows, ~] = find(reflectionBoundaryCombinations(:, 1 : end - 1)
        ~= shiftedBoundaryCombinations(:, 1 : end - 1));
    reflectionBoundaryCombinations = reflectionBoundaryCombinations(
        validRows, :);

end


function complexBasebandImpulseResponses = ImpulseResponseSampling(
    bandwidth, impulseResponses )
% This function accepts a communication system single-sided baseband
% channel bandwidth and an array of impulse response structures and
% returns a matrix, the columns of which are the complex baseband
% channel impulse responses associated with the room.  A 0 % excess
% bandwidth is assumed. The impulse responses are 10 samples longer than
% would be required for the maximum observed propagation delay.

samplePeriod = 1 / (2 * bandwidth);
numAntennaPairs = length(impulseResponses);
maximumChannelDelay = max(max([impulseResponses.delays]));
sampleIndices = (0 : 1 : (ceil(maximumChannelDelay / samplePeriod) + 10)
    )';
complexBasebandImpulseResponses = zeros(length(sampleIndices),
    numAntennaPairs);

for nAntennaPair = 1 : numAntennaPairs
```

```
    numMultipathComponents = length(impulseResponses(nAntennaPair).
        delays);

    for nMultipathComponent = 1 : numMultipathComponents

        componentGain = impulseResponses(nAntennaPair).gains(
            nMultipathComponent);
        componentDelay = impulseResponses(nAntennaPair).delays(
            nMultipathComponent);
        complexBasebandImpulseResponses(:, nAntennaPair) =
            complexBasebandImpulseResponses(:, nAntennaPair) +
            componentGain * sinc(sampleIndices - componentDelay /
            samplePeriod);

    end

end


classdef(Enumeration) MIMOArrayGeometry < int32
% This class definition assigns a numerical value to the two types of
% MIMO array geometries under consideration.  For example, the type of
% array geometry can be addressed as "MIMOArrayGeometry.Linear", making
% the code more readable.

    enumeration

        Linear(0)
        Circular(1)

    end

end


function Am = MirrorPoint(A, equation)
% This function accepts the coordinates of a point and the equation
% of a plane in vector form and returns the coordinates of the mirror
% image of the point about the plane.

u = UnitVector(equation(1:(length(equation)-1)));
d_ab = PointPlaneDistance(A, equation);
Am = A - 2*d_ab*u;


function impulseResponse = NewImpulseResponse(numComponents)
% This function defines a structure of impulse response propagation
% delays and complex gains based on the anticipated number of multipath
% components.

impulseResponse.delays = zeros(numComponents, 1);
impulseResponse.gains = zeros(numComponents, 1);
```

```
function ray = NewRay(startPoint, maxNumReflections, nMobileAntenna,
    nAccessPointAntenna)
% This function creates a ray structure based on a number of default
% values along with input starting point coordinates, the maximum number
% of reflections the ray is to undergo and the associated mobile and
% access point antenna numbers.

ray.isValid = true;
ray.numPoints = 0;
ray.points = [];
ray.numReflections = 0;
ray.reflectionBoundaries = [];
ray.totalLength = 0;
ray.transmittingAntenna = 1;
ray.mobileAntenna = 1;
ray.accessPointAntenna = 1;

if nargin > 0

    ray.points = [startPoint, zeros(3, 1 + maxNumReflections)];
    ray.numPoints = 1;
    ray.reflectionBoundaries = zeros(1, maxNumReflections);
    ray.mobileAntenna = nMobileAntenna;
    ray.accessPointAntenna = nAccessPointAntenna;

end


function simulationOptions = NewSimulationOptions( centreFrequency )
% This function accepts a centre frequency at which the system is
% intended to operate and returns a structure containing the resulting
% default simulation options.  The structure, "simulationOptions", can
% then be modified to adjust the parameters of the simulation.

if nargin == 0

    centreFrequency = 2.44175 * 10^9;

end

simulationOptions.centreFrequency = centreFrequency;
simulationOptions.bandwidth = 41.75 * 10^6;

simulationOptions.roomWidth = 8;
simulationOptions.roomLength = 8;
simulationOptions.roomHeight = 3;
simulationOptions.wallRelativePermittivity = 4;

simulationOptions.numReflections = 2;
simulationOptions.numEvaluationPointsPerSide = 30;

simulationOptions.numAccessPointAntennas = 3;
simulationOptions.accessPointAntennaType = AntennaType.Isotropic;
simulationOptions.accessPointMIMOArrayGeometry = MIMOArrayGeometry.
```

```
    Circular;
simulationOptions.accessPointAntennaSpacing = 2 * (3 * 10^8) /
    centreFrequency;
simulationOptions.accessPointAntennaOrientation = [ 1, 0, 0 ; 0, 1, 0 ;
    0, 0, 1 ];
simulationOptions.accessPointArrayOrientation = [ 1, 0, 0 ; 0, 1, 0 ; 0,
     0, 1 ];
simulationOptions.accessPointArrayDistanceBelowCeiling = 2 * (3 * 10^8)
    / centreFrequency;

simulationOptions.phasedArrays = false;
simulationOptions.phasedArrayNumElements = 2;
simulationOptions.phasedArrayElementSpacing = 0.5 * 3 * 10^8 /
    simulationOptions.centreFrequency + eps;
simulationOptions.phasedArrayProgressivePhaseShift = 0;

simulationOptions.numMobileAntennas = 3;
simulationOptions.mobileAntennaType = AntennaType.Isotropic;
simulationOptions.mobileMIMOArrayGeometry = MIMOArrayGeometry.Circular;
simulationOptions.mobileAntennaSpacing = 0.5 * (3 * 10^8) /
    centreFrequency;
simulationOptions.mobileAntennaOrientation = [ 1, 0, 0 ; 0, 1, 0 ; 0, 0,
     1 ];
simulationOptions.mobileArrayOrientation = [ 1, 0, 0 ; 0, 1, 0 ; 0, 0, 1
     ];

simulationOptions.transmittedSNR = 10^8;


function d = PointPlaneDistance(A, equation)
% This function accepts the (x,y,z) coordinates of a point and the
% equation of a plane in vector form and returns the distance between
% the point and plane.

u = UnitVector(equation(1:(length(equation)-1)));
p = equation(length(equation));
d = dot(A, u) + p;

end


function rays = RayTracing( room, numReflections )
% This function returns a vector of ray structures corresponding to ray
% tracing in a room defined by the input room object and the desired
% number of reflections.  First, an array containing list of the
% possible boundary reflection combinations is created.  Then, ray
% structures associated with the LOS and NLOS paths for each antenna
% combination are created and stored in "rays".

reflectionBoundaryCombinationArray = cell(numReflections, 1);
numReflectionBoundaryCombinations = zeros(numReflections, 1);

for nReflection = 1 : numReflections
```

```
    reflectionBoundaryCombinationArray{nReflection} =
       GenerateReflectionBoundaryCombinations(room.numWalls,
       nReflection);
    numReflectionBoundaryCombinations(nReflection) = length(
       reflectionBoundaryCombinationArray{nReflection});

end

numRays = 1 + sum(numReflectionBoundaryCombinations);
rays(numRays, room.numMobileAntennas * room.numAccessPointAntennas) =
   NewRay();

for nMobileAntenna = 1 : room.numMobileAntennas

    for nAccessPointAntenna = 1 : room.numAccessPointAntennas

        nAntennaPair = nAccessPointAntenna + (nMobileAntenna - 1) * room
           .numAccessPointAntennas;
        nRay = 1;
        ray = NewRay(room.mobileAntennas(nMobileAntenna).centrePosition,
            0, nMobileAntenna, nAccessPointAntenna);
        rays(nRay, nAntennaPair) = EvaluateRaySegment(ray, room.
           accessPointAntennas(nAccessPointAntenna).centrePosition);

        for nReflection = 1 : numReflections

            reflectionBoundaryCombinations =
               reflectionBoundaryCombinationArray{nReflection};

            for nReflectionBoundaryCombination = 1 :
               numReflectionBoundaryCombinations(nReflection)

                nRay = nRay + 1;
                ray = NewRay(room.mobileAntennas(nMobileAntenna).
                   centrePosition, nReflection, nMobileAntenna,
                   nAccessPointAntenna);
                rays(nRay, nAntennaPair) = EvaluateNLOSRay(ray, room.
                   accessPointAntennas(nAccessPointAntenna).
                   centrePosition, reflectionBoundaryCombinations(
                   nReflectionBoundaryCombination, :), room);

            end

        end

    end

end


function sphericalVector = RectangularToSpherical( rectangularVector,
   pointOfInterest )
% This function accepts a vector in rectangular coordinates along with a
% point of interest and returns the corresponsing vector in spherical
```

```
% coordinates.

phi = atan2(pointOfInterest(2), pointOfInterest(1));
theta = acos(pointOfInterest(3) / norm(pointOfInterest));

conversionMatrix = [sin(theta)*cos(phi),cos(theta)*cos(phi),-sin(phi);
                    sin(theta)*sin(phi),cos(theta)*sin(phi), cos(phi);
                        cos(theta)     ,    -sin(theta)    ,    0    ]';

sphericalVector = conversionMatrix * rectangularVector;


classdef Room
% This class definition describes a room object.  It is defined by the
% following instance variables:
%
%   walls - an array of wall objects which enclose the room.
%
%   numWalls - the number of wall objects in walls.
%
%   mobileAntennas - an array of mobile antenna objects.
%
%   numMobileAntennas - the number of antenna objects in mobileAntennas.
%
%   accessPointAntennas - an array of access point antenna or antenna
%   array objects.
%
%   numAccessPointAntennas - the number of antenna or antenna array
%   objects in accessPointAntennas.

    properties
        walls;
        numWalls;
        mobileAntennas;
        numMobileAntennas;
        accessPointAntennas;
        numAccessPointAntennas;
    end

    methods

        function obj = Room(walls, mobileAntennas, accessPointAntennas)

            obj.walls = walls;
            obj.numWalls = length(walls);
            obj.mobileAntennas = mobileAntennas;
            obj.numMobileAntennas = length(mobileAntennas);
            obj.accessPointAntennas = accessPointAntennas;
            obj.numAccessPointAntennas = length(accessPointAntennas);

        end

    end
```

```
end


function output = SignalReception( electricField, rayOrigin,
    receivingAntenna )
% This function computes the output voltage due to an input electric
% field incident from a particular origin point upon an input receiving
% antenna. The associated elevation and azimuth angles relative to the
% receiving antenna's coordinate system are computed and the electric
% field is converted to spherical receiver coordinates.  The dot product
% of the result with the receiving antenna's vector effective length
% gives the open circuit voltage, half of which corresponds to the
% output voltage assuming conjugate matching.

receiverRotationMatrix = EulerRotation(receivingAntenna.orientation);
receiverRayOrigin = receiverRotationMatrix * (rayOrigin -
    receivingAntenna.centrePosition);

receiverRayTheta = acos(receiverRayOrigin(3) / norm(receiverRayOrigin));
receiverRayPhi = atan2(receiverRayOrigin(2), receiverRayOrigin(1));

receiverElectricField = RectangularToSpherical((receiverRotationMatrix'
    * electricField), receiverRayOrigin);

effectiveLength = VectorEffectiveLength(receivingAntenna,
    receiverRayTheta, receiverRayPhi);

output = dot(receiverElectricField, effectiveLength) / 2;


function electricField = SignalTransmission( transmittingAntenna,
    rayDestination )
% This function computes the electric field emitted from a transmitting
% antenna in the direction of a particular ray destination.  This is
% done by first calculating the elevation and azimuth angles associated
% with the destination relative the local coordinate system of the
% transmitting antenna.  The electric field is then computed based on
% the vector effective length of the antenna; note the the effects of
% propagation are not included, as they will be incorporated after
% reception using the total length of the ray.

transmitterRotationMatrix = EulerRotation(transmittingAntenna.
    orientation);
transmitterRayDestination = transmitterRotationMatrix * (rayDestination
    - transmittingAntenna.centrePosition);

transmitterRayTheta = acos(transmitterRayDestination(3) / norm(
    transmitterRayDestination));
transmitterRayPhi = atan2(transmitterRayDestination(2),
    transmitterRayDestination(1));

inputVoltage = 1;
inputCurrent = inputVoltage / transmittingAntenna.inputImpedance;
waveImpedance = 377;
```

```
waveNumber = 2 * pi / transmittingAntenna.wavelength;
effectiveLength = VectorEffectiveLength(transmittingAntenna,
   transmitterRayTheta, transmitterRayPhi);
transmitterElectricField = -1i * waveImpedance * waveNumber *
   inputCurrent * effectiveLength / (4 * pi);

electricField = transmitterRotationMatrix' * SphericalToRectangular(
   transmitterElectricField, transmitterRayDestination);


function rectangularVector = SphericalToRectangular( sphericalVector,
   pointOfInterest )
% This function accepts a vector in spherical coordinates and a
% particular point of interest and returns the resulting vector in
% rectangular coordinates.

phi = atan2(pointOfInterest(2), pointOfInterest(1));
theta = acos(pointOfInterest(3) / norm(pointOfInterest));

conversionMatrix = [sin(theta)*cos(phi),cos(theta)*cos(phi),-sin(phi);
                    sin(theta)*sin(phi),cos(theta)*sin(phi), cos(phi);
                        cos(theta)     ,    -sin(theta)    ,    0    ];

rectangularVector = conversionMatrix * sphericalVector;


function u = UnitVector(A)
% This function accepts a vector and returns the associated unit vector.

if norm(A) == 0;
    u = zeros(size(A));
else
    u = A / norm(A);
end

end


function vectorEffectiveLength = VectorEffectiveLength(obj, theta, phi)
% This function returns the vector effective length of the input obj
% subject to the input theta and phi angles.  In the case of a phased
% array, the array factor is calculated and incorporated into the vector
% effective length.

if obj.antennaType == AntennaType.Isotropic

    effectiveLengthPhi = 0;
    effectiveLengthTheta = obj.wavelength / sqrt(pi);

elseif obj.antennaType == AntennaType.Dipole

    effectiveLengthPhi = 0;
```

```
    if mod(theta, 2*pi) < 0.02

        effectiveLengthTheta = - ( obj.wavelength / pi ) * sqrt( sin(
            theta) ^ 3 );

    else

        effectiveLengthTheta = - ( obj.wavelength / pi ) * cos((pi/2) *
            cos(theta)) / sin(theta);

    end

elseif obj.antennaType == AntennaType.Loop

    if theta < eps
        effectiveLengthTheta = obj.wavelength * cot(eps) * sin(phi) *
            besselj(1, sin(eps));
    else
        effectiveLengthTheta = obj.wavelength * cot(theta) * sin(phi) *
            besselj(1, sin(theta));
    end

    effectiveLengthPhi = 0.5 * obj.wavelength * cos(phi) * (besselj(0,
        sin(theta)) - besselj(2, sin(theta)));

else

    effectiveLengthPhi = 0;
    effectiveLengthTheta = obj.wavelength / sqrt(pi);

end

vectorEffectiveLength = [ 0; effectiveLengthTheta; effectiveLengthPhi ];

if isa(obj, 'AntennaArray')

    N = obj.numElements;
    if N > 1

        k = 2 * pi / obj.wavelength;
        d = obj.elementSpacing;
        beta = obj.progressivePhaseShift;
        psi = k * d * cos(theta) + beta;
        arrayFactor = 0;
        Z = obj.mutualImpedances;
        N = obj.numElements;

        for n = 1 : N

            arrayFactor = arrayFactor + sqrt((Z(n, n) / N) / sum(Z(n, :)
                )) * exp((n - 1) * 1i * psi);

        end
```

```
        vectorEffectiveLength = vectorEffectiveLength * arrayFactor;

    end

end


classdef Wall < ElectromagneticBoundary
% This class definiation describes a wall object, which inherits several
% properties from the ElectromagneticBoundary class.  It is further
% defined by the following additional instance variables:
%
%   xDim - The dimension of the (rectangular) wall in the x-direction.
%   yDim - The dimension of the (rectangular) wall in the y-direction.

    properties
        xDim;
        yDim;
    end

    methods

        function obj = Wall(centrePosition, relativePermittivity,
            orientation, xDim, yDim)

            obj = obj@ElectromagneticBoundary(centrePosition,
                relativePermittivity, orientation);
            obj.xDim = xDim;
            obj.yDim = yDim;

        end

        function result = IsPointOnWall(point, obj)

            rotationMatrix = EulerRotation(obj.orientation);
            relativePoint = rotationMatrix * (point - obj.centrePosition
                );

            if any(abs(relativePoint) > [0.5 * obj.xDim ; 0.5 * obj.yDim
                ; 100 * eps])

                result = 0;

            else

                result = 1;

            end

        end

    end

end
```

Appendix B

The van der Pauw Method

A theoretical treatment of the van der Pauw method will be presented. It is based on the original papers published by van der Pauw [116, 126] and a supporting text which covers the concept of conformal mapping [127]. A justification for the use of Equation 5.1 in order to determine the conductivity of the square conductive-paper sample will be given. The assumptions associated with the van der Pauw method which were summarized in Section 5.1.1 will be invoked throughout the treatment as needed.

B.1 Derivation of the van der Pauw Formula

Consider a sample defined as a semi-infinite plane in the xy-plane, which is depicted in Figure B.1. Test points denoted by P, Q, R and S are located at arbitrary positions along the edge of the sample, which is also the x-axis in this case. Adjacent test points are separated by distances denoted by s_{PQ}, s_{QR} and s_{RS}. As shown in Figure B.1, a current source drives a current of I_{PQ} into P and out of Q on the semi-infinite sample, while the potential difference between S and R on the sample is measured using a voltmeter.

Due to the semi-infinite nature of the sample, the principle of superposition

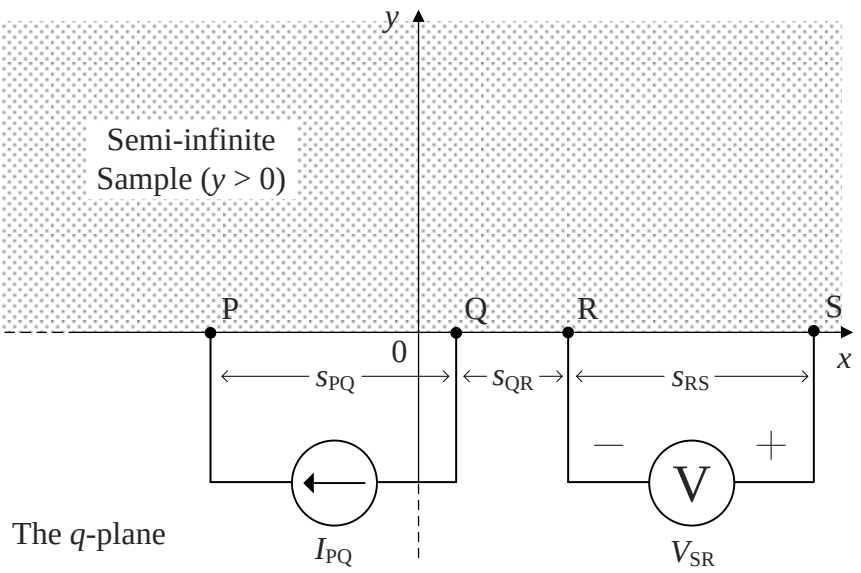

Figure B.1: Semi-infinite sample with the van der Pauw set-up in order to determine the value of $R_{\mathrm{PQ,RS}}$.

can be applied to the current source; the effects of driving current into P can be considered independently from those associated with drawing current from Q. First, consider the case of driving a current equal to I_{PQ} into P while Q is left unconnected. If it can be assumed that the sample material is isotropic, homogeneous in both conductivity and thickness and that the test point contacts are infinitesimally small, then the charges disperse from P evenly in every direction within the sample. In other words, the associated current density is obtained by assuming that I_{PQ} is distributed uniformly along the edge of a semi-circular disc of thickness d_{t} which is centred on P. This current density, denoted by $\vec{J}_{\mathrm{P}}$, can therefore be expressed as

$$\vec{J}_{\mathrm{P}} = \frac{I_{\mathrm{PQ}}}{\pi r d_{\mathrm{t}}}\,\hat{r}, \tag{B.1}$$

where r is taken from P to the point of interest. Let V'_{SR} denote the voltage appearing across S and R due solely to the injection of current into P; it can be expressed in terms of $\vec{J}_{\mathrm{P}}$ as

$$V'_{\mathrm{SR}} = -\frac{1}{\sigma}\int_{R\to S} \vec{J}_{\mathrm{P}} \bullet \vec{dl}, \tag{B.2}$$

where $\vec{dl}$ is the tangential differential length vector associated with an arbitrary path from R to S. Since no current can flow across the x-axis, the simplest path to choose would be a straight line from S to R. In this case, $\hat{r}$ and $\vec{dl}$ would be parallel and the integration could simply be performed over r. The voltage can therefore be expressed as

$$V'_{\mathrm{SR}} = -\frac{I_{\mathrm{PQ}}}{\pi d_{\mathrm{t}}\sigma}\int_{s_{\mathrm{PQ}}+s_{\mathrm{QR}}}^{s_{\mathrm{PQ}}+s_{\mathrm{QR}}+s_{\mathrm{RS}}} \frac{1}{r}\,dr, \tag{B.3}$$

the result of which gives

$$V'_{\mathrm{SR}} = \frac{I_{\mathrm{PQ}}}{\pi d_{\mathrm{t}}\sigma}\ln\left(\frac{s_{\mathrm{PQ}}+s_{\mathrm{QR}}}{s_{\mathrm{PQ}}+s_{\mathrm{QR}}+s_{\mathrm{RS}}}\right). \tag{B.4}$$

Now suppose that P is left unconnected and a current equal to I_{PQ} is drawn from Q. Using a similar procedure, the resulting voltage across S and R, denoted by V''_{SR}, can be expressed as

$$V''_{\mathrm{SR}} = \frac{I_{\mathrm{PQ}}}{\pi d_{\mathrm{t}}\sigma}\ln\left(\frac{s_{\mathrm{QR}}+s_{\mathrm{RS}}}{s_{\mathrm{QR}}}\right). \tag{B.5}$$

Combining V'_{SR} and V''_{SR} gives the value of V_{SR} associated with the set-up depicted in Figure B.1. The result is

$$V_{\mathrm{SR}} = \frac{I_{\mathrm{PQ}}}{\pi d_{\mathrm{t}}\sigma}\ln\left(\frac{(s_{\mathrm{PQ}}+s_{\mathrm{QR}})(s_{\mathrm{QR}}+s_{\mathrm{RS}})}{s_{\mathrm{QR}}(s_{\mathrm{PQ}}+s_{\mathrm{QR}}+s_{\mathrm{RS}})}\right). \tag{B.6}$$

Define $R_{\mathrm{PQ,RS}}$ to be the result of dividing V_{SR} by I_{PQ}. It can therefore be expressed as

$$R_{\mathrm{PQ,RS}} = \frac{1}{\pi d_{\mathrm{t}}\sigma}\ln\left(\frac{(s_{\mathrm{PQ}}+s_{\mathrm{QR}})(s_{\mathrm{QR}}+s_{\mathrm{RS}})}{s_{\mathrm{QR}}(s_{\mathrm{PQ}}+s_{\mathrm{QR}}+s_{\mathrm{RS}})}\right). \tag{B.7}$$

Alternatively,

$$\frac{s_{\mathrm{QR}}(s_{\mathrm{PQ}}+s_{\mathrm{QR}}+s_{\mathrm{RS}})}{(s_{\mathrm{PQ}}+s_{\mathrm{QR}})(s_{\mathrm{QR}}+s_{\mathrm{RS}})}=\exp(-\pi d_{\mathrm{t}}\sigma R_{\mathrm{PQ,RS}}). \tag{B.8}$$

If the current source is instead connected such that current is driven into Q and out of R while the voltmeter is connected such that it is measuring the potential difference between P and S, the associated value of $R_{\mathrm{QR,SP}}$ can be obtained by the same procedure. This situation is depicted in Figure B.2. The resulting expression is

$$R_{\mathrm{QR,SP}}=\frac{1}{\pi d_{\mathrm{t}}\sigma}\ln\left(\frac{(s_{\mathrm{QR}}+s_{\mathrm{RS}})(s_{\mathrm{PQ}}+s_{\mathrm{QR}})}{s_{\mathrm{PQ}}s_{\mathrm{RS}}}\right). \tag{B.9}$$

which can be re-written as

$$\frac{s_{\mathrm{PQ}}s_{\mathrm{RS}}}{(s_{\mathrm{QR}}+s_{\mathrm{RS}})(s_{\mathrm{PQ}}+s_{\mathrm{QR}})}=\exp(-\pi d_{\mathrm{t}}\sigma R_{\mathrm{QR,SP}}). \tag{B.10}$$

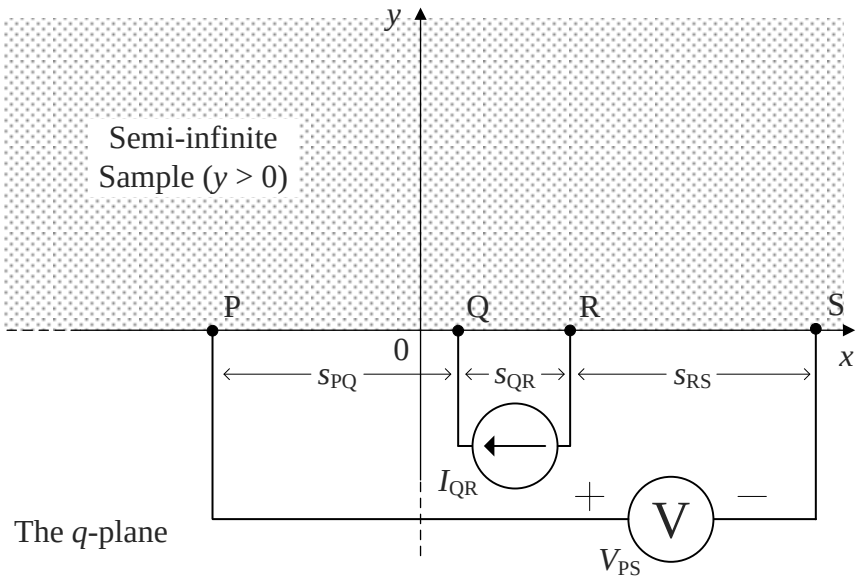

Figure B.2: Semi-infinite sample with the van der Pauw set-up in order to determine the value of $R_{\mathrm{QR,SP}}$.

Summing Equations B.8 and B.10 gives

$$\frac{s_{\mathrm{QR}}(s_{\mathrm{PQ}}+s_{\mathrm{QR}}+s_{\mathrm{RS}})+s_{\mathrm{PQ}}s_{\mathrm{RS}}}{(s_{\mathrm{PQ}}+s_{\mathrm{QR}})(s_{\mathrm{QR}}+s_{\mathrm{RS}})}=\exp(-\pi d_{\mathrm{t}}\sigma R_{\mathrm{PQ,RS}})+\exp(-\pi d_{\mathrm{t}}\sigma R_{\mathrm{QR,SP}}). \quad \text{(B.11)}$$

Note that $s_{\mathrm{QR}}(s_{\mathrm{PQ}}+s_{\mathrm{QR}}+s_{\mathrm{RS}})+s_{\mathrm{PQ}}s_{\mathrm{RS}}=(s_{\mathrm{PQ}}+s_{\mathrm{QR}})(s_{\mathrm{QR}}+s_{\mathrm{RS}})$. Thus Equation B.11 can be re-written as what is known as the van der Pauw formula:

$$1=\exp(-\pi d_{\mathrm{t}}\sigma R_{\mathrm{PQ,RS}})+\exp(-\pi d_{\mathrm{t}}\sigma R_{\mathrm{QR,SP}}). \quad \text{(B.12)}$$

First, Equation 5.1 will derived from the van der Pauw formula, validating its use for the case of a semi-infinite sample. The concept of conformal mapping will then be applied in order to prove the generality of the van der Pauw formula for flat samples of arbitrary shape.

B.2 Derivation of Equation 5.1

Let $a=\pi d_{\mathrm{t}}R_{\mathrm{PQ,RS}}$ and $b=\pi d_{\mathrm{t}}R_{\mathrm{QR,SP}}$. Note that $a=\frac{1}{2}[(a+b)+(a-b)]$ and $b=\frac{1}{2}[(a+b)-(a-b)]$. The van der Pauw formula can therefore be re-written as

$$1=\exp\left(-\frac{\sigma}{2}(a+b)\right)\left[\exp\left(-\frac{\sigma}{2}(a-b)\right)+\exp\left(+\frac{\sigma}{2}(a-b)\right)\right]. \quad \text{(B.13)}$$

Invoking the hyperbolic cosine identity yields

$$\frac{1}{2}=\exp\left(-\frac{\sigma}{2}(a+b)\right)\cosh\left(\frac{\sigma}{2}(a-b)\right). \quad \text{(B.14)}$$

Now, suppose

$$\frac{\ln 2}{p}=\frac{\sigma}{2}(a+b)=\frac{\pi d_{\mathrm{t}}\sigma}{2}\left(R_{\mathrm{PQ,RS}}+R_{\mathrm{QR,SP}}\right), \quad \text{(B.15)}$$

where p is a parameter between 0 and 1 which satisfies Equation B.14. Re-arranging this expression for conductivity yields

$$\sigma = \frac{\ln 2}{\pi d_{\mathrm{t}}} \left(\frac{2}{R_{\mathrm{PQ,RS}} + R_{\mathrm{QR,SP}}} \right) \frac{1}{p}, \tag{B.16}$$

which is analogous to Equation 5.1 except for the presence of p. Using Equation B.15 and some algebraic manipulation, the van der Pauw formula can be re-written as

$$\frac{1}{2} = \exp\left(-\frac{\ln 2}{p} \right) \cosh\left(\left[\frac{R_{\mathrm{PQ,RS}} - R_{\mathrm{QR,SP}}}{R_{\mathrm{PQ,RS}} + R_{\mathrm{QR,SP}}} \right] \frac{\ln 2}{p} \right). \tag{B.17}$$

This expression can be solved numerically in order to determine the relationship between p and the ratio of $R_{\mathrm{PQ,RS}}$ and $R_{\mathrm{QR,SP}}$; a plot of the resulting curve can be found in the paper by van der Pauw [116]. For this treatment, it is sufficient to note that as long as

$$\frac{1}{2} \leq \frac{R_{\mathrm{PQ,RS}}}{R_{\mathrm{QR,SP}}} \leq 2, \tag{B.18}$$

the value of p is very close to unity and its impact on Equation B.16 can be ignored. This condition can be met by choosing the locations of the test points such that there is a degree of symmetry between measurement set-ups for determining $R_{\mathrm{PQ,RS}}$ and $R_{\mathrm{QR,SP}}$. As long as this is the case, the validity of Equation 5.1 has been proven for determining the conductivity of a semi-infinite sample. The generality of the van der Pauw formula must now be proven for a flat sample of arbitrary shape.

B.3 Generality of the van der Pauw Formula

The semi-infinite sample depicted in Figures B.1 and B.2 occupies the $y > 0$ portion of the xy-plane. Another way to treat this situation is to define $q = x + jy$ and instead describe the semi-infinite sample as occupying a portion of the q-plane.

In general, a two-dimensional field within the sample, denoted by $w(q)$, is described by

$$w(q) = u(x, y) + jv(x, y), \tag{B.19}$$

where $u(x, y)$ and $v(x, y)$ are real functions. Most practical fields are analytic, meaning that over the region of interest $w(q)$ can be meaningfully differentiated with respect of q. It will be assumed here that $w(q)$ is analytic, which also means that the field obeys the Cauchy-Riemann equations:

$$\frac{\partial u(x, y)}{\partial x} = \frac{\partial v(x, y)}{\partial y}; \tag{B.20}$$

$$\frac{\partial u(x, y)}{\partial y} = -\frac{\partial v(x, y)}{\partial x}. \tag{B.21}$$

A consequence of the Cauchy-Riemann equations is that the curves $u(x, y) = \mathrm{c}_1$ and $v(x, y) = \mathrm{c}_2$ are always orthogonal to each other, where c_1 and c_2 are constants. Therefore, $u(x, y)$ and $v(x, y)$ can be defined as the potential and the lines of force associated with the field, respectively. For example, the curve $u(x, y) = \mathrm{c}_1$ plotted in the q-plane, would fully describe the c_1 equipotential line.

The net current traversing an arbitrary surface, S, defined on the semi-infinite sample in the q-plane is to be determined. Assume that this surface is comprised of an arbitrary line connecting the arbitrary points T_1 and T_2 which has simply been extended from $z = -d_\mathrm{t}/2$ to $z = d_\mathrm{t}/2$. Figure B.3 illustrates this situation.

The surface can be defined parametrically in terms of two variables: χ, which indicates the position between T_1 and T_2 along the arbitrary line, and ψ, which indicates the height within the sample. The x and y coordinates associated with the surface are both functions of χ, while ψ is simply equal to z since the sample is assumed to be very thin, precluding variations in the shape of the surface along the z

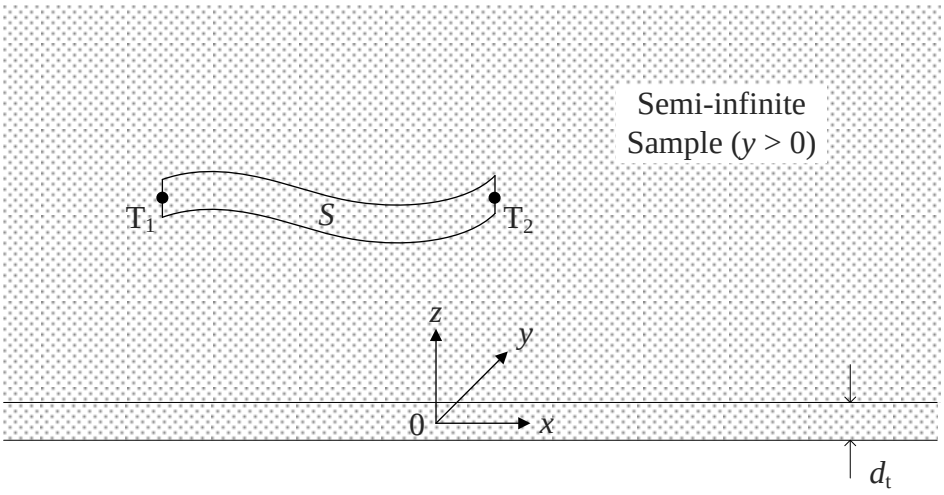

Figure B.3: Illustration of the arbitrary surface in the semi-infinite sample through which the net current is to be determined.

direction. The surface normal vector can be evaluated based on the surface tangent vectors associated with χ and ψ, denoted by $\vec{T}_\chi$ and $\vec{T}_\psi$, respectively. These are given by

$$\vec{T}_\chi = \frac{\partial x}{\partial \chi}\hat{x} + \frac{\partial y}{\partial \chi}\hat{y} + 0\hat{z} \tag{B.22}$$

and

$$\vec{T}_\psi = 0\hat{x} + 0\hat{y} + 1\hat{z} \tag{B.23}$$

where $\hat{x}$, $\hat{y}$ and $\hat{z}$ are the x, y and z unit vectors, respectively. The surface normal vector, $\vec{n}_S$ is therefore given by the cross product of $\vec{T}_\chi$ and $\vec{T}_\psi$:

$$\vec{n}_S = \vec{T}_\chi \times \vec{T}_\psi = \frac{\partial y}{\partial \chi}\hat{x} - \frac{\partial x}{\partial \chi}\hat{y} + 0\hat{z}. \tag{B.24}$$

Since the range of values which χ can assume has not been specified, the condition $|\vec{n}_S| = 1$ can be asserted without loss of generality.

The net current passing through the surface S, denoted by I_S, can be expressed as

$$I_S = \sigma \int_S \vec{E} \bullet d\vec{S}, \tag{B.25}$$

where $\vec{E} = E_x\hat{x} + E_y\hat{y} + E_z\hat{z}$ and $d\vec{S}$ is the differential surface normal vector. Using the parametric definition of the surface, this can be re-written as

$$I_S = \sigma \int_{-d_t/2}^{+d_t/2} \int_{\chi_1}^{\chi_2} \left(\vec{E} \bullet \vec{n}_S\right) d\chi \, d\psi, \tag{B.26}$$

where χ_1 and χ_2 are the χ-values associated with T_1 and T_2, respectively. Employing Equation B.24 gives

$$I_S = \sigma \int_{-d_t/2}^{+d_t/2} \int_{\chi_1}^{\chi_2} \left(E_x \frac{\partial y}{\partial \chi} - E_y \frac{\partial x}{\partial \chi}\right) d\chi \, d\psi. \tag{B.27}$$

Since the integrand is independent of ψ, this reduces to

$$I_S = \sigma d_t \int_{\chi_1}^{\chi_2} \left(E_x \frac{\partial y}{\partial \chi} - E_y \frac{\partial x}{\partial \chi}\right) d\chi. \tag{B.28}$$

Now, if $u(x, y)$ is assumed to be the potential associated with the field within the sample, let:

$$E_x = \frac{\partial u(x, y)}{\partial x}; \tag{B.29}$$

$$E_y = \frac{\partial u(x, y)}{\partial y}. \tag{B.30}$$

Applying these expressions to Equation B.28 allows the integral to be re-written in terms of x and y:

$$I_S = \sigma d_\mathrm{t} \int_{\mathrm{T}_1}^{\mathrm{T}_2} \left(\frac{\partial u(x,y)}{\partial x}\, dy - \frac{\partial u(x,y)}{\partial y}\, dx \right). \tag{B.31}$$

Employing the Cauchy-Riemann equations gives

$$I_S = \sigma d_\mathrm{t} \int_{\mathrm{T}_1}^{\mathrm{T}_2} \left(\frac{\partial v(x,y)}{\partial y}\, dy + \frac{\partial v(x,y)}{\partial x}\, dx \right), \tag{B.32}$$

which can be further simplified to

$$I_S = \sigma d_\mathrm{t} \int_{v_1}^{v_2} dv(x,y), \tag{B.33}$$

where v_1 and v_2 are the values of $v(x,y)$ occurring at T_1 and T_2, respectively. Finally,

$$I_S = \sigma d_\mathrm{t}(v_2 - v_1), \tag{B.34}$$

which can be re-arranged as

$$v_2 - v_1 = \frac{I_S}{\sigma d_\mathrm{t}}. \tag{B.35}$$

This result is interesting in that the sample need not be semi-infinite in order to obtain it. In fact, Equation B.35 applies for an arbitrary surface located anywhere within a flat sample of arbitrary shape.

For now, consider the semi-infinite sample as depicted in Figures B.1 and B.2. Equation B.35 is only useful if the surface S is defined such that the behaviour of I_S is known. This occurs most conveniently along the x-axis since current only traverses the edge of the sample at the test points which are connected to the current source. Taking the set-up depicted in Figure B.1 as an example, I_S will only be non-zero for a surface defined along the x-axis if the surface passes through P and not Q, or vice versa. Figure B.4 illustrates each of these situations from a top view of the q-plane. The solutions to Equation B.35 for the situations in Figures B.4(a) and B.4(b) are

$$v_2 - v_1 = +\frac{I_{\mathrm{PQ}}}{\sigma d_{\mathrm{t}}} \tag{B.36}$$

and

$$v_2 - v_1 = -\frac{I_{\mathrm{PQ}}}{\sigma d_{\mathrm{t}}}, \tag{B.37}$$

respectively. Although these results may seem initially vague from a practical standpoint, they imply that the behaviour of the field within the semi-infinite sample is known along the x-axis.

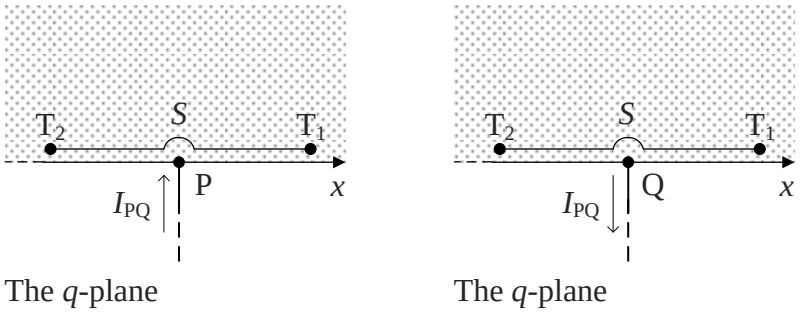

(a) The surface passes through P. (b) The surface passes through Q.

Figure B.4: Surface definitions along the x-axis which give non-zero results for Equation B.35.

Now consider a flat sample of arbitrary shape defined in the q'-plane, where $q' = x' + jy'$. Figure B.5 illustrates an example of such a sample. The field within the sample will be defined as $w'(q') = u'(x', y') + jv'(x', y')$, which is similar to $w(q)$ for the semi-infinite sample in the q-plane.

As previously mentioned, the derivation of Equation B.35 is applicable anywhere within a flat sample of any shape. Consequently, the result can be used to characterize the field within the arbitrary sample in the q'-plane. This can be most effectively done along the edge of the sample as the result will only be non-zero for a surface passing through A and not B, or vice versa. The solutions for each case are

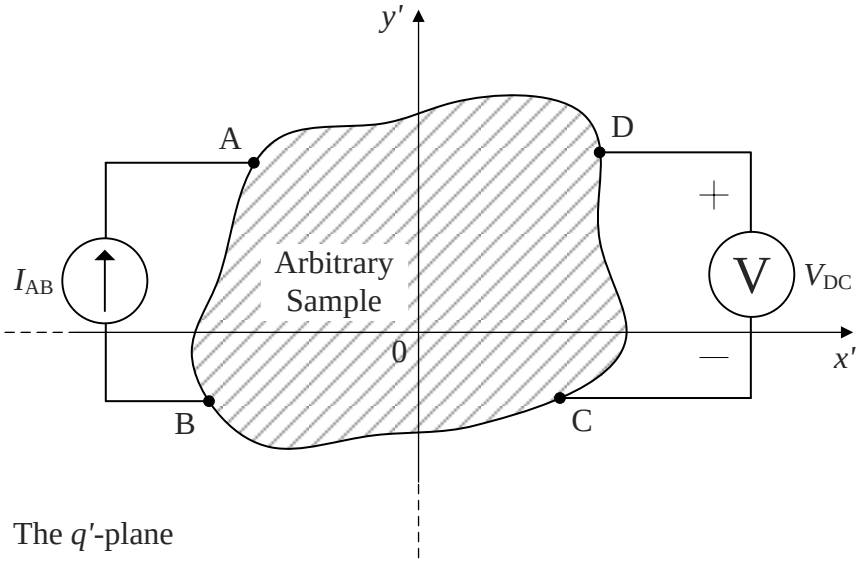

Figure B.5: Arbitrary sample with the van der Pauw set-up in order to determine the value of $R_{\mathrm{AB,CD}}$.

$$v_2' - v_1' = +\frac{I_{\mathrm{AB}}}{\sigma d_{\mathrm{t}}} \tag{B.38}$$

and

$$v_2' - v_1' = -\frac{I_{\mathrm{AB}}}{\sigma d_{\mathrm{t}}}, \tag{B.39}$$

respectively. As long as $I_{\mathrm{AB}} = I_{\mathrm{PQ}}$, it can be concluded that the field along the edge of the arbitrary sample in the q'-plane is equivalent to the field along the x-axis for the semi-infinite sample in the q-plane.

Assuming the arbitrary sample to be singly connected, meaning that it contains no isolated holes, it can be equated to the semi-infinite sample via conformal mapping. More specifically, the edge of the arbitrary sample in the q'-plane can be mapped to the x-axis in the q-plane. The space within the arbitrary sample in the q'-plane would therefore be mapped to $y > 0$ in the q-plane while the space outside the arbitrary sample is mapped to $y < 0$. If A, B, C and D in the q'-plane are images of P, Q,

R and S in the q-plane, it can be concluded that $V_{\mathrm{DC}} = V_{\mathrm{SR}}$ and $V_{\mathrm{AD}} = V_{\mathrm{PS}}$ since $w'(q')$ behaves exactly the same along the edge of the arbitrary sample as $w(q)$ does along the x-axis. If $I_{\mathrm{AB}} = I_{\mathrm{PQ}}$ and $I_{\mathrm{BC}} = I_{\mathrm{QR}}$, it is clear that $R_{\mathrm{AB,CD}} = R_{\mathrm{PQ,RS}}$ and $R_{\mathrm{BC,DA}} = R_{\mathrm{QR,SP}}$. Consequently, the van der Pauw formula is equally valid for a flat sample of arbitrary shape as it is for a semi-infinite sample.

The generality of the van der Pauw formula permits the application of Equation 5.1 to the set-up depicted in Figure 5.1.

Vita

Candidate's full name: Christopher David Rouse

University attended: University of New Brunswick, B.Sc.E., 2009

Publications:

Chris D. Rouse, Brent R. Petersen and Bruce G. Colpitts, "Characterizing an in-room MIMO system employing elevation-directional access point antennas," to be submitted.

Chris D. Rouse, Michael R. Kurz, Brent R. Petersen and Bruce G. Colpitts, "Performance evaluation of conductive-paper dipole antennas," *IEEE Transactions on Antennas and Propagation*, vol. 61, no. 3, pp. 1427–1430, March 2013.

Brandon C. Brown, Frédéric G. Goora and Chris D. Rouse, "The design of an economical antenna-gain and radiation-pattern measurement system," *IEEE Antennas and Propagation Magazine*, vol. 53, no. 4, pp. 188–200, August 2011.

Chris D. Rouse, Anthony W. Brown, Michael T. V. Wylie, and Bruce G. Colpitts, "Phase-locking of commercial DFB lasers for distributed optical fiber sensing applications," *Proceedings of the SPIE*, vol. 7753, May 15–19 2011.